Use of Nonlinear Volterra Theory in Predicting the Propagation of Non-uniform Flow Through an Axial Compressor

by

Jonathan G. Luedke

Thesis submitted to the Faculty of the
Virginia Polytechnic Institute and State University
in partial fulfillment of the requirements for the degree of

Master of Science

in

Mechanical Engineering

Approved:

_____

W.F. O'Brien, Committee Chair

K.A. Thole	P.S. King	C.L.Dancey

December 6, 2001
Blacksburg, VA

Use of Nonlinear Volterra Theory in Predicting the Propagation of Non-Uniform Flow Through an Axial Compressor

by

Jonathan Luedke

(ABSTRACT)

Total pressure non-uniformities in an axial flow compressor can contribute to losses in aerodynamic operability through a reduction in stall margin, pressure rise and mass flow, and to loss of structural integrity through means of high cycle fatigue (HCF). HCF is a primary mechanism of blade failure caused by vibrations at levels exceeding material endurance limits. Previous research has shown total pressure distortions to be the dominant HCF driver in aero engines, and has demonstrated the damaging results of total pressure distortion induced HCF on first stage fan and compressor blade rows [Manwaring et al., 1997]. It is, however, also of interest to know how these distortion patterns propagate through a rotor stage and impact subsequent downstream stages and engine components. With current modeling techniques, total pressure distortion magnitudes can be directly correlated to induced blade vibratory levels and modes. The ability to predict downstream distortion patterns then allows for the inference of blade vibratory response of downstream blades to inlet distortion patterns. Given a total pressure distortion excitation entering a blade row, the nonlinear Volterra series can serve as a predictor of the downstream total pressure profile and therefore provide insight into the potential for HCF in downstream blade rows.

This report presents the adaption of nonlinear Volterra theory to the prediction of the transport of non-uniform total pressure distortions through an axial flow compressor. The use of Volterra theory in nonlinear system modeling relies on the knowledge of Volterra kernels, which capture the behavior of a system's response characteristics. Here an empirical method is illustrated for identifying these kernels based on total pressure distortion patterns measured both upstream and downstream of a transonic rotor of

modern design. A Volterra model based on these kernels has been applied to the prediction of distortion transfer at new operating points of the same rotor with promising results. Methods for improving Volterra predictions by training Volterra kernels along individual streamlines and normalizing total pressure data sets by physics-based parameters are also investigated.

Acknowledgements

I would like to thank my graduate committee for serving in this capacity. In particular I would like to thank Dr. O'Brien for introducing me to this project and providing continuous guidance and support along the way. A special thanks goes to Dr. Doug Rabe of the Compressor Research Facility at Wright-Patterson Air Force Base for funding this project and providing the experimental resources for this study.

I owe a debt of gratitude to Matt Small, my predecessor on this work, for taking the time to introduce me to this project. I would also like to thank Matt for coming across the concept of Volterra theory and realizing its potential for the work at hand.

The support and friendship of the members of the Turbolab have truly made the experience of completing this task an enjoyable and memorable one. Thanks to Drew, Karl, Keith, Matt, Scott, Mac, Joe, Wayne, Grant, John, Kevin, Rob, Melissa, and Pete for their friendship and support.

As always, my family and friends have been a tremendous source of support and encouragement throughout this project. Thank you to my parents, my sister and her family for supporting my decision to return to school and complete an advanced degree. Every accomplishment I have ever made, including this one, I owe to them.

And finally I would like to thank my girlfriend, and now fiancée, Jenny, for everyday showing me the light at the end of the road.

Table of Contents

Table of Tables

Table of Figures

Table of Equations

1 Introduction

The assumption of uniform flow through aero engines has historically been relied upon in the aerodynamic design process. The validity of this assumption, however, has diminished over the years as aircraft and aero engine performance have been pushed to new, extreme limits. Modern flight conditions and aircraft design make non-uniform conditions at engine inlets very much a reality that must be recognized and incorporated into the design process.

Modeling inlet flow distortions in aero engines is a subject that has been studied for quite some time, both in terms of the effects on compressor performance and the transfer of distortions to downstream engine components. In the past, linear correlation models have been applied to this task, and have found a certain degree of success. As technology has advanced and the envelope of turbomachinery performance has been stretched, the extent to which linear models apply has become limited. Because of this, nonlinear methods of modeling flow distortion resident in a compressor rotor are desired. This study will focus on modeling the transfer of non-uniform flow through a compressor rotor using nonlinear Volterra theory.

A flow distortion is defined as a deviation from a steady, uniform distribution of flow properties within a flow path. These are characterized by the level, extent, and time interval over which they exist. Distortions can exist in flow properties such as swirl, vorticity, turbulence, total and static pressure, velocity, temperature, flow angle, density, and many others. The most common of these distortions encountered in aero engine operation is total pressure, which will be the focus of this study.

Inlet flow distortions in aero engines are caused by a number of phenomena, and exist in both steady and time varying states. Several causes of distortion are inherent to the design of the engine itself, such as non-axisymmetric intake duct geometry (e.g. serpentine inlets) and the location of the engine inlet with respect to the airframe. Other causes are related to the operating conditions of the aircraft. Examples include the pitch and yaw angle of the aircraft, flow separation from the lip of the inlet during maneuvers, shock induced separation during supersonic flight, and the ingestion of wakes from other

aircraft or from the launching of armaments in the case of military applications. Figure 1.1 and Figure 1.2 illustrate several causes of inlet distortion.

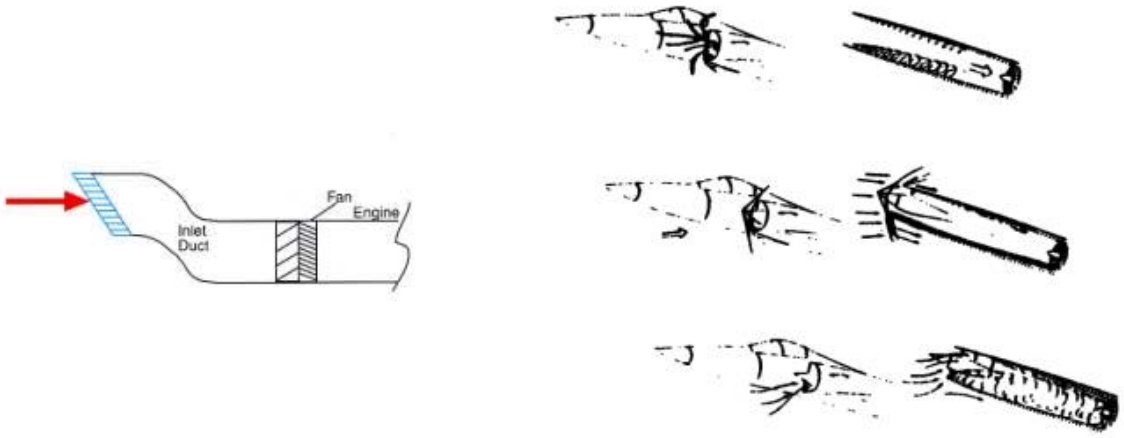

Figure 1.1. Illustrations of inlet distortion due to non-axisymmetric intake and flow separation at the inlet [Small, 2001].

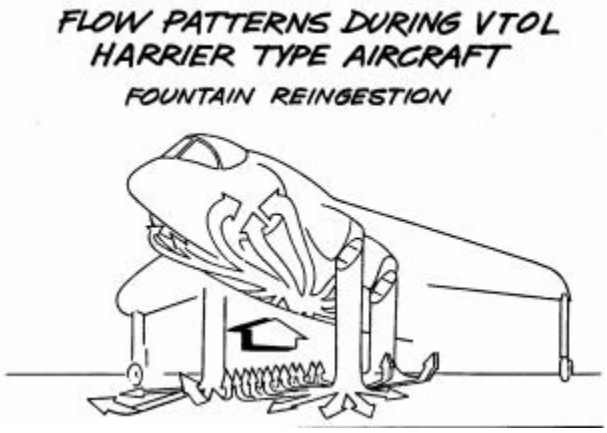

Figure 1.2. Illustration of inlet distortion due to ingestion of exhaust gases from a VTOL (Vertical Take Off and Landing) aircraft [SAE ARD50015, 1991].

The end result of inlet flow distortions in aero engines is degraded engine performance. This degradation can be manifested in two distinct forms: loss in compressor thermodynamic performance and loss in structural integrity through the excitation of blade vibratory modes.

Loss in compressor thermodynamic performance due to flow distortion presents a loss in pressure rise and/or mass flow. This, in effect, leads to a reduction in stall margin, thereby limiting the performance capabilities of the engine. As a compressor nears stall it is unable to maintain its design pressure ratio, possibly leading to the phenomena of surge. Surge is characterized by a flow reversal in the engine due to loss of pressure in the compressor and existing higher pressures in the combustor and turbine. Surge can lead to flame-out in the combustor as well as severe damage to engine components as hot turbine gases are introduced into significantly cooler compressor gases.

Today's aero engines must meet demands such as increased thrust to weight ratio and reduced specific fuel consumption, and as a result are built with fewer fan, compressor, and turbine stages with higher-pressure ratio per stage and highly stressed airfoil configurations. These factors lead to airfoils with closely spaced modes of vibration, and therefore increased levels of aerodynamic excitations and reduced overall system damping [Capece et al, 1997]. Flow distortions present periodic blade passing frequencies to rotor blades, which are capable of exciting these blade vibratory modes. Blade passing frequencies combined with the relative rotation of blades can lead to a condition known as high cycle fatigue (HCF), which is a primary mechanism of blade failure caused by vibrations at levels exceeding material endurance limits [Vahdati et al, 2000]. Direct correlations between distortion intensity levels and blade vibratory stresses have been made, making HCF a significant source of concern in blade failure and ultimately in engine reliability.

Previous studies have shown that fluctuations in total pressure are the dominant HCF driver in aero engine fans and compressors [Manwaring et al., 1997]. Figure 1.3 provides an example of the increase of blade vibratory stress as a function of increasing total pressure distortion. It is apparent from the first graph that there is a direct, nearly linear, correlation between distortion intensity and vibratory stresses. Also presented in Figure 1.3 is a Campbell diagram. Campbell diagrams are used to illustrate the relationship between blade vibratory modes, rotational speed and excitation frequency, and can also include areas of a blade where resonance is likely to occur. This particular Campbell diagram shows forcing frequencies to be a function of the number of total pressure deficits, or per revs, and to have an increasing trend with rotational speed.

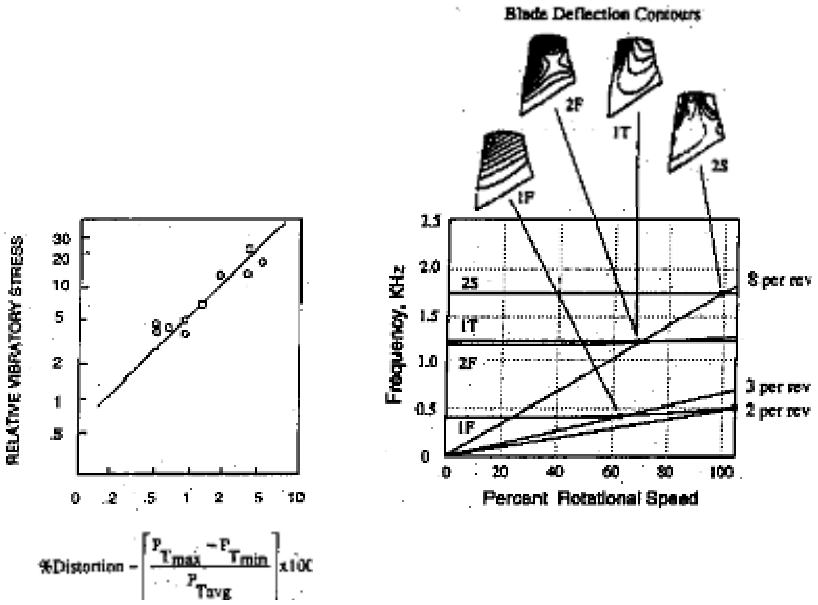

Figure 1.3. Example of blade vibratory stress as a function of total pressure distortion [Manwaring et al., 1997] and of a Campbell diagram [Danforth, 1975].

The severity of blade vibration levels depends on two factors: the level of unsteady aerodynamic loading and the total damping of the blades. With the advent of blisks (modern integrally bladed disks), which are characterized by reduced blade damping at the hub, the need for an understanding of the behavior of unsteady aerodynamic loading has moved to the forefront of much research. A particular area of interest in the behavior of flow distortion is the manner in which it propagates through a blade row. As a distortion pattern exits a stage, it serves as a driving force for the next blade row or engine component immediately following. While much of the past research in the area of flow distortion induced HCF has focused solely on the first stage fan or compressor blade row, the present study examines the threat posed to subsequent downstream stages. Figure 1.4 illustrates dynamic total pressure distortion levels measured both upstream and downstream of a first stage transonic compressor rotor. As seen at the stage outlet strong distortion levels exist and, although diminished from inlet levels, still present a significant driving force for the following stage. Maximum fluctuations downstream of the rotor remain in the neighborhood of 50% of maximum inlet fluctuations. This figure

demonstrates the importance of not overlooking the possible effects of inlet flow distortions on downstream engine components.

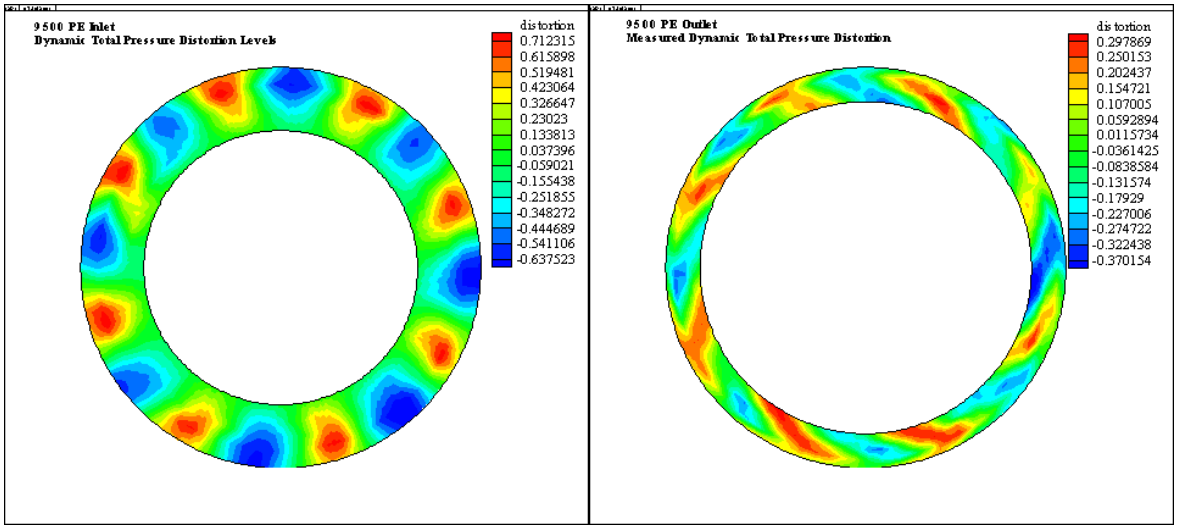

Figure 1.4. Dynamic total pressure distortion levels upstream and downstream of a compressor rotor.

This study will be centered on the prediction of dynamic total pressure distortion patterns downstream of a compressor rotor by means of nonlinear Volterra theory. With the concept of HCF excitation sources in mind, frequency content of downstream predictions will be the focal point of analysis. The Integrated High Performance Turbine Engine Technology program (IHPTET) has set a goal to be able to predict vibratory stresses anywhere on a blade to within 20% of measurements [Gas Turbine High Cycle Fatigue web site, www.utc-hcf.com]. Being able to predict the propagation of distorted flow into subsequent rotors is then an initial step in meeting this goal.

2 Literature Review

A vast amount of work has been directed towards the understanding of inlet flow non-uniformities in aero engines and their effects on engine (compressor) performance. As will be shown in a review of literature concerning the subject at hand, a majority of work has focused on the effect of inlet distortion on the thermodynamic performance of compressors, specifically in terms of reduced pressure rise and stall. However, there is a need for a better understanding of inlet distortion as related to aeromechanical effects. Several works leading toward this will be presented.

A wide variety of modeling techniques aimed at predicting compressor response to inlet flow non-uniformities exist and will be examined. As will be shown, each of these techniques has found success. However, each operates under set assumptions that restrict their use to specific areas. Finally, the fairly new concept of applying nonlinear Volterra theory in aerodynamic response applications will be reviewed.

2.1 Influence of Flow Distortion on Thermodynamic and Aeromechanical Compressor Performance

Biesiadny et al (1986) presented a summary of investigations of engine response to distorted inlet conditions conducted at NASA Lewis Research Center. Specific findings of compressor response to inlet total pressure distortions included,

- Rate of attenuation of total pressure distortion increased with increasing rotor speed.
- Total temperature distortions were created by two unequal pressure ratios resulting from pressure distortions.
- Inlet total pressure distortions rotating about the engine axis increased stall margin when distortion pattern rotated opposite to the compressor, but decreased stall margin when rotating with the compressor.

- Stall was most likely to occur over a low range of rotor speeds and was unlikely to occur above this range. This result is due to the finite time required for the blade to stall in response to the distortion. A lower rotor speed corresponds to a lower absolute flow velocity and therefore a longer distortion dwell time in the rotor passage.

Schwartz (1999), based on experimental analysis, characterized the typical behavior of flow distortions at the inlet and exit of a low speed fan rotor. Specific flow behavior observed at the inlet of the fan rotor included,

- Increased angle of attack.
- Increased pitch angle.
- Decreased total and static pressures.
- Velocity slowly increased while approaching the distortion and then dropped off to its distorted value.

Specific flow behavior observed at the exit of the fan rotor included,

- Decreased total pressure.
- Wake depth increased in absolute magnitude.
- Wake width dipped at the leading edge and peaked at the trailing edge.
- Suction-side jet magnitude and width both dipped at leading edge, peaked at trailing edge, and otherwise maintained a constant value throughout the entire profile.

Greitzer and Longley (1992) discussed the effect of varying the extent of circumferential total pressure distortions entering an engine. Here they defined the angle of spoiling, which is the total angular width of the distorted inlet sector. A series of experiments revealed trends of compressor performance when presented with a variety of inlet distortions.

Figure 2.1 and Figure 2.2 illustrate the compressor delivery pressure at surge line for different distortion arrangements. Analysis of Figure 2.1 shows that as the angular width of the spoiled sector is increased, there is a point at which further increases in width have negligible effect on the exit static pressure. This width is defined as the critical sector angle, θ_{crit}, and is seen to occur around 90° in Figure 2.1. Figure 2.2 provides insight into the effect of subdividing a distortion into different numbers of equal sections, totaling the same overall spoiled section in each case. It can be seen here that the greatest loss of peak pressure rise due to distortion occurs when there is only one spoiled region. The reasoning behind this experimental finding is that the larger a spoiled sector is, the longer the dwell time experienced by the rotor in the pressure deficit.

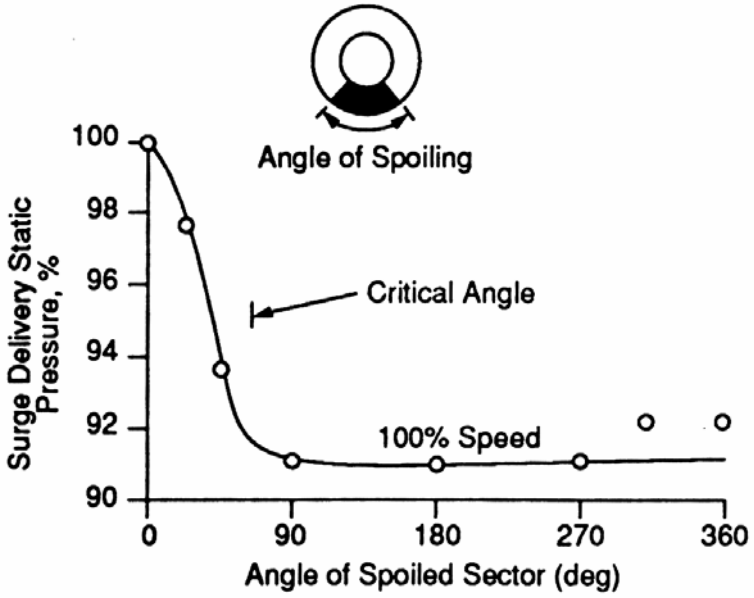

Figure 2.1. Effect of spoiled sector width [Greitzer and Longley, 1992].

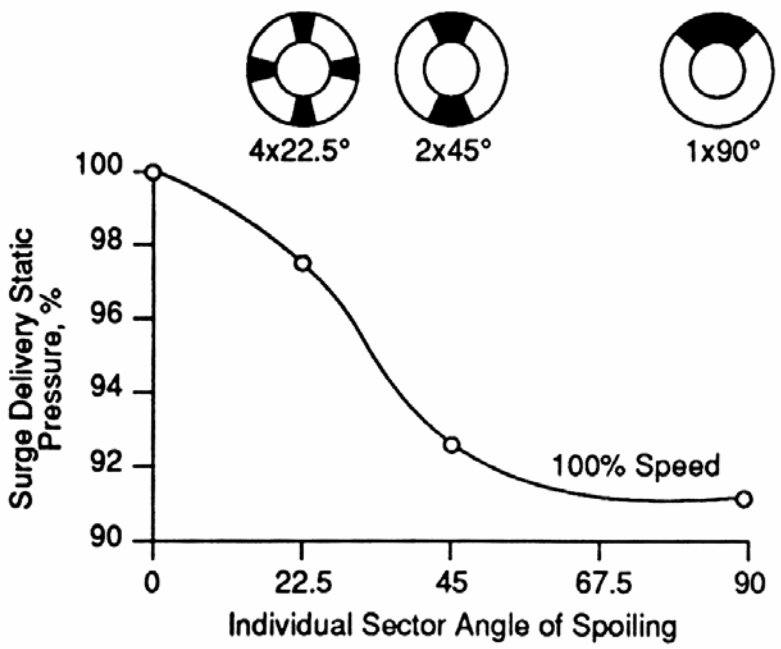

Figure 2.2. Effect of contiguous spoiled sector width [Greitzer and Longley, 1992].

Greitzer and Longley went on to define distortion indices used to quantify the extent to which a distortion affects compressor performance. Generally these indices are defined based on experimental observations. Two distortion indices are presented that emphasize the severity of the distortion in terms of the size of the total spoiled region that is below the average inlet value. The first index presented is the "K" series. This is defined as,

$$K = \frac{\overline{P}_t\big|_{360^\circ} - \overline{P}_t\big|_{\vartheta_{ext}}}{\frac{1}{2}\rho C_x{}^2}.$$

Equation 2.1

This index is a ratio of the difference in circumferential average total pressure and maximum total pressure deficit, and the incompressible dynamic pressure. The second distortion index defined is the "DC (θ_{crit})" series. This index involves the critical sector angle discussed above, and is defined as,

$$DC(\vartheta_{crit}) = \frac{P_t\big|_{360^\circ} - P_t\big|_{worst\,\vartheta_{crit}}}{\frac{1}{2}\rho C_x{}^2}.$$

Equation 2.2

This index is a ratio of the difference in circumferential average total pressure and lowest total pressure at the critical angle, and the incompressible dynamic pressure. Greitzer and Longley found that the loss of surge margin is approximately proportional to the size of this distortion index, and as a result defined a compressor sensitivity as,

$$\text{Sensitivity} = \text{loss of surge margin} / DC(\theta_{crit}).$$

Equation 2.3

Roberts, et al (1968) performed an experimental investigation into the performance of a low speed, axial compressor undergoing a 180° circumferential pressure distortion. Results of testing showed that an increase in rotor chord length increased the compressor's tolerance to distortion effects on stall margin. It was also noted that later stages of the compressor provided less attenuation of the distortion than did initial stages.

Several works concerning the aeromechanical degradation of compressor components due to non-uniform flow will now be considered.

Datko and O'Hara (1987) measured the forced vibratory response of the first stage blisk of a transonic compressor generated by a variety of inlet total pressure distortion screens. Results of the study showed the blisk to be prone to high resonant stresses resulting from the inlet distortions. Datko and O'Hara concluded that rotor forced response characteristics in the presence of uniform inlet flow are not representative of the response when a distortion is present.

Danforth (1975) established a need for distortion indices as related to the induction of blade fatigue. He proposed that distortion characteristics are relevant to assessing blade response to random vibrations in separated flow. Danforth's research showed that low blade aspect ratio trends, which generally benefit stall margin, generate the potential for resonant blade vibration where stall margin is helped most. The severity of distortion

induced blade vibration depends on the effectiveness of energy input into the blades. He showed that high-intensity distortion sectors that are too narrow to induce stall are capable of generating serious higher-order response in multistage compressor blading. As a result of these findings, Danforth suggested that an index be adopted for assessing a distortion's potential for aeromechanical effects, namely the Distortion Excitation Index for Vibration (DEIV). This index provides an early warning design alert to potential vibratory problems.

Greitzer, et al (1994) cited several effects of unsteady flow in turbomachines. Included were effects on compressor and turbine aerodynamic performance, peak turbine temperature levels, aeromechanical excitation, and compression system instability onset. In the area of aeromechanical excitation, the effects of flutter and forced response vibrations were investigated. Flutter was defined to be a self-excited aeromechanical instability while forced response vibration was defined as the response of a part to external aerodynamic forces at a resonance frequency of the part (e.g.. total pressure distortion induced blade vibrations). Greitzer, et al quoted a report on failures in military engines (Air Force Scientific Advisory Board, 1992), which stated that in the prior three decades, several hundred incidents ranging from Class A mishaps (resulting in a total of $1 million or more property damage, fatality or permanent disability, or destruction of aircraft beyond economical repair) to maintenance action have occurred. HCF was found to be the predominant cause of failure throughout these cases. Judging from the results of this investigation, forced response vibrations appeared to be the more important source of HCF when compared with flutter.

Greitzer, et al (1994) also detailed the need for further understanding of aeromechanical excitations. They noted that while resonant blade frequencies have been well predicted, the magnitudes of dynamic forcing functions that drive vibrations have not been well predicted. Also pointed out is that an important issue for multistage turbomachines is the understanding of how distortion information is passed between stationary and rotating rows, and the subsequent effect on each. The present work addresses both concerns.

2.2 Aerodynamic Performance Modeling Techniques

While finite element codes and numeric flow solvers can provide accurate predictions of compressor performance degradation resulting from distorted flow fields, they are computationally intensive and very time consuming. Because of this, simpler, less time-consuming modeling techniques have been adapted to predict compressor performance.

Delahaye and Sagnes (1984) described parallel compressor theory as the most natural and simplistic, and the most often used code for predicting compressor behavior when in the presence of distorted total pressure and total temperature flow fields. The theory operates on the principle of dividing the distorted compressor into sectors that are treated as hypothetical compressors working in parallel. An illustration of the parallel compressor theory applied to a compressor using a single distorted sector and a single clean sector is shown in Figure 2.3.

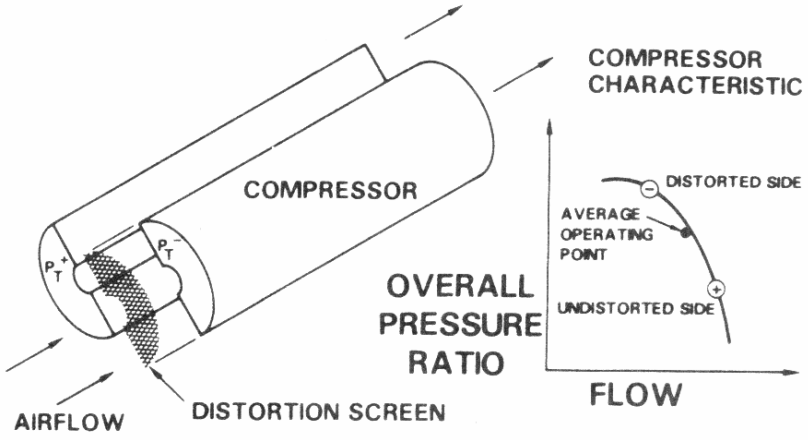

Figure 2.3. Illustration of the parallel compressor model utilizing one distorted sector [Reid, 1969].

The basic assumptions surrounding the parallel compressor theory were stated as,

- Uniform circumferential static pressure at the exit of each of the compressor sectors.
- Circumferential flow redistribution within the compressor is neglected.
- All sectors operate on the undistorted characteristics.

When one of the compressor sectors becomes stalled, the entire compressor is said to enter stall. The downfall of this theory is that static pressure circumferential gradients often exist downstream of the compressor, and parallel compressor theory is unable to account for these.

Another modeling technique is the linear actuator disk model. This model provides distorted values for pressure and velocity components both in front of and through the compressor [Delahaye and Sagnes, 1984]. Upstream conditions are solved for through a set of linear equations and assumptions, including continuity, tangential velocity at hub and tip, and developments of the potential function. A different procedure is applied for through compressor conditions. Here, the compressor is divided into vaned and vaneless spaces. For each of these a transfer function is presented, which allows for the calculation of flow characteristics at the outlet in terms of those at the inlet. Nonlinear variations of the actuator disk model exist as well.

Yet another modeling technique discussed by Delahaye and Sagnes is the blade cascade model. This model predicts unsteady turning and losses in cascades resulting from upstream flow non-uniformities. Blade cascade modeling is based on potential flow theory. A benefit of this model is that it does not require velocity perturbations to be small.

Small (2001) presented an enhanced frequency response function modeling technique for the prediction of total pressure distortion propagation through a transonic compressor rotor. This work serves as the predecessor of the current study. Small entitled this technique the "Tuned FRF Method", as frequency response functions are "tuned" to the operating conditions and properties of the inlet flow field at which predictions are taking place. Frequency components of a prediction are adjusted based on several factors including:

- Distortion intensity
- Rate of change in total pressure as seen by blade row
- Blade passage shock strength
- Fluid axial velocity
- Blade chord length

Small introduced a new parameter in his study called reduced distortion rate (RDR), which serves as an improved form of reduced frequency. RDR is based on the time domain characteristics of inlet distortion, rotor speed, and fluid velocity. Results of Small's tuned FRF predictions will be included in the results of the current study presented in Chapter 7 for means of comparison.

2.3 Nonlinear Volterra Theory as an Aerodynamic Response Modeler

Traditionally nonlinear Volterra theory has been used as a response modeler in electrical and biological systems engineering. However, in the past decade it has seen more and more use in the field of aerodynamic response modeling. The focus of much of the work done in this area has been on methods of measuring Volterra kernels in order to create system representations. A variety of techniques to do so exist and will be discussed here.

As early as 1983 Boyd et al [Boyd, et al, 1983] developed a method of measuring second order Volterra kernels for the purpose of modeling response behavior systems where the nonlinearities are subtle. Examples of such systems are high quality transformers, electro-mechanical and electro-acoustic transducers, and simple communications systems. While the work of Boyd, et al, was not specifically related to aerodynamic response modeling, it is cited by others in this field as the basis of other modeling techniques. Boyd, et al, presented a multitone harmonic probing technique for measuring the 2^{nd} order Volterra kernel of an electro-acoustic transducer. This method applied a signal to the transducer at two or three levels and used an interpolation method

to estimate the second-degree component of the system response, which yielded a measurement of the 2nd order Volterra kernel.

Jenkins and Tromp (1990) applied a Volterra kernel identification scheme to the problem of modeling lift response to angle-of-attack over a 2-D airfoil. The pencil of functions (POF) method was used to determine the linear, 1st order Volterra kernel from lift response data generated by an unsteady Navier-Stokes solver. The POF method relies on finding the proper magnitude of an input such that only the linear portion of the response is excited. This was accomplished by choosing sufficiently small angles-of-attack to insure linear behavior. A set of "pencil functions" were generated by performing successive integrations on the input and output time histories and assembling the inner products of these functions into a Gram matrix. The poles and residues of the matrix were then identified and used to solve for the linear kernel in the form of

$$h_1(s) = \sum_{i=1}^{N} R_i (s - \lambda_i)^{-1}$$

Equation 2.4

where λ_i are stable, nonzero poles, R_i the residuals, and s the Laplace operator. Exciting the system such that third order effects and above were negligible allowed for identification of the 2nd order kernel. Subtracting the linear response from the total response then identified the second order system response.

Silva (1993) presented the method of unit impulse responses as applied to nonlinear aerodynamic responses. In this method, systems were modeled in state space form while kernels were extracted from the system output when excited by a unit impulse. Results of this technique were provided indicating excellent agreement between predicted and measured system response. Later Silva (1997) furthered his investigation into the use of nonlinear Volterra theory in aerodynamic response modeling, establishing the aerodynamic impulse response function as "the most fundamental, and, therefore, the most computationally efficient, aerodynamic function that can be extracted from any given discrete-time, aerodynamic system." Silva then went on to illustrate that the multidimensional impulse response function is the basis of nonlinear Volterra theory.

While all previous Volterra kernel extraction techniques have been based on very specific input structures, Reisenthel (1999) developed a unique time-domain kernel extraction technique that is said to use physically realizable inputs, be robust with respect to noise, and minimize or eliminate the need for analytical assumptions. The technique presented relies on the expansion of Volterra kernels into basis function space, which is bound by known system behavior in the form of measured input and response data. The extraction method was applied to the aerodynamics of a wing dynamically pitched about its quarter chord location with accurate results. Reisenthel lists a series of quality assurance steps that should be taken to ensure that the true underlying system kernels have been identified. These include,

- Check that data used for identification can be reproduced using the extracted kernels.
- Check that the linear impulse response resulting from simultaneous identification of 1^{st} and 2^{nd} order kernels using nonlinear data matches the result of 1^{st} order only extraction based on linear data (if necessary data is available).
- Results should converge to the same kernels as the training data set is progressively enriched.
- Verify that extracted kernels can predict novel data not included in the training.

This method of kernel extraction presented by Reisenthel is the motivation behind the method presented in the current study, and will be discussed in depth in Chapter 5.

2.4 Conclusions Drawn from Literature Review

As seen throughout this literature review, a general understanding of the effects of flow non-uniformities on compressor performance exists. However, there is a need for further developments and understanding, particularly in the area of aeromechanical distortion effects. Several works have been presented which outline the potential effects of distortion induced blade excitation. An excerpt from an Air Force Scientific Advisory

Board report on engine failures due to HCF has been provided, which illustrates the severity of distortion effects already realized.

A brief history of the use of nonlinear Volterra theory in aerodynamic response modeling has also been presented. While only few applications have been made in this area, a general trend leading to the use of Volterra theory in the current study is evident.

3 An Introduction to Nonlinear Volterra Theory

3.1 Nonlinear Volterra Theory

Nonlinear Volterra theory was developed in the 1880s by Vito Volterra and later introduced to the mathematical community in a series of lectures entitled *Theory of Functionals and of Integral and Integro-Differential Equations* [Schetzen, 1980]. The theory quickly received a great deal of attention in the field of electrical engineering, and then later in the biological field, as a powerful approach to the modeling of nonlinear system behavior.

Volterra theory is a generalization of the linear convolution integral approach often applied to linear, time-invariant systems. The theory states that any time-invariant, nonlinear system can be modeled as an infinite sum of multidimensional convolution integrals of increasing order. This is represented symbolically by the series of integrals,

$$y(t) = \int_0^\infty h_1(\tau_1)x(t-\tau_1)d\tau_1 + \int_0^\infty\int_0^\infty h_2(\tau_1,\tau_2)x(t-\tau_1)x(t-\tau_2)d\tau_1 d\tau_2 + \ldots$$
$$+ \int_0^\infty \ldots \int_0^\infty h_n(\tau_1,\ldots,\tau_n)x(t-\tau_1)\ldots x(t-\tau_n)d\tau_1\ldots d\tau_n \,,$$

Equation 3.1

which is known as the Volterra series. Here, x (t) represents the dynamic system input while y (t) represents the system response. Volterra theory is based on dynamic data, and as such the average values of all input and response data sets are removed. Each of the convolution integrals contains a kernel, either linear (h_1) or nonlinear ($h_2,\ldots,h_n$), which represents the behavior of the system. Knowledge of these kernels allows the prediction of a system's response to any arbitrary input, and as such is critical to nonlinear Volterra modeling. The first term of the series represents the linear convolution integral. As seen for a third order Volterra series in Figure 3.1, each of the terms in the series is superposed

to form the system output. The first order term is considered to represent the mean of the system response. All higher-order terms then represent a higher-order variation about this mean.

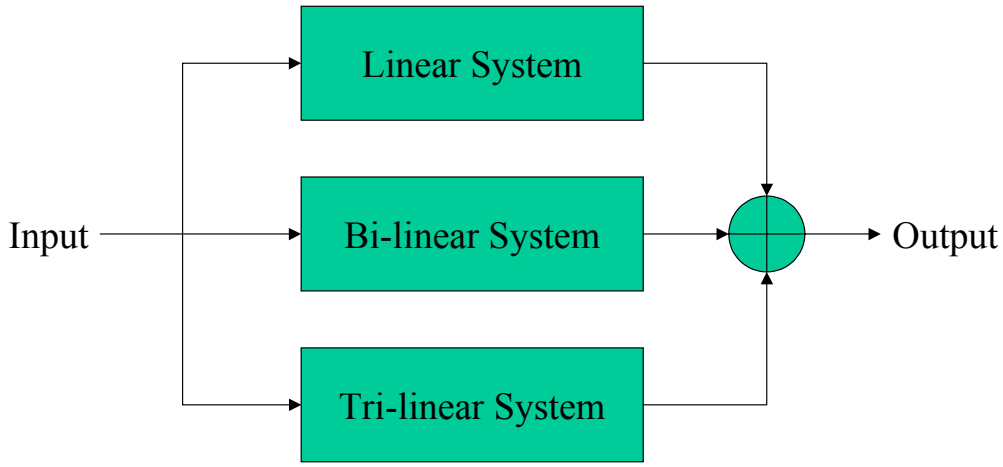

Figure 3.1. An illustration of the superposition of terms in a 3rd order Volterra series.

Low-order nonlinear systems can often be accurately represented by a truncated Volterra series. Such systems are deemed weakly nonlinear. The term weakly nonlinear merely implies that a system is well represented by the first two or three terms of a Volterra series. All higher-order terms in this situation are seen to quickly tend toward zero, and are therefore negligible in the system representation. By extending the concept of weakly nonlinear systems, the Volterra series can be thought of as a test of non-linearity. As an example, consider a completely linear system that is represented solely by the first-order convolution integral of the series. The kernels of all higher-order terms have zero response due to the lack of non-linearity in the system response. Because of this, the existence or nonexistence of higher-order kernels, h_2 through h_n, can be seen as a measure of the degree of a system's linearity. In the same way, this reasoning can be used to establish bounds beyond which the assumption of linearity begins to fail.

While Volterra theory has a strong foundation in both the biological and electrical engineering fields, it has received little attention in the field of aerodynamics until recently. Linear response models have often been assumed sufficient for representation of nonlinear aerodynamic systems when excited by small perturbations. This assumption derives from the fact that highly nonlinear phenomena have a negligible impact on the net

effect of various responses under conditions such as small perturbation excitation [Silva, 1997]. In addition, the lack of attention is due in large part to the inherent difficulty of identifying Volterra kernels. Several experimental kernel identification methods exist which, while easily accomplished in an electrical application, are both impractical and unrealistic in an aerodynamic sense.

3.2 Volterra Kernels

Volterra kernels are the backbone of any Volterra series. Knowledge of a system's behavior is contained within these kernels, and given any arbitrary input the Volterra series can predict the response of the system. Volterra kernels, both linear and nonlinear, are input dependent. As an example of this consider the case where the response of a linear system to an arbitrary input is desired. Here, the unit impulse response of the system to that type of input must first be defined [Silva, 1993].

The first order kernel, $h_1(\tau)$, represents the linear unit impulse response of the system. This term is comparable to the basic frequency response function (FRF) of a linear system, transformed into the time domain. However, the kernel h_1 gives a more accurate portrayal of a system's linear response than does the FRF. This is because h_1 exists with the knowledge of higher-order, nonlinear terms while the FRF assumes a completely linear response.

The second order kernel, $h_2(\tau_1,\tau_2)$, is a two-dimensional function of time. It represents the response of the system to two separate unit impulses applied at two varying points in time. Therefore the kernel is a function of both time and time lag. Similarly, $h_3(\tau_1,\tau_2,\tau_3)$ is a three-dimensional function of time, representing the response of the system to three separate unit impulses applied at three varying points in time. Here the kernel is a function of time and two distinct time lags. It is through these time lags that nonlinear kernels represent the effect of a previous response as it is carried through time in the system.

Volterra kernels can be rewritten in several ways simply by reordering the variables of integration. Because of this, more than one kernel can generally be used to

describe a given system, and it is therefore necessary to impose uniqueness upon the kernels. This is accomplished by working with restricted forms of the kernels. Three such forms exist, including symmetric, triangular, and regular. Here, the symmetric kernel will be focused on. Rugh shows that the kernel of a homogeneous system can be assumed symmetric without the loss of generality [Rugh, 1981]. A symmetric kernel is one in which the choice of the time lag variables, τ, is arbitrary, and as such these variables are in fact dummy variables. Given in terms of the bilinear kernel, a symmetric kernel is one in which

$$h_2(\tau_1, \tau_2) = h_2(\tau_2, \tau_1).$$

Equation 3.2

The method used to impose symmetry on extracted kernels in the present work will be discussed further in Section 5.6.

3.3 Memory Functions

Nonlinear Volterra kernels are said to represent the "memory" of a system. That is, they act as measures of the relative influence of a previous input on the current response of the system. This memory is in fact a temporal measure of non-linearity, and because of this Volterra systems are often referred to as nonlinear systems with memory [Silva, 1997]. The memory of a linear system is commonly defined by the system's impulse response. Volterra theory then extends this concept to nonlinear systems by means of nonlinear kernels and multidimensional impulse responses.

3.4 Requirements for a Volterra Series

Three conditions exist which must be satisfied when defining a Volterra series. The first of these is that the kernels, input function and output function must be real valued functions over all time. The second condition requires the system being modeled

to be causal. A causal system is one that, for any input, the response at any instant in time does not depend on the future of the input. The final condition to be satisfied requires that a system be time-invariant. A time-invariant system is one for which the operator does not vary with time. By this it is implied that a time shift of the input will result in the same time shift in the output [Schetzen, 1980]. The fundamental properties of a time-invariant system do not change with time. As most real world systems satisfy each of these conditions, they can be considered as merely academic.

4 Experimental Data

4.1 Experimental Testing

All experimental testing and data collection for this study has taken place at the Compressor Research Facility (CRF) at Wright Patterson Air Force Base, OH. CRF houses a two stage, transonic, low aspect ratio compressor of modern design, which will be the focal point of this investigation. A summary of the "Experimental Procedure and Data Acquisition" portion of Matt Small's thesis [Small, 2001] will be provided here as an overview of the experimental methods applied.

The two-stage compressor described above is contained in a test section as illustrated in Figure 4.1. The test section is of an open loop design with atmospheric air drawn into the facility by the compressor. The test chamber is 20 feet in diameter and 65 feet long. Compressor inlet air pressure is controlled by a series of filters and valves located upstream of the test chamber. Inlet air is then straightened through flow conditioning elements downstream of the chamber. Two 30,000 hp synchronous electric drive motors drive the compressor through high and low speed gearboxes.

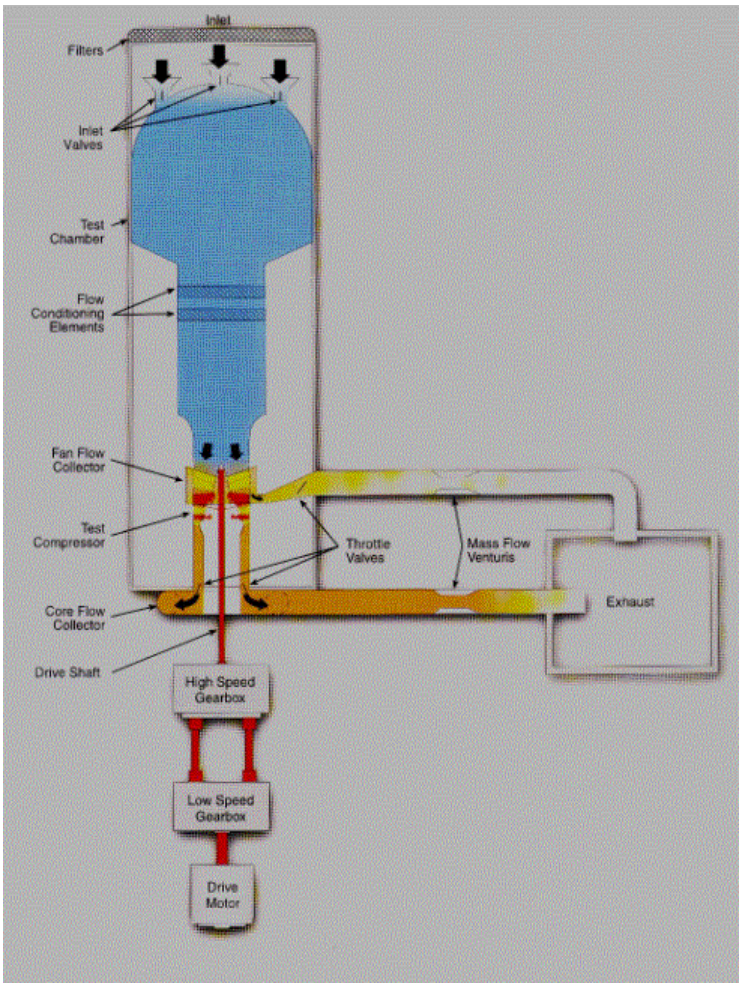

Figure 4.1. Compressor test facility located at the CRF, Wright Patterson AFB [Morrow, 1993].

The compressor used in this study contains a first stage blisk (modern integrally bladed disk), which will be the emphasis of the majority of this investigation. A picture of the blisk is shown in Figure 4.2. The blisk consists of 16 low aspect ratio blades of modern design. At design operating conditions relative rotor velocities are supersonic above 45% span for inlet temperatures near 300 K. The geometric parameters characteristic of this rotor are provided in Table 4.1. The second stage rotor is mounted on a disk using a conventional dovetail arrangement. This rotor consists of 40 blades, and is shown in Figure 4.3.

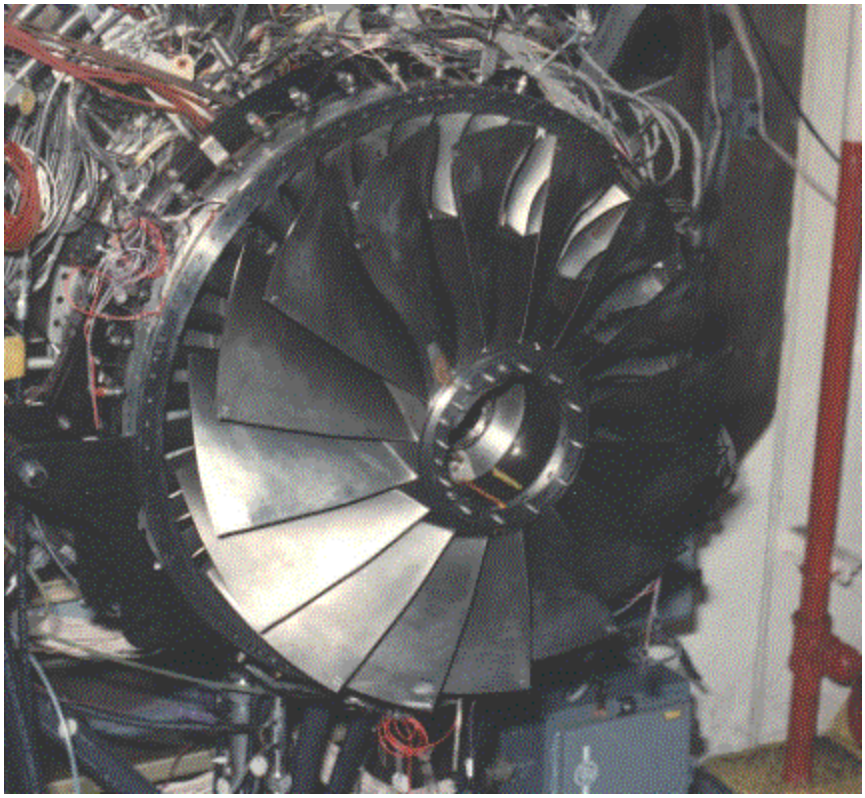

Figure 4.2. First stage blisk mounted on test rig [Morrow, 1993].

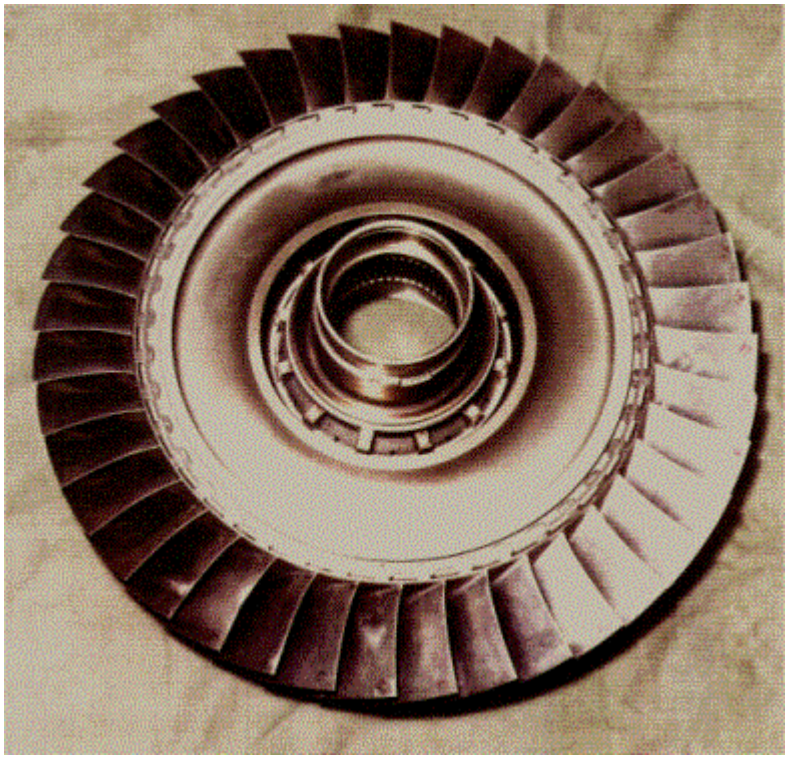

Figure 4.3. Second stage rotor [Morrow, 1993].

Table 4.1 Rotor 1 Geometry [Rabe et al, 1999]

Parameter	Value
Average Aspect Ratio	1.22
Rotor Tip Radius (in.)	13.87
Inlet Radius Ratio	0.33
Average Radius Ratio	0.47
Average Tip Solidity	1.50
Maximum Thickness/Chord	0.028

A schematic of the test setup used in this experiment is shown in Figure 4.4. As seen here, a distortion-generating device is installed approximately 1.5 diameters upstream of the leading edge of the first stage rotor. This test setup does not incorporate inlet guide vanes (IGVs), but does include stator rows immediately downstream of Rotor 1 and Rotor 2. Total pressure measurement locations exist approximately one diameter upstream of the first stage rotor leading edge, along Stator 1 leading edge, and along Stator 2 leading edge. Various other instrumentation such as thermocouples and static pressure taps were present in the test cell during data collection, however this information is not used in the current investigation and therefore will not be discussed here.

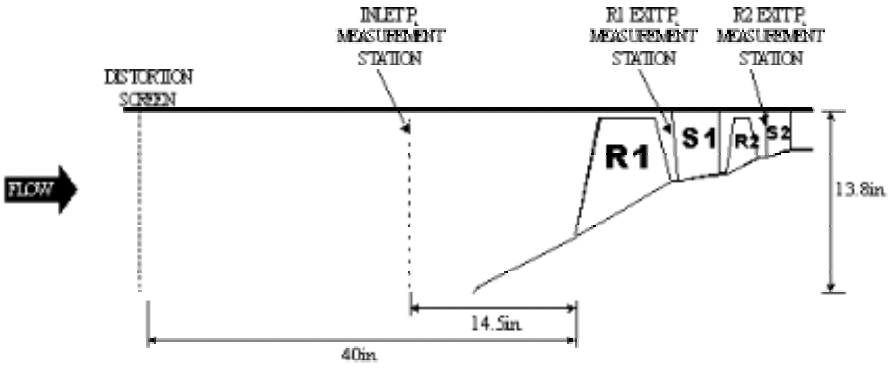

Figure 4.4. Experimental test setup [Morrow, 1993].

4.2 Total Pressure Distortion Generation

As depicted in Figure 4.4, a total pressure distortion generating device is located upstream of the compressor inlet. The distortion generator consists of a wire mesh screen of varying porosity, which creates downstream regions of reduced axial velocity. These regions of reduced axial velocity correspond directly to regions of reduced total pressure. Distortion screens are created so as to impose a circumferentially sinusoidal, steady state distortion. In this experiment, screens consisting of 3 distortions per revolution (3 per rev) and 8 distortions per revolution (8 per rev) were used. An example of a 3 per rev distortion screen is shown in Figure 4.5.

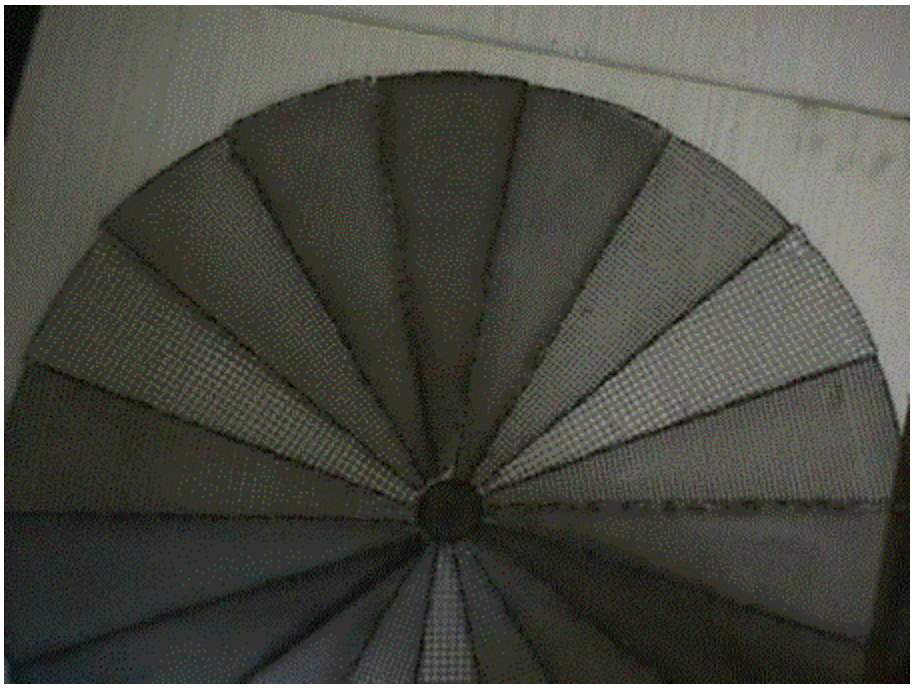

Figure 4.5. 3 per rev distortion screen [Morrow, 1993].

The distortion generator used in this experiment is equipped with a mechanical screen rotator. The screen rotator consists of backup screen radial struts and a drive motor located outside of the flow path. A picture of the screen rotator is shown in Figure 4.6. Screen rotation allows for high spatial circumferential data resolution from a small number of probes. However, use of a rotating screen requires a slow enough rotation

speed so that the distortion pattern is quasi-steady as it passes through the rotor. Williams (1999) determined that a rotation rate of approximately two degrees per second is sufficient for this compressor to consider the distortion pattern quasi-steady.

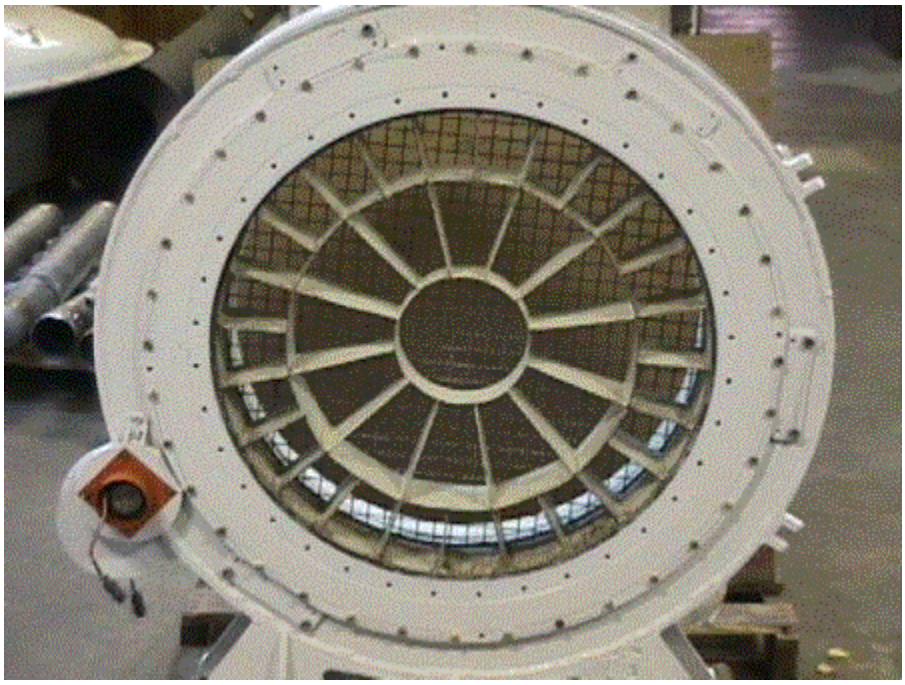

Figure 4.6. Distortion screen rotator [Morrow, 1993].

Rotating the distortion screen and implementing stationary pressure probes create time-series total pressure histories in the rotor coordinate frame. Time-series histories are easily transformed into spatial histories in the rotor coordinate frame with knowledge of the rotor's rotational speed and the radial position of the time-series.

4.3 Total Pressure Measurements and Data Reduction

Small carried out the majority of raw data reduction necessary for this study as part of his M.S. thesis [Small, 2001]. As such, a summary of experimental measurement locations and data reduction procedures from Small's thesis will be provided. For further information, the reader is referred to the original document.

Inlet total pressure measurements were taken 14.5 in. upstream of Rotor 1 leading edge. This was accomplished through eight total pressure radial rakes consisting of five radial immersions each. The rakes were equally spaced about the circumference of the test cell with radial immersions located on centers of equal mass flow annuli. Inlet radial immersions are provided in Table 4.2.

Table 4.2 Inlet Total Pressure Rake Radial Immersions [Morrow, 1993]

Immersion	Radial Distance from O.D. (in).
1	0.74
2	2.31
3	4.11
4	6.33
5	9.57

Rotor 1 and Rotor 2 exit total pressure measurements were made along the stator leading edge of each respective stage. At Rotor 1 exit, three circumferentially equally spaced stator vanes were instrumented with total pressure probes at seven radial immersions. Stage 1-probe measurement locations are shown in Table 4.3. A sample illustration of an instrumented stator vane representative of both first and second stages is shown in Figure 4.7. The seven total pressure probes located along the radius of the stator are apparent in this figure. The configuration of total pressure probes along the second stage stator is similar to that of the first stage. Probe locations in stage two are provided in Table 4.4.

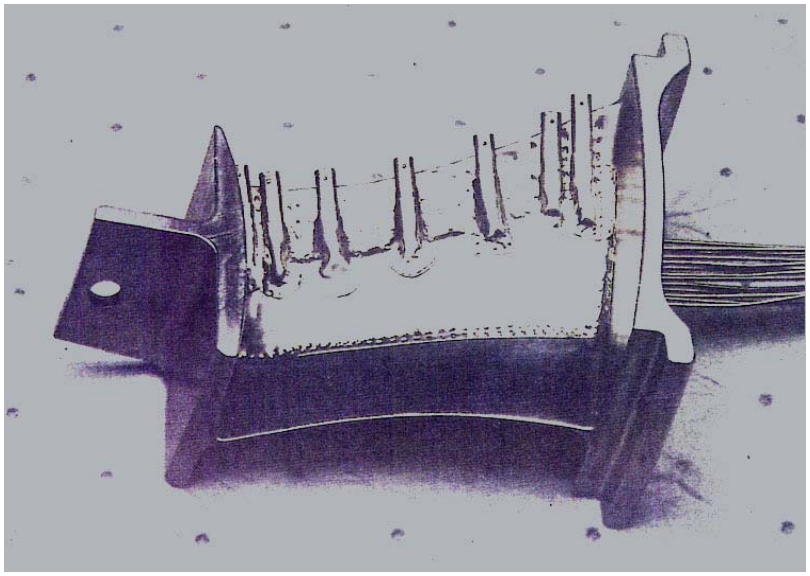

Figure 4.7. Instrumented stator vane [Morrow, 1993].

Table 4.3 First Stage Stator Leading Edge Probe Locations [Morrow, 1993]

Immersion	Radial Distance from O.D. (in.)	Axial Distance from R1 LE (in.)
1	0.315	6.60
2	0.662	6.80
3	1.577	7.05
4	2.577	7.27
5	3.573	7.29
6	4.241	7.16
7	4.595	7.10

Table 4.4 Second Stage Stator Leading Edge Probe Locations [Morrow, 1993]

Immersion	Radial Distance from O.D. (in.)	Axial Distance from R2 LE (in.)
1	0.271	13.07
2	0.479	13.12
3	0.903	13.22
4	1.479	13.30
5	2.011	13.30
6	2.430	13.26
7	2.650	13.22

Data taken for this study were sampled several times per second, creating close to 900 circumferential measurements. This corresponds to one measurement every 0.35 – 0.40 degrees per probe. This data was then reduced to 360 equal circumferentially spaced measurements. Because the probes were not phase locked, measurements were taken at varying points in time by each probe. This necessitated each data point to be rounded to the nearest degree (in spatial coordinates). Small then averaged probe measurements over each degree of the circumference. Averaging the probe measurements actually served as a high frequency filter for the data, eliminating some high frequency content on the order of 100 per rev.

In this study it is desired to follow total pressure propagations through a rotor along continuous streamlines. This is necessary for understanding the behavior of an individual distortion pattern as it travels through the rotor. In order to accomplish this Small applied a streamline curvature (SLC) code to the data sets. SLC is an iterative procedure based on the governing equations of continuity and momentum, which calculates streamline radial positions through turbomachinery stages. It is based on several flow assumptions, including steady, adiabatic, inviscid, and axisymmetric with negligible body forces. For more detail on the SLC method the reader is referred to Boyer, 2001.

An enhanced form of SLC code developed by Boyer was used to calculate streamline positions in this study. Streamline positions upstream of Rotor 1 were chosen

as centered on annuli of equal mass flow. Because the mass flow upstream of Rotor 1 was radially uniform and purely axial, equal mass flow annuli corresponded to the equal area annuli pressure probe locations at this position. In Boyer's code, 19 axial streamline positions were calculated and followed through each stage of the compressor. The five streamlines corresponding to the five inlet pressure probe locations were chosen for use in this study. An illustration of the streamline positions through the compressor is shown in Figure 4.8.

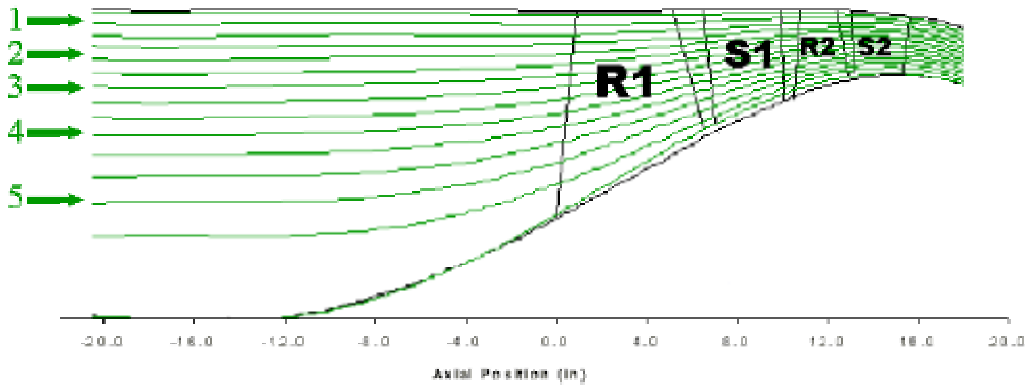

Figure 4.8. SLC computed streamline positions through the compressor [Small, 2001].

Because nonlinear Volterra theory operates on the dynamic content of data sets, all average total pressures from each data set were removed. Because of this only variations in total pressure will be considered. The impact of this action on this study is not at all negative, as it is the changes in total pressure that serve as HCF drivers.

4.4 Data Characteristics

Total pressure distortion data sets were collected at eleven individual operating points of the compressor, along three separate speed lines (note that all total pressure measurements are in units of psi.) These speeds include 9100 rpm, 9500 rpm, and 13200 rpm, which correspond to 68.5%, 71.5%, and 99.3% of design speed, respectively. At each speed four mass flow settings were recorded. These include normal operating line

(NOL), near stall (NS), peak efficiency (PE), and wide-open discharge (WOD). Note that NS and PE operating points along the 13200 rpm speed line are coincident, and as such only three data sets exist at 13200 rpm. An operating map of the compressor under investigation is shown in Figure 4.9. This map includes operating points with both distorted and clean inlets. Notice the apparent loss in pressure ratio and mass flow due to the distorted inlet.

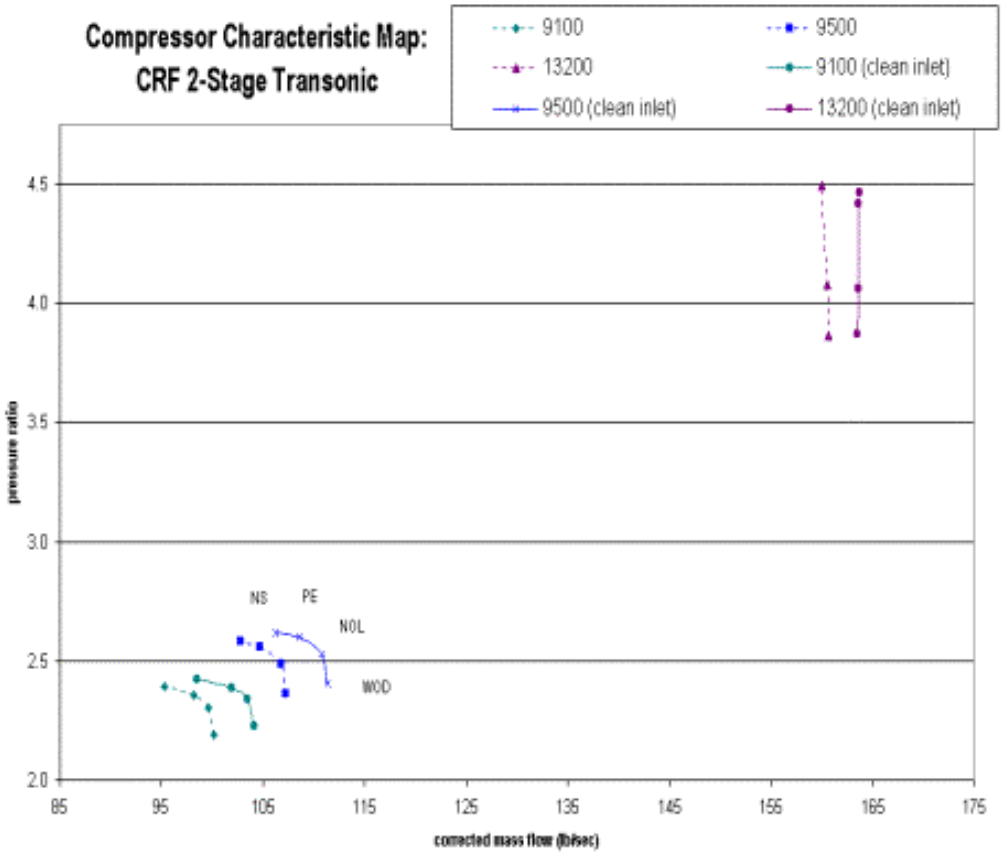

Figure 4.9. Compressor operating map, including both distorted and clean inlet conditions [Small, 2001].

As noted in the previous section, five streamlines from the SLC prediction have been chosen for examination in this study. Each of these streamlines corresponds to a radial immersion on the inlet total pressure probe rakes. Therefore, these streamlines will be referred to as radial immersions 1 through 5 (RI1, RI2, RI3, RI4, RI5) throughout the remainder of this study. Note that RI1 will always represent the near tip radial immersion

while RI5 will always represent the near hub radial immersion. The exact positions of the radial immersions will, however, vary between operating points due to varying mass flows and the resulting SLC streamline locations.

As mentioned previously, two distortion types have been applied to the compressor, 3 per rev and 8 per rev. 3 per rev distortions correspond to the 9100 rpm speed line while 8 per rev distortions correspond to the 9500 rpm and 13200 rpm speed lines. A summary of operating conditions at the NOL condition is provided in Table 4.5.

Table 4.5 Compressor Characteristics at NOL [Small, 2001]

Distortion Type	3 per rev	8 per rev	8 per rev
Max. P_t Variation from Mean	3%	6%	18%
Mechanical Speed (rpm)	9100	9500	13200
Percent Rotor Speed	69%	72%	99%
Pressure Ratio	2.3	2.5	4.1
Percent Corrected Mass Flow	63%	67%	103%

A typical 3 per rev distortion pattern upstream of Rotor 1 is shown in Figure 4.10 as a color contour plot. Note that variations about the mean total pressure are presented. The 3 per rev distortion pattern is clear in this figure, with three high-pressure areas (indicated in red) and three low-pressure areas (indicated in dark blue) creating a sinusoidal pattern with smooth transitions between peaks. Time-series representations of the same distortion pattern broken into radial immersions are shown in spatial coordinates in Figure 4.11.

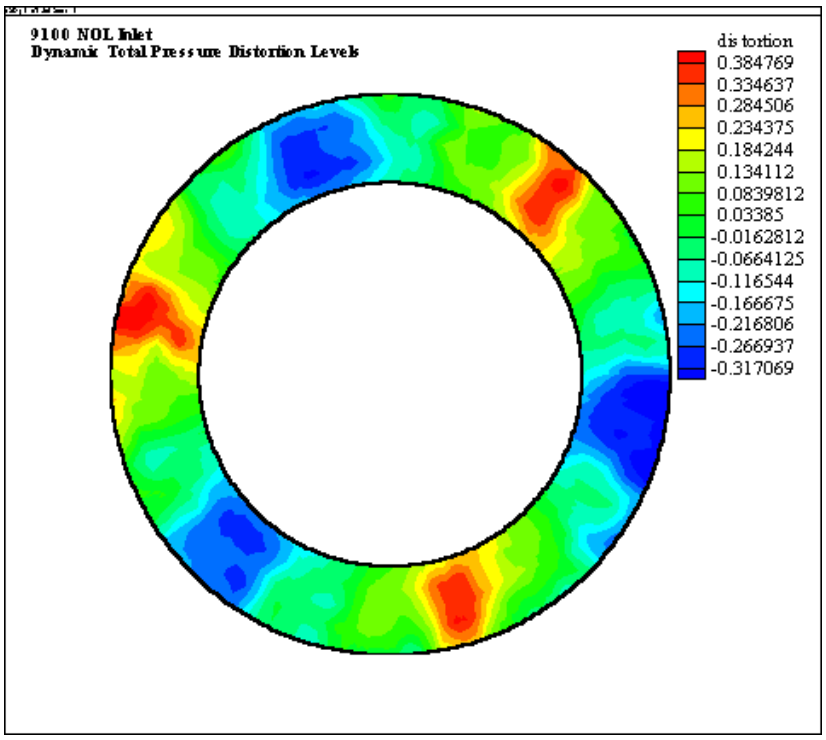

Figure 4.10. Inlet 3 per rev dynamic total pressure distortion pattern at 9100 NOL operating condition.

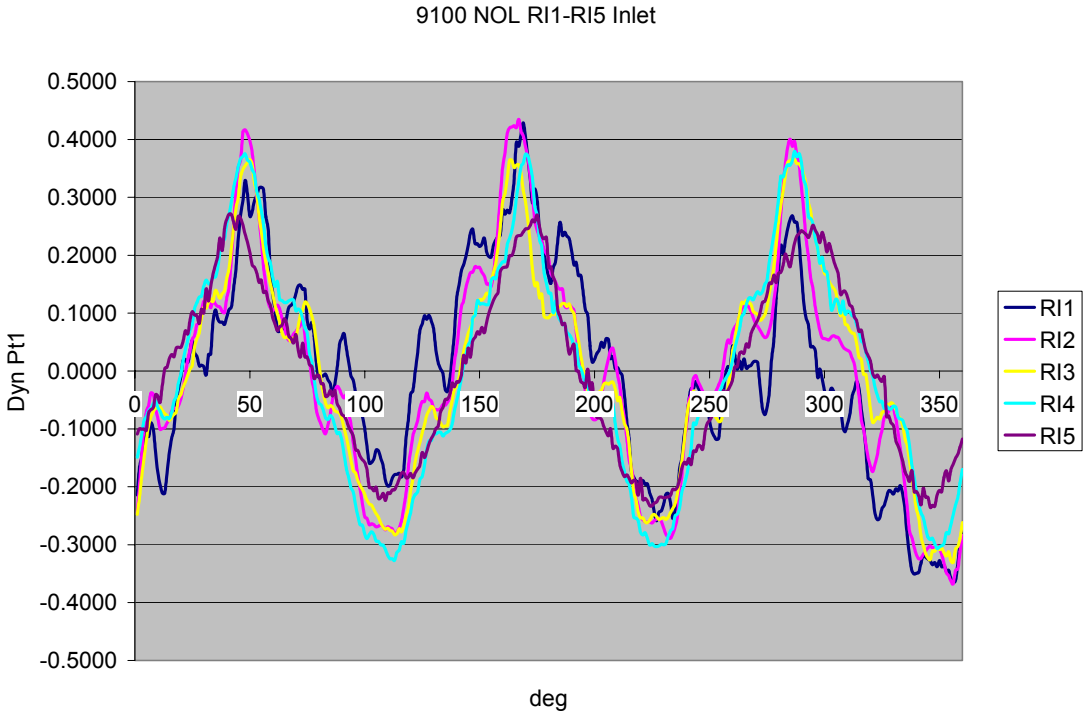

Figure 4.11. Time-series inlet dynamic total pressure profiles at 9100 NOL operating condition.

Time-series total pressure profiles downstream of Rotor 1 at the 9100 NOL condition are presented in Figure 4.12. Notice that a strong distortion pattern still exists after traveling through the first stage rotor, establishing a non-uniform inlet flow for the next stage. The frequency magnitudes of the first 24 harmonics of the downstream distortion patterns of each radial immersion are shown in Figure 4.13. Here the characteristic 3rd harmonic of this distortion pattern is seen as the dominant frequency magnitude. The higher harmonics of the dominant distortion frequency (6, 9, 12, etc.) also show significant magnitudes. Note that the zero harmonic, or DC component, has no magnitude at all. This is a result of removing the average (DC component) total pressure from each data set.

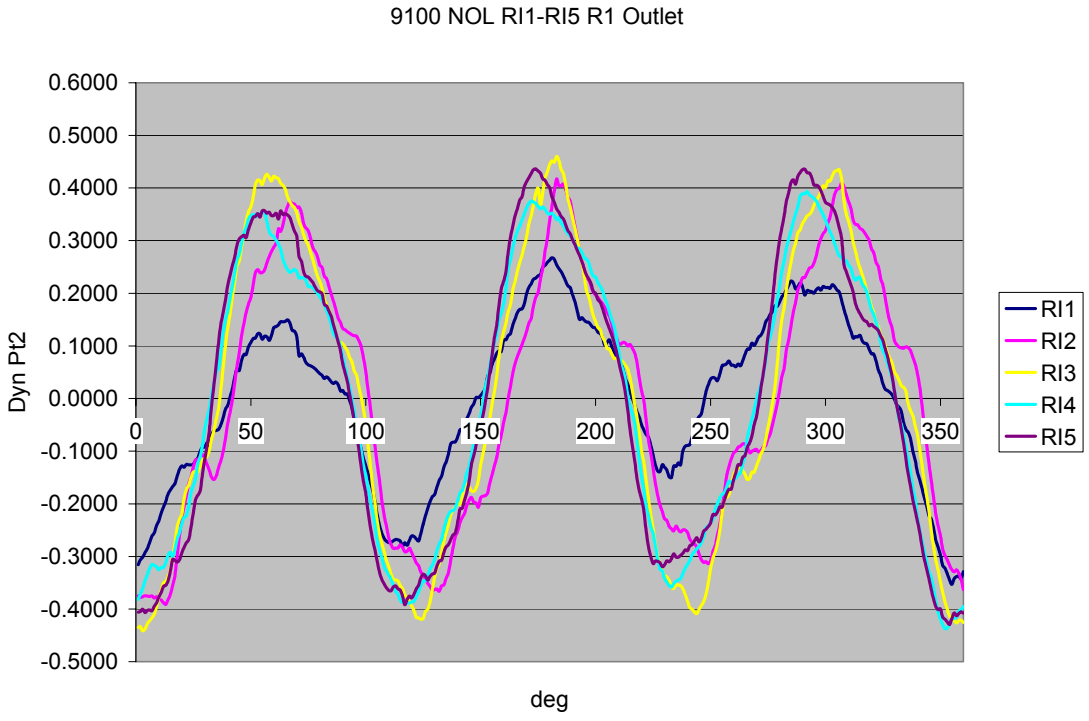

Figure 4.12 Time-series dynamic total pressure profiles downstream of Rotor 1 at 9100 NOL operating condition.

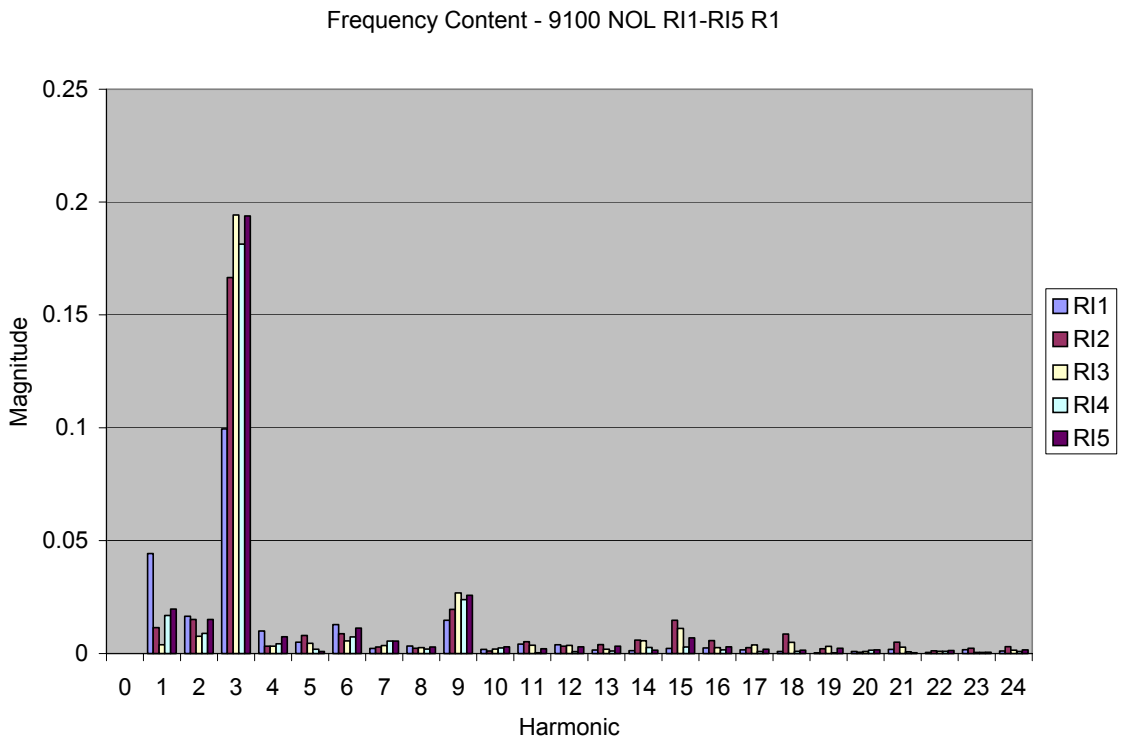

Figure 4.13. 9100 NOL RI1-RI5 frequency content downstream of Rotor 1.

A typical 8 per rev distortion pattern upstream of Rotor 1 along the 9500 rpm speed line is shown in Figure 4.14. Again, dynamic total pressures are presented. Here the 8 per rev distortion pattern is apparent with eight high-pressure areas (indicated in red) and eight low-pressure areas (indicated in dark blue) creating the sinusoidal pattern. Again, smooth transition between peaks is apparent. Figure 4.15 shows time-series distortion patterns for the same condition in spatial coordinates at each radial immersion. Inlet total pressure profiles along the 13200 rpm speed line are similar to those shown for the 9500 speed line.

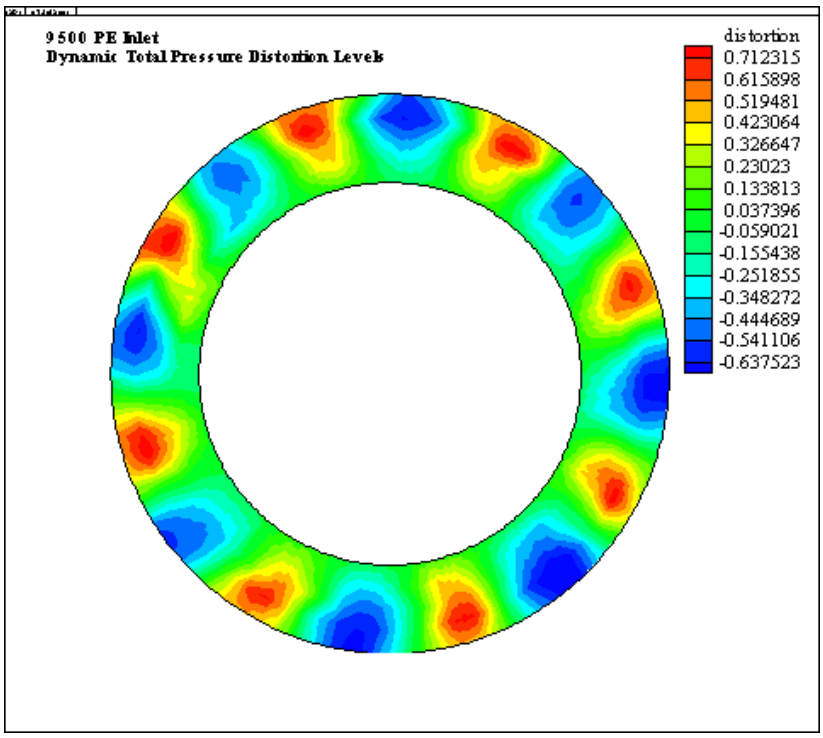

Figure 4.14. Inlet 8 per rev dynamic total pressure distortion pattern at 9500 PE operating condition.

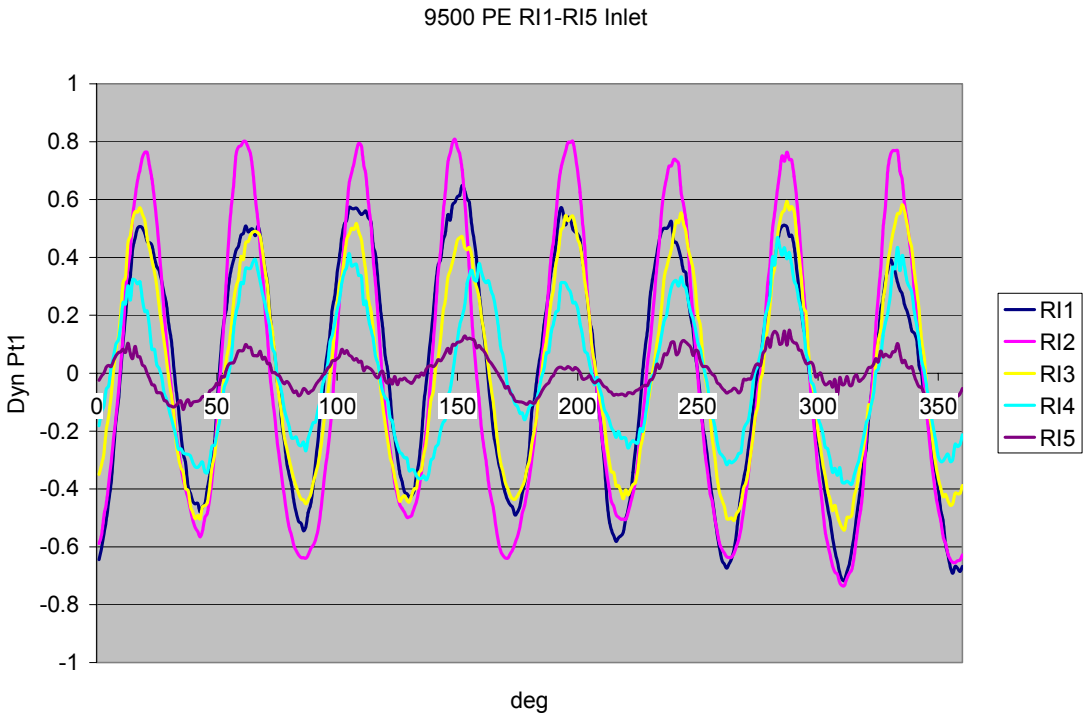

Figure 4.15. Time-series inlet dynamic total pressure profile at 9500 PE operating condition.

Time-series total pressure profiles downstream of Rotor 1 at the 9500 PE condition are now presented in Figure 4.16. Notice again that a diminished, however considerable, total pressure distortion exists downstream of the rotor. The inlet distortion pattern at this condition is seen to vary in intensity from hub to tip, however the outlet distortion pattern exhibits fairly consistent distortion intensity. The frequency magnitudes of the first 24 harmonics of the total pressure distortion profile at each radial immersion are presented in Figure 4.17. Here the eighth harmonic is the dominant distortion magnitude, as is characteristic of an 8 per rev distortion pattern. The harmonics of the dominant distortion frequency (4, 16, etc.) show significant distortion magnitudes as well.

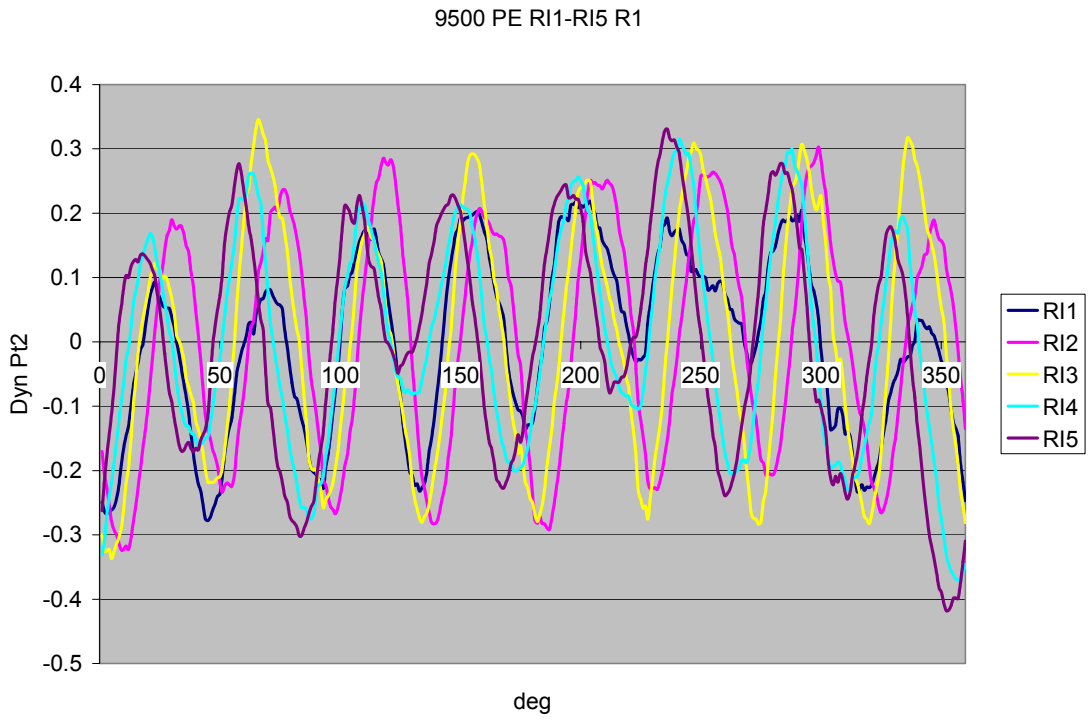

Figure 4.16. Time-series dynamic total pressure profiles downstream of Rotor 1 at 9500 PE operating condition.

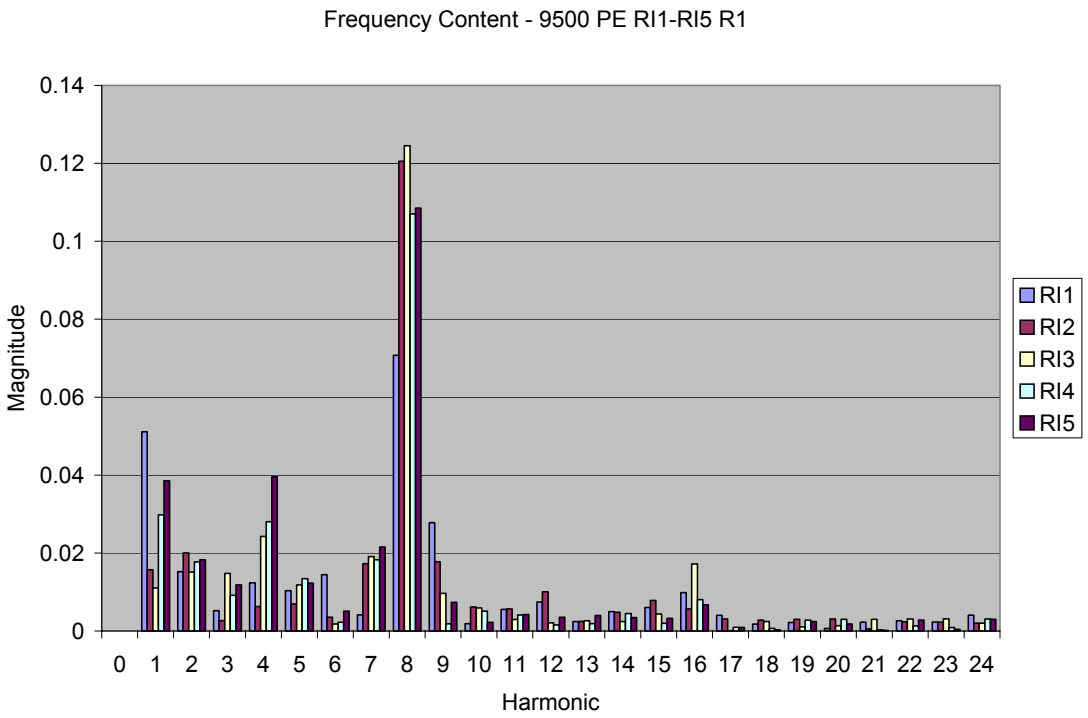

Figure 4.17. 9500 PE RI1-RI5 frequency content downstream of Rotor 1.

5 Identifying Volterra Kernels

5.1 Existing Volterra Kernel Identification Methods

The key to system modeling by means of a Volterra series is capturing the Volterra kernels that represent the system. Once the kernels are known, the system response to any arbitrary input can be predicted with relative ease. Therefore the success of nonlinear Volterra system modeling is dependant on the ability to accurately identify Volterra kernels. Unfortunately, kernel identification is a difficult process, which has been studied for some time. Several identification methods do exist; however most do not allow kernel identification from generic experimental data. Of the existing methods that do extract Volterra kernels from experimental data, all rely on specific system excitations, such as unit impulses, which are not applicable to wind tunnel or flight test models. Reisenthel notes that there appears to be an inverse relationship between accuracy and physical realizabilility amongst existing Volterra kernel identification methods [Reisenthel, 1999].

Reisenthel has created a kernel extraction technique, which uses physically realizable inputs and is applicable to existing experimental data [Reisenthel, 1999]. This technique serves as the motivation for the kernel identification method presented in the current study. For this work, a weakly nonlinear, third order Volterra series will be derived for the prediction of downstream total pressure distortion patterns.

5.2 Volterra Kernel Identification Method

Volterra series exist in both the frequency and time-domains. Therefore, at the onset of this study a choice had to be made as to the domain the Volterra series would be constructed in. Silva states that it is preferable to work in the time-domain since unsteady, nonlinear CFD analyses (often providing the data for system modeling) are generally performed in the time-domain [Silva, 1993]. However, Boyd, et al, chose to

work in the frequency domain for two stated reasons: 1) ease of accurately measuring frequency-domain kernels over time-domain Volterra kernels when the non-linearities are subtle, and 2) there was a greater interest in frequency domain kernels because they are believed to have a more intuitive interpretation [Boyd et al, 1983].

In the present work, the choice to work in the time-domain has been made. Doing so allows for a degree of simplicity in the application of the basis function expansion technique to be described in the following sections. After the kernels have been identified and predictions have been made, the results will then be transformed into the frequency-domain for further analysis.

The Volterra kernel identification method used in this work is based on an existing identification technique, developed for the extraction of nonlinear indicial responses from experimental data. This approach relies on the expansion of kernels into a basis function space and the subsequent creation of a linear system of equations, for which the bounds are set by experimental input and output data. The uniqueness of this method is that, while the Volterra series is nonlinear with respect to the input parameter, the inverse problem of identifying the kernels remains linear with respect to the kernels.

5.3 Linear Kernel Expansion into Basis Function Space

In creating a basis function space for the expansion of Volterra kernels it is logical to choose a function form which is similar to the parameter being modeled. In the case of Volterra theory, the kernels represent multidimensional impulse responses of the system. Therefore the form of an impulse response, an exponential decay, is chosen as the basis function. As a means of illustration, the first term of a truncated Volterra series will be considered, as shown in Equation 5.1,

$$y(t) = \int_0^t h_1(\tau_1) x(t-\tau_1) d\tau_1$$

Equation 5.1

where x (t) is the system input parameter and y (t) is the system response parameter. Here, the linear kernel h_1 is expanded into basis function space,

$$h_1 = \sum_j c_j \xi_j(t)$$

Equation 5.2

where c_j is a set of unknown basis coefficients, the integer j defines the number of basis functions used, and

$$\xi_j = e^{-jt}$$

Equation 5.3

are the basis functions. In Equation 5.3, the integer j also serves as a series of time constants used in defining the decaying exponential basis functions. By substituting the expanded kernel form into Equation 5.1, the linear term of the series becomes

$$y(t) = \sum_j c_j \int_0^t \xi_j(\tau) x(t-\tau) d\tau .$$

Equation 5.4

In examining Equation 5.4, the basis coefficients, c_j, are the only unknown parameters. The convolution integral is comprised of the basis functions, ξ_j, which are known functions of time, and the measured input time-series, x (t). By simplifying Equation 5.4 to the form

$$y_i = \sum_j c_j a_{ij}$$

Equation 5.5

For the time step i = 0,…, t, where

$$a = \int_0^t \xi_j(\tau) x(t-\tau) d\tau$$

Equation 5.6

is defined as the motion matrix, it becomes evident that Equation 5.4 is linear, and solving for the basis coefficients is inherently an inverse problem. In this system of equations, multiple sets of input and response data are used as constraints representing the system's behavior. The unknown basis coefficients must satisfy these constraints at all points in time. Applying Equation 5.5 to multiple sets of data, the linear equation becomes

$$\sum_n A^{(n)} C = \sum_n Y^{(n)}$$

Equation 5.7

where Y is the response data matrix, A is the motion matrix, C is the solution matrix containing the unknown basis coefficients, and the variable n represents the number of data sets used in the solution. Generally, the resulting system of linear equations is ill-posed and a regularization technique must be applied when solving for the set of basis coefficients [Reisenthel, 1999].

5.4 Extraction of Linear Kernels From Data Sets

Because the linear system of equations representing the linear term of the Volterra series is ill-posed, performing a general matrix inversion of the motion matrix and then solving for the basis coefficients will not always guarantee a unique solution. A problem is deemed ill-posed if its solution is not unique or if it is not a continuous function of the data. The condition number of a matrix, which is defined as the ratio between the largest and smallest singular values of the matrix, implies the degree of a problem's ill-posedness [Hansen, 1998]. A large condition number of the motion matrix A implies that some of the equations of the linear system in Equation 5.7 are numerically independent.

Several steps are taken in the solution process to ensure that the set of basis coefficients solved for are indeed unique solutions. The first step is to perform a linear least squares fit on the data in order to minimize error. A linear least squares fit fits a line

to the data that minimizes the sum of the squared deviations of the data from the fitted line. This is accomplished by multiplying each side of Equation 5.7 by the transpose of the motion matrix A, which results in the equation

$$\sum_n A^{T(n)} A^{(n)} C = \sum_n A^{T(n)} Y^{(n)} .$$

Equation 5.8

Stated more simply,

$$MC = B$$

Equation 5.9

where M is the least squares motion matrix and B is the least squares response data matrix. Because this action is performed on both sides of the equation, the net effect of the operation leaves the equation unchanged. Equation 5.9 makes it apparent that the solution process remains linear with respect to the kernels.

The next step in assuring a unique solution of the set of basis coefficients is to solve for them using a Singular Value Decomposition (SVD), also called a pseudo-inverse. The SVD is said to be the superior tool for the analysis of discrete ill-posed problems [Hansen, 1998]. The SVD breaks down the ill-posed matrix into three separate matrices containing the singular values of the matrix, σ, and two sets of basis vectors, μ and υ. Through a SVD the ill-posed motion matrix is transformed into the form

$$M = \sum_{i=1}^{n} \mu_i \sigma_i \upsilon_i^T .$$

Equation 5.10

The set of basis coefficients C can then be solved for after manipulation of Equation 5.9 and Equation 5.10 as

$$C = \upsilon^{-1} \sigma \mu^T Y .$$

Equation 5.11

With the basis coefficients known, solving for the linear kernel is simply a matter of inserting the basis coefficients into the expanded form of the kernel given in Equation 5.2, and summing the terms together. The result is a time-series exponential decay representing the linear impulse response of the system.

5.5 Choosing the Appropriate Number of Basis Functions

Choosing the number of basis functions needed to properly identify the linear kernel h_1 is a matter of trial and error. Figure 5.1 shows a series of h_1 kernels extracted from the total pressure distortion data sets of interest with a varying number of basis functions. As seen in this figure, as the number of basis functions increases, the response begins to converge to the appropriate response. From Figure 5.1 it can be concluded that using eight or more basis functions produces no further change in the response function, and will provide a converged response for the current work. Ten basis functions have been used in the identification of the linear kernel throughout this investigation.

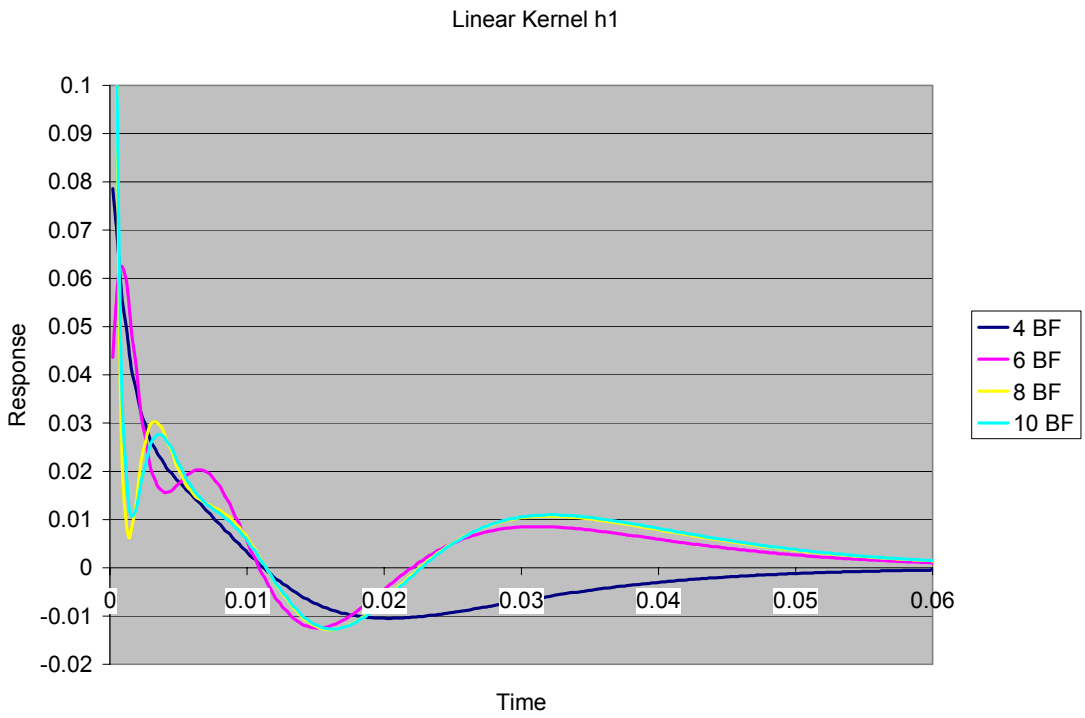

Figure 5.1. Comparison of number of basis functions used in the identification of the linear Volterra kernel from total pressure distortion data sets.

5.6 Relating the Kernel Identification Method to Higher-Order Kernels

In identifying higher-order Volterra kernels, the same principles used in the identification of the linear kernel apply. When solving for higher-order kernels, all kernels, including the linear kernel, are solved for simultaneously. This is what creates the distinction of the linear kernel h_1 from the basic FRF, as was discussed in Section 3.2. Just as the linear kernel is comprised of several basis function terms, the higher-order kernels consist of a series of terms. Consider h_2, a two-dimensional function of time. As stated in Section 3.2, h_2 is a function of both time and time lag, so that for every value of time lag used, a new function of time is defined. These sets of functions of time are referred to as *terms*. The first term of the kernel is defined when both unit impulses are applied at the same time. The second term of the kernel is then defined for the first value

of time lag selected, and so on [Silva, 1993]. The number of terms needed to accurately define a second-order kernel depends on the system at hand. Much like the number of basis functions used in defining the linear kernel, the higher-order kernels will begin to converge after a certain number of terms.

5.7 Identifying the Second-Order Kernel

When identifying the second-order kernel h_2, the kernel is expanded into a basis function space just as the linear kernel was in Equation 5.2. The main difference in this case is that, while h_1 is a one-dimensional kernel, h_2 exists in two dimensions. Because of this it is necessary to define a two-dimensional array of time constants when expanding the second-order kernel into basis function space. As discussed in Section 3.2, it is necessary to impose symmetry on the multi-dimensional kernels in order to ensure uniqueness. This is done through the choice of time constants used to define the kernel's basis function space. In the case of h_2, symmetry is imposed on the kernel by creating a two-dimensional, symmetric matrix of time constants. In order for a matrix to be symmetric, the matrix itself must be equal to its transpose. As an example, consider a three term, 2nd order kernel. Here, a 3 x 3 symmetric matrix of time constants is appropriate for kernel expansion, defined as tc,

$$tc = \begin{bmatrix} 1 & 2 & 3 \\ 2 & 3 & 1 \\ 3 & 1 & 2 \end{bmatrix}, \qquad tc^T = \begin{bmatrix} 1 & 2 & 3 \\ 2 & 3 & 1 \\ 3 & 1 & 2 \end{bmatrix}.$$

Equation 5.12

It is apparent that symmetry has been satisfied, as the transpose of tc is equal to tc itself. When the kernel is expanded into basis function space, the form of tc will impose the same form onto the kernel, that of a two-dimensional symmetric matrix. With the kernel expanded into two-dimensional basis function space, the procedure of extracting the basis

coefficients from the data sets follows the same procedure for the linear kernel, as laid out in Section 5.4.

Identification of the third-order kernel h_3 is identical to that of the second-order kernel, however the definition of time constants is extended to three dimensions.

The kernel extraction technique described here has been implemented in a Matlab® code that serves as both a kernel extraction and prediction tool. This code has been set up to operate as a 1st, 2nd, and 3rd order Volterra system. By specifying time-series data to be used for kernel extraction, and time-series input data to be used for prediction, the code extracts kernels based on a specified number of basis functions and kernel terms. The system created is then used to predict the system response, which is presented as time-series plots of measured and predicted waveforms.

6 Training Volterra Kernels

6.1 Training Volterra Kernels

One benefit of the kernel identification technique used in this study is that it is capable of including knowledge from several data sets in the solution. As mentioned in the previous chapter, these data sets create the bounds which the basis coefficients, and therefore the kernels themselves, must satisfy at all points in time. The idea of kernel training implies the imparting of knowledge of system behavior by means of extracting kernels from known input and response data sets. The behavior of the system in these data sets is said to train the kernels to the system's inherent response characteristics.

6.2 Choice of Training Data Sets

The distortion data available in this study consists of three separate mechanical speeds, each with four operating points and five distinct streamlines. Within these three speeds, two distortion types exist, 3 per rev and 8 per rev. With this limited set of data it is necessary to choose a set of training data that will allow for a full analysis of the prediction capabilities of the Volterra series. It is desired to be able to make downstream distortion pattern predictions based on novel data. Novel data implies the prediction of distortion patterns at speeds and operating points not actually used in the training of the kernels. Doing so will assess the Volterra series' ability to simulate the propagation through the rotor of unmeasured distortion patterns and of unknown operating conditions, as set out in the scope of this study.

In keeping with the above argument of making predictions of novel data, a schedule of upstream and downstream rotor distortion patterns has been selected for Volterra kernel training. The same training data set will be used for all predictions in order to create consistency amongst predictions. The data sets chosen for the training of kernels, as well as for making predictions, are laid out in Table 6.1.

Table 6.1 Data Sets Used for Training Kernels and Making Predictions

Kernel Training Data Sets	Prediction Data Sets
9100 PE RI1 – RI5	9100 NOL RI1 – RI5
9100 WOD RI1 – RI5	9500 PE RI1 – RI5
9500 NOL RI1 – RI5	13200 WOD RI1 – RI5
9500 NS RI1 – RI5	

In all, twenty data sets have been chosen for use in the training of the Volterra kernels. When examining the choice of data sets shown in Table 6.1, it is evident that none of the prediction data sets are included in the kernel training. This ensures that novel data sets are being predicted to assess the true merit of the Volterra series model. With this choice of data sets, predictions will be made at new operating points on speed lines used in training, as well as on a new speed line not used in kernel training, 13200 rpm. Note that all five radial immersions of each data set have been included in the training data while predictions will be made at individual radial immersions. This has been done in order to include as much system information as possible in the training of the Volterra kernels. The consequences of doing so will be discussed in Chapter 8.

7 Results and Analysis of Downstream Distortion Pattern Predictions Using the Nonlinear Volterra Series

7.1 Presentation of Results

In the presentation of Volterra series downstream distortion pattern predictions, several areas will be considered and analyzed. The first form of results presented will be that of a time-series comparison of predictions and measured data. This will provide qualitative insight into the physical forms of the predictions and how well they recreate the measured distortion waveforms. Next, a quantitative comparison will be made of the frequency content of predictions and measured data. This analysis of results is of particular interest when considering the motivation for this study, the prediction of frequency content of downstream total pressure distortions, as related to HCF drivers.

In order to carry out an analysis of frequency content, all time-domain Volterra predictions are transformed into the frequency-domain by means of a 360-point Discrete Fourier Transform normalized by the number of data points. The actual frequency content to be considered are the magnitude and phase components of each prediction. Each of these components is calculated from the real and imaginary values resulting from the Discrete Fourier Transform. The magnitude component is computed as

$$Mag = \sqrt{\mathrm{Re}\,al^2 + \mathrm{Im}\,ag^2}\ .$$

Equation 7.1

The phase component, presented in units of radians, is computed as

$$Phase = \tan^{-1}\left(\frac{\mathrm{Im}\,ag}{\mathrm{Re}\,al}\right).$$

Equation 7.2

In the analysis of frequency content, only the first 24 harmonics will be considered. All higher harmonics in the downstream distortion patterns are seen to tend very nearly toward zero, and therefore can be considered to have a negligible impact on the overall response. Focusing on the first 24 harmonics will allow for greater detail in the inspection of distortion magnitude and phase. An example of a complete frequency spectrum is shown in Figure 7.1. Here, the frequency content of the measured downstream distortion pattern at 9500 PE RI5 R1 is presented. A total of 360 spectral lines are shown. This is an extended presentation, including spectral lines through twice the nyquist frequency, which is equal to one half of the sample frequency (180 spectral lines.) The second half of the frequency spectrum, from the nyquist frequency up, is an exact mirror image of the content of the first half. It is apparent here that frequency magnitudes become negligibly low before the 30th harmonic, and remain so until the 335th harmonic, where the first 24 harmonics are mirrored.

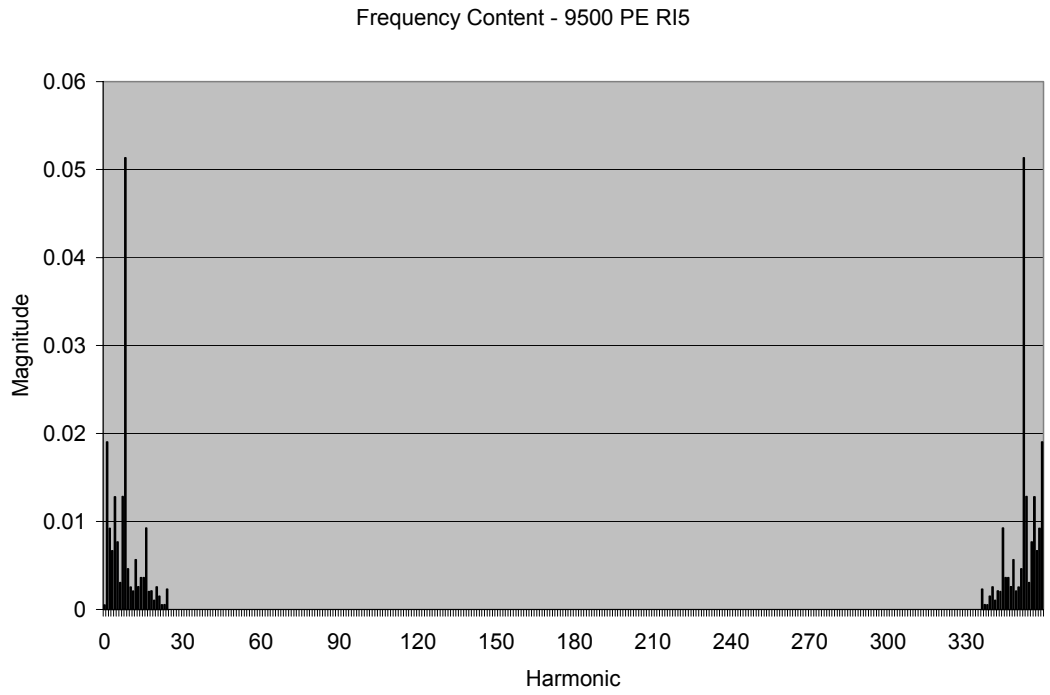

Figure 7.1. An extended presentation of the frequency spectrum of the measured downstream distortion pattern at 9500 PE RI5 R1.

A method of comparing the ability of predictors to capture frequency content magnitudes of a measured distortion pattern has been adopted in this study. The accuracy of a prediction, as related to frequency content, is defined as

$$Acc = \frac{MeasuredMagnitude}{\Pr edictedMagnitude}$$

Equation 7.3

where a perfect prediction would yield a value of 1.0. This definition of accuracy is applied in two separate manners. The first method is to calculate an average accuracy over the span of 24 harmonics of a prediction. The second method is to compare the accuracy of the prediction at the dominant frequency of the distortion pattern. Using these two evaluation methods will provide quantitative comparisons of how well a predictor has recreated the frequency content of a distortion pattern. This will allow for comparisons between the capabilities of the Volterra series and other prediction methods, namely the tuned FRF method of Small (2001). Note that this definition of accuracy provides an analysis of a prediction's frequency magnitude, but does not include phase information.

A definition of terms is in order before presenting prediction results. When referring to measured data, the term "Meas" will be used in plot legends. When referring to a Volterra series prediction, the suffix "Volt" will be used followed by a series of numbers representing the order of the prediction (1^{st}, 2^{nd} or 3^{rd}) and the number of terms used in the highest order term of the series. For example, when presenting a 2^{nd} order Volterra series prediction consisting of ten 2^{nd} order terms, the nomenclature "Volt 210" will be used. Likewise, for a 3^{rd} order Volterra series prediction consisting of three 3^{rd} order terms, the nomenclature "Volt 33" will be used.

7.2 Assessing the Capabilities of the Volterra Series in Predicting Downstream Distortion Patterns

There are several levels of assessment to be conducted in determining the capabilities of the Volterra series. The first area investigates the ability of the Volterra series to recreate data that has been used to train its kernels. The next area of assessment lies in the ability of the Volterra series to predict novel downstream distortion patterns. The choice of training and prediction data sets has been discussed in detail in Section 6.2. Here the levels of prediction, namely 1st, 2nd, and 3rd order, will be individually analyzed in order to show the enhancement of predictions as higher-order terms are added to the series. In addition, an illustration of the superposition of terms in creating an overall prediction will be provided. Initial results will be based on first stage distortion behavior. Results of a Volterra series based on second stage distortion behavior will be investigated in Chapter 11. Finally, the ability of the Volterra series model to predict distortion patterns propagating through a separate rotor of different design will be also be investigated in Chapter 11. This analysis will provide insight into the ability of the Volterra series to capture the fundamental properties of compressor behavior.

Before investigating the abilities of the Volterra series in predicting distortion propagation, it is beneficial to test its abilities on more simple waveforms, i.e. sine waves. This will serve as a proof of concept and highlight the capabilities and limitations of the model. Using a basic sine wave constructed from 360 points as an input to a system and treating the output with a known operator will make any underlying error in the model made known.

An initial test of the model is conducted by training the kernels of a Volterra series with an input sine wave and an output waveform of known behavior. Two tests are conducted. First the output will be treated in a linear manner by amplifying and shifting the input sine wave. Next, as a separate test, the output will be treated in a nonlinear, 2nd order manner by squaring the input sine wave. The kernels of the Volterra series in each test will be trained using the same data sets as those that will be predicted.

In the case of the linear test, the kernels are trained with the input sine wave and the output amplified and shifted sine wave as shown in Figure 7.2 and Figure 7.3. After creating the Volterra series the input sine wave is then used as an input to re-predict the amplified and shifted sine wave. The time series results of the prediction are shown in Figure 7.4. As seen in this figure, the predicted waveform exactly overlays the actual waveform. As a further analysis, the frequency content of the prediction is now compared with that of the actual waveform.

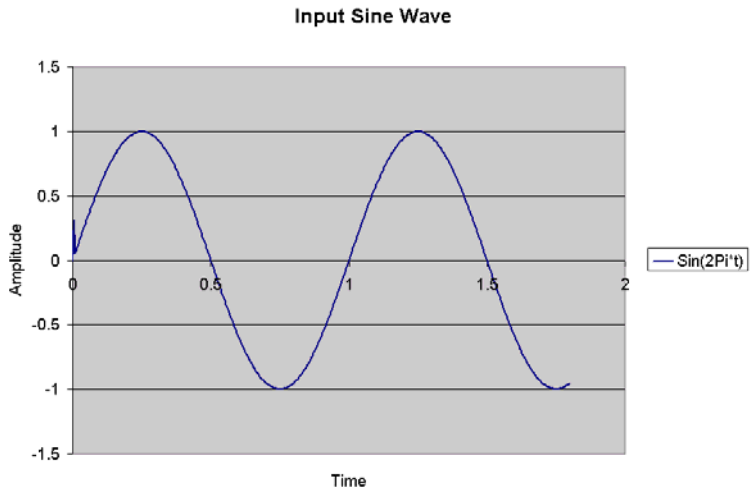

Figure 7.2. Input sine waveform.

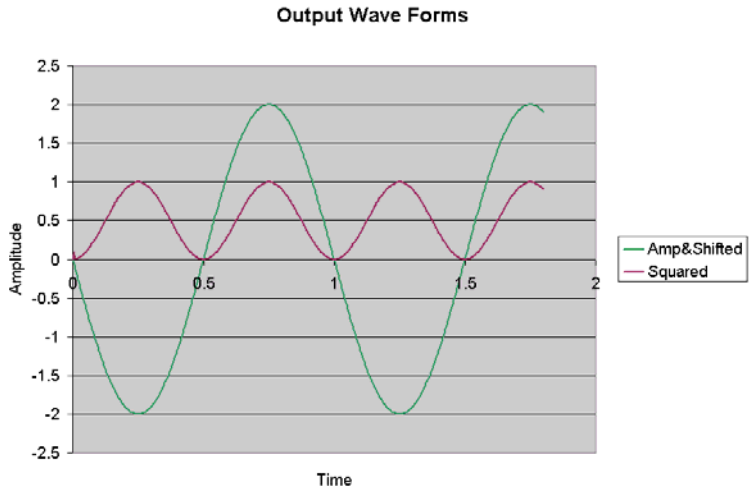

Figure 7.3. Linear and 2nd order output sine waveforms.

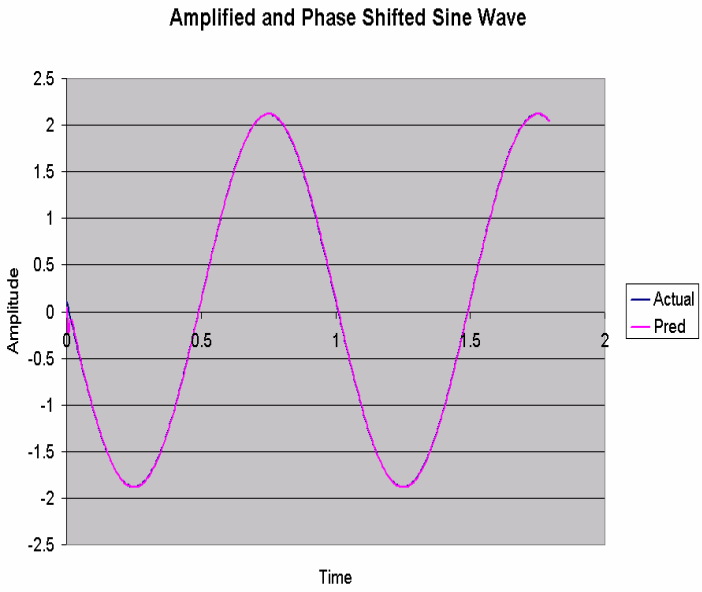

Figure 7.4. Volterra prediction of amplified and shifted sine wave.

Figure 7.5 shows the magnitude and phase of both the predicted amplified and shifted waveform and the actual waveform. It is seen that the magnitude and phase of the prediction matches the actual with very good accuracy. Of particular interest is the magnitude at the dominant frequency, the 2nd harmonic, where very good agreement is again found between actual and predicted waveforms.

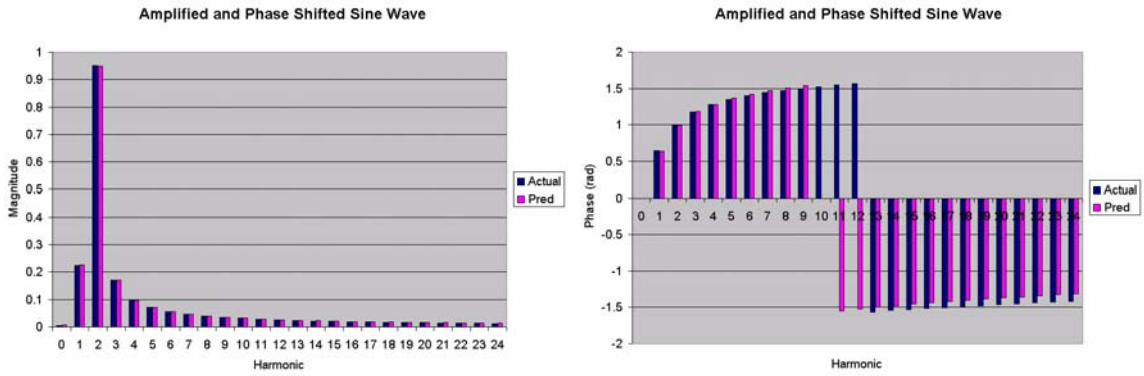

Figure 7.5. Frequency content of Volterra prediction of amplified and shifted sine wave.

In a similar manner, a nonlinear test of the Volterra series is performed as well. In this case, the output waveform is a squared sine wave, representing a 2nd order operation. Here, one would expect good agreement between a 2nd order Volterra prediction and the

actual waveform. The time series results of the prediction are compared with the actual waveform in Figure 7.6. Here, Volterra series consisting of five 2nd order kernels terms and ten 2nd order kernel terms are considered. It is seen that the Volterra series with only five 2nd order terms has not done well at recreating the waveform. However, with ten terms the prediction is seen to converge towards the actual waveform. This is a good illustration of the necessity of including a sufficient number of terms in higher order kernels to exactly capture higher order effects. The frequency content of the predictions is provided in Figure 7.7 as well. Here it is seen that the dominant frequency magnitude of the prediction more closely matches that of the actual waveform when ten terms are included in the 2nd order Volterra kernel. Also, the prediction with five terms is 180° out of phase over more than half of the frequency spectrum presented, however this is corrected with the addition of five more terms to the kernel..

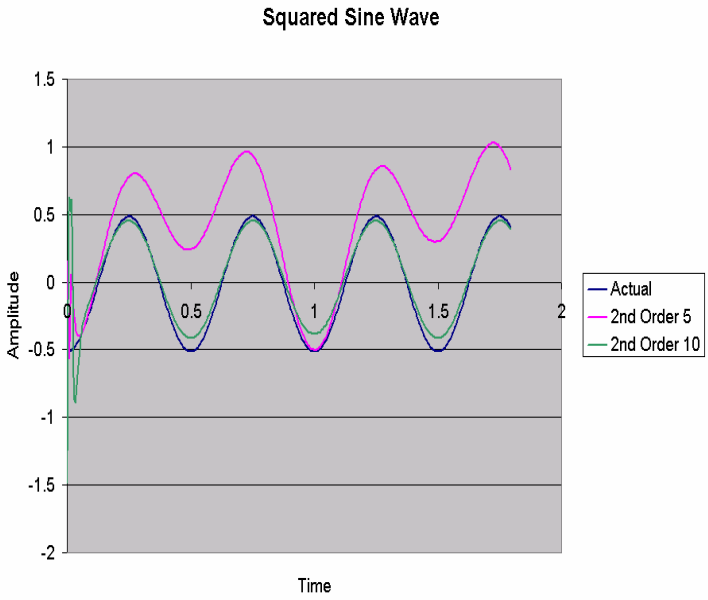

Figure 7.6. Volterra predictions of a squared sine wave.

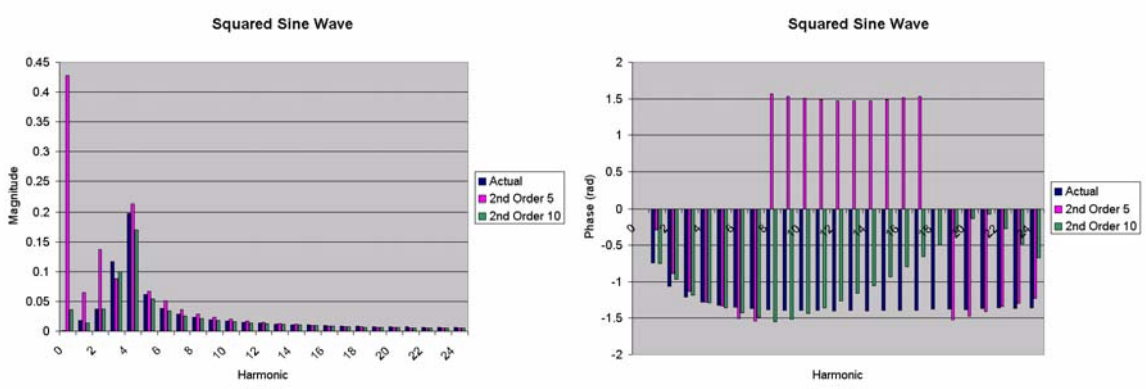

Figure 7.7. Frequency content of Volterra predictions of a squared sine wave.

The results of this initial test of the Volterra model have demonstrated the capabilities and limitations of the model. It has been shown that a sufficient number of terms in higher-order kernels is needed to fully capture a higher-order effect. Because of the limitation of data resolution on solving for basis coefficients in the kernel expansion procedure discussed earlier, it is not possible to extend the Volterra series with extra terms in the higher-order kernels. Because of this, a baseline error has been established which can be expected in predictions of distortion propagation as well.

7.3 Recreating Downstream Distortion Patterns of Data Used to Train Volterra Kernels

The first test of a Volterra series is to ensure that it is capable of recreating downstream distortion patterns of operating conditions that have been included in the training of its kernels. While this assessment may seem trivial, it is a necessary test of the system. The possibility exists that the results of kernel extraction are merely fitting the data sets used. Because of this, steps must be taken to ensure that the kernels have captured the true physics of the system's response behavior. The first step is to ensure that the kernels all individually converge to a set response as the number of terms in the kernels and basis functions used in extraction are increased. The satisfaction of this criterion has already been discussed in Section 5.5 and Section 5.6. The next step, which

is discussed in the current section, is to ensure that data used for identification of the kernels can be recreated by the extracted kernels.

Training the kernels of a third-order series with a single data set, and then making a prediction of this same data set carries out the test of the Volterra series' ability to recreate data used in kernel training. Two examples will be provided. The first set of data to be examined is 9100 PE RI3 R1. The upstream and downstream distortion patterns of this operating point are used to train the kernels of the Volterra series, with the same upstream distortion pattern subsequently used as the input to the series to recreate the downstream distortion pattern. A time-series comparison of the measured and predicted downstream distortion patterns is shown in Figure 7.8. Comparisons of the frequency content, magnitude and phase, of the measured and predicted downstream distortion patterns are shown in Figure 7.9 and Figure 7.10.

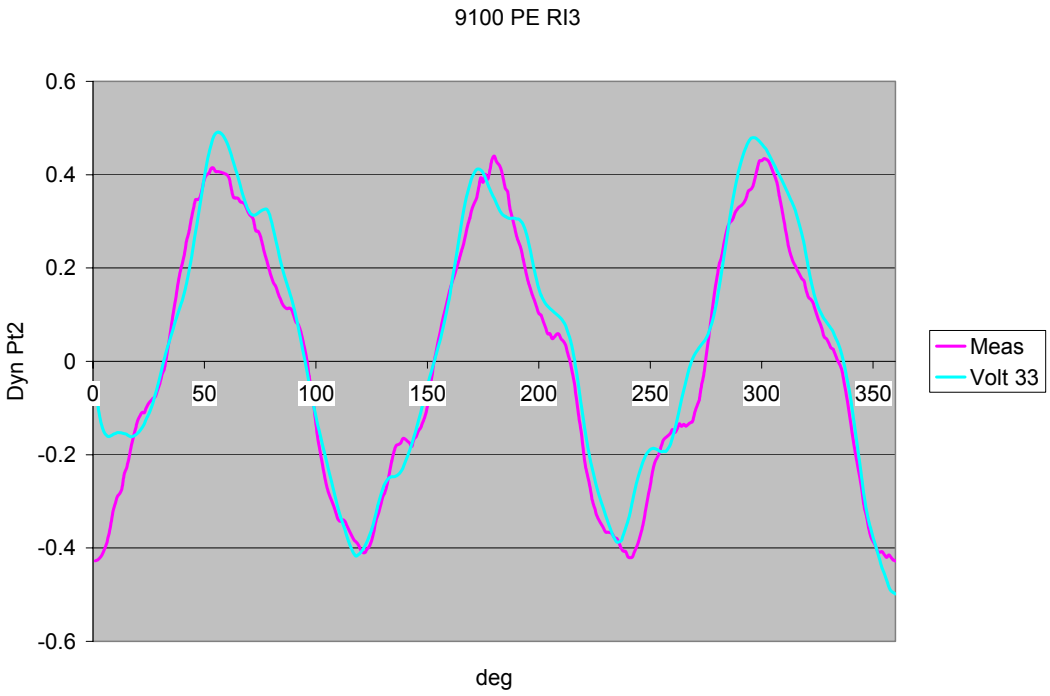

Figure 7.8. A time-series comparison of Volterra prediction of kernel training data – 9100 NOL RI3 R1.

Visual inspection of Figure 7.8 reveals the recreation of the time-series distortion pattern to be very good, confirming the ability of the Volterra series to match the general

distortion trend. Examining the frequency content of both the measured and predicted distortion patterns reinforces this confirmation. As seen in Figure 7.9, the prediction has come very close to matching the magnitudes of the distortion pattern, particularly at the distortion's dominant frequency, the third harmonic.

When examining the phase content of the measured and predicted waveforms, the results are not in as good agreement as would be expected. Predicted phase at the dominant distortion frequency and lower harmonics tends to be slightly ahead of measured phase, while at the higher harmonics the prediction is often 180° out of phase. When examining these results, keep in mind that this is a third-order system approximation, with all higher-order effects negated. As will be shown later in this chapter, comparisons between 2nd and 3rd order predictions often reveal shifts in phase. These observations serve as evidence that there may be higher-order influences in this system, which have not been included in current study.

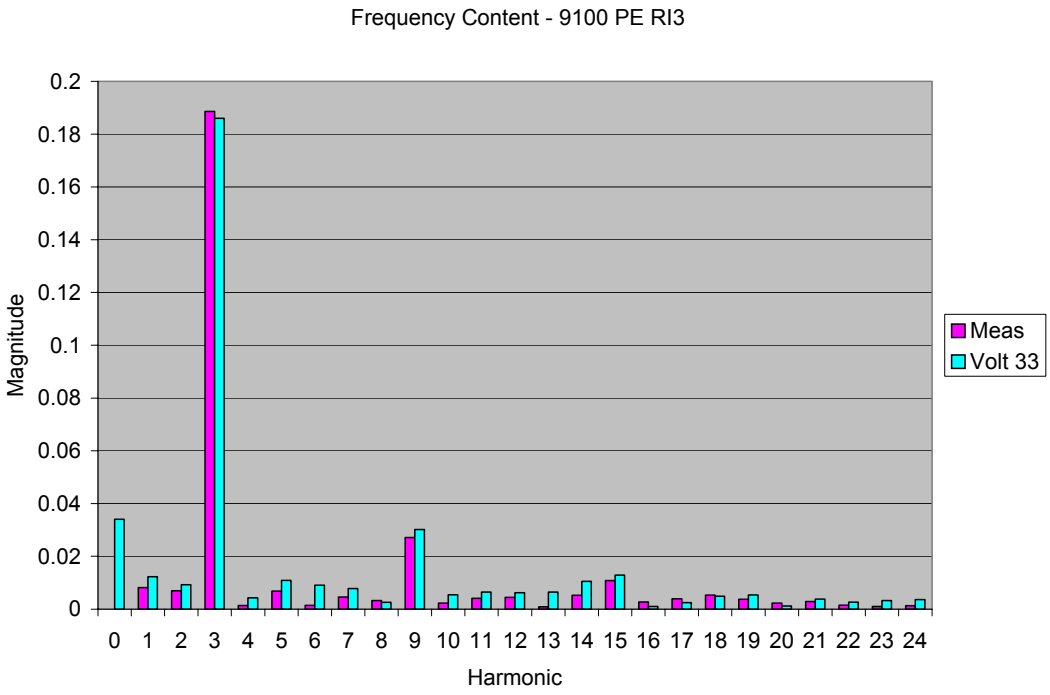

Figure 7.9. Frequency content of Volterra prediction of kernel training data – 9100 NOL RI3 R1.

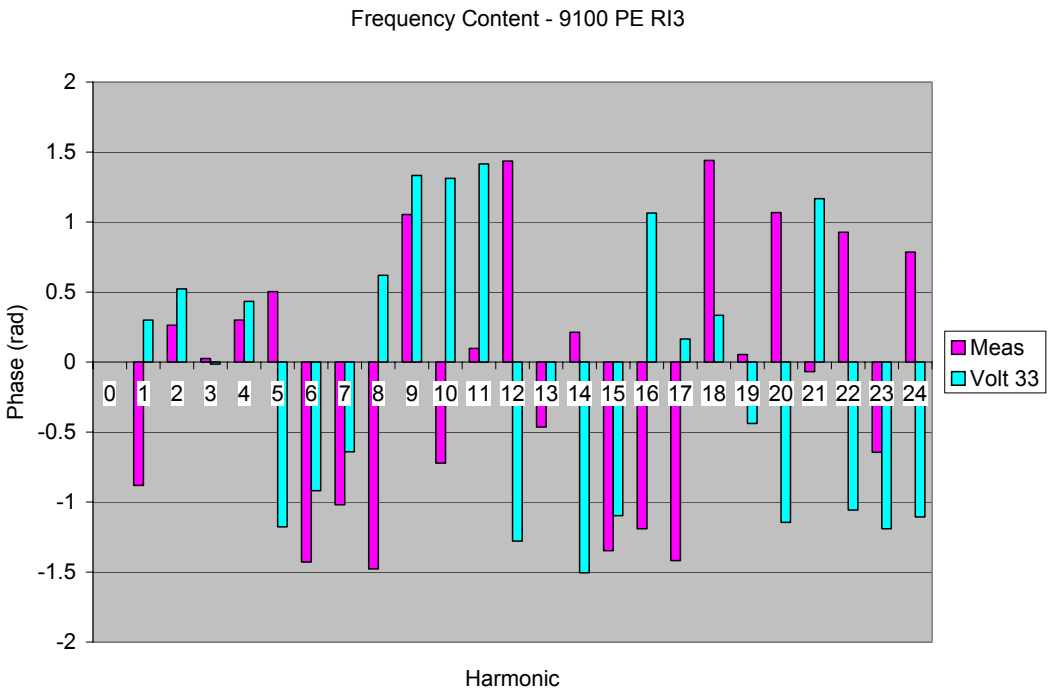

Figure 7.10. Frequency content of Volterra prediction of kernel training data – 9100 NOL RI3 R1.

The next data set used to test the Volterra series' ability to recreate data used in kernel training is 9500 NOL RI3 R1. Again, time-series and frequency content comparisons of the measured and predicted distortion patterns will be reviewed. In Figure 7.11, excellent agreement between the measured and predicted 8 per rev total pressure distortion time-series can be seen. And again, in Figure 7.12 the Volterra series has done well in capturing the distortion pattern's frequency magnitude content, particularly at the dominant distortion frequency. However, as seen at 9100 PE the phase content of the prediction in Figure 7.13 is not in exact agreement with the measured phase. In this example, phase at the dominant distortion frequency is very close to the measured phase. However, at several harmonics the prediction is either slightly ahead or 180° out of phase. Again one can hypothesize that these errors may be a function of higher-order influences neglected in the system model.

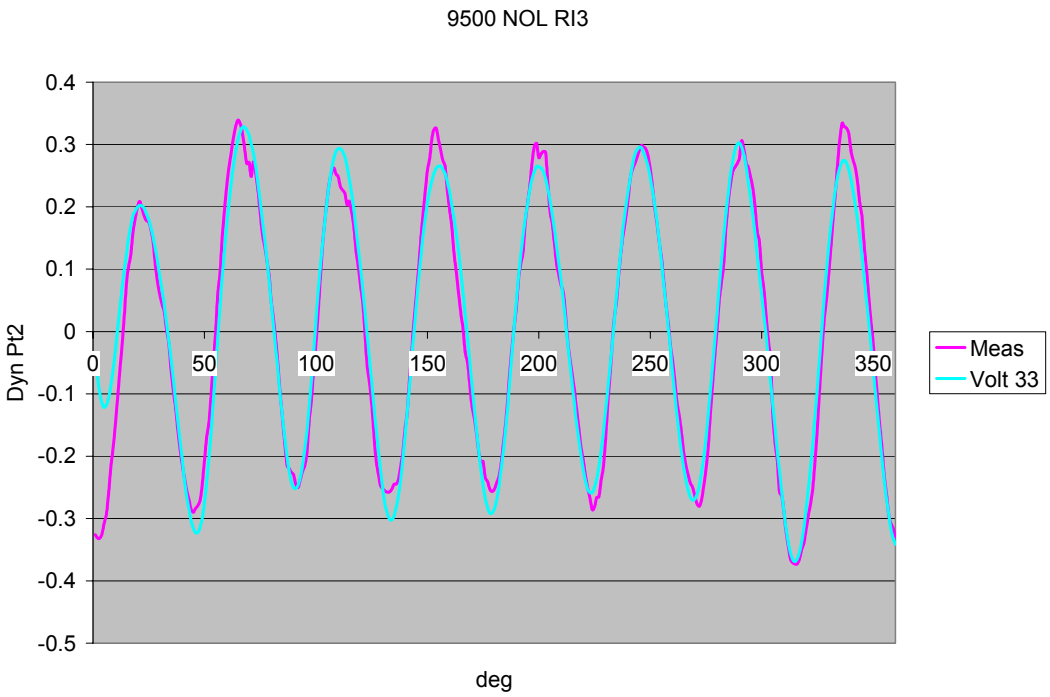

Figure 7.11. A time-series comparison of Volterra prediction of kernel training data – 9500 PE RI3 R1.

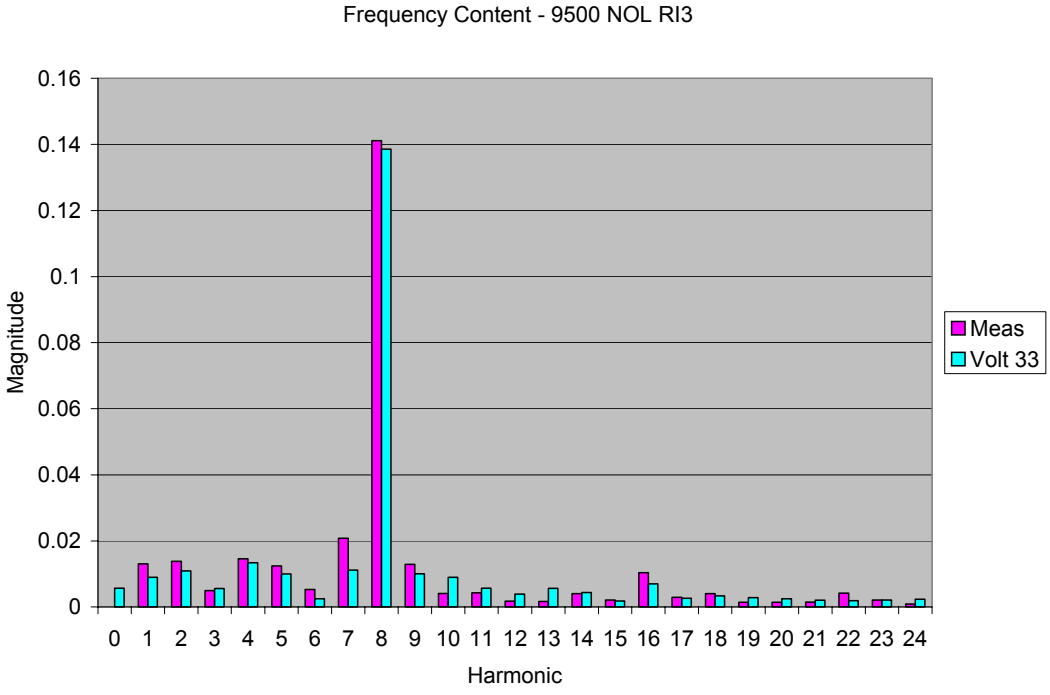

Figure 7.12. Frequency content of Volterra prediction of kernel training data – 9500 PE RI3 R1.

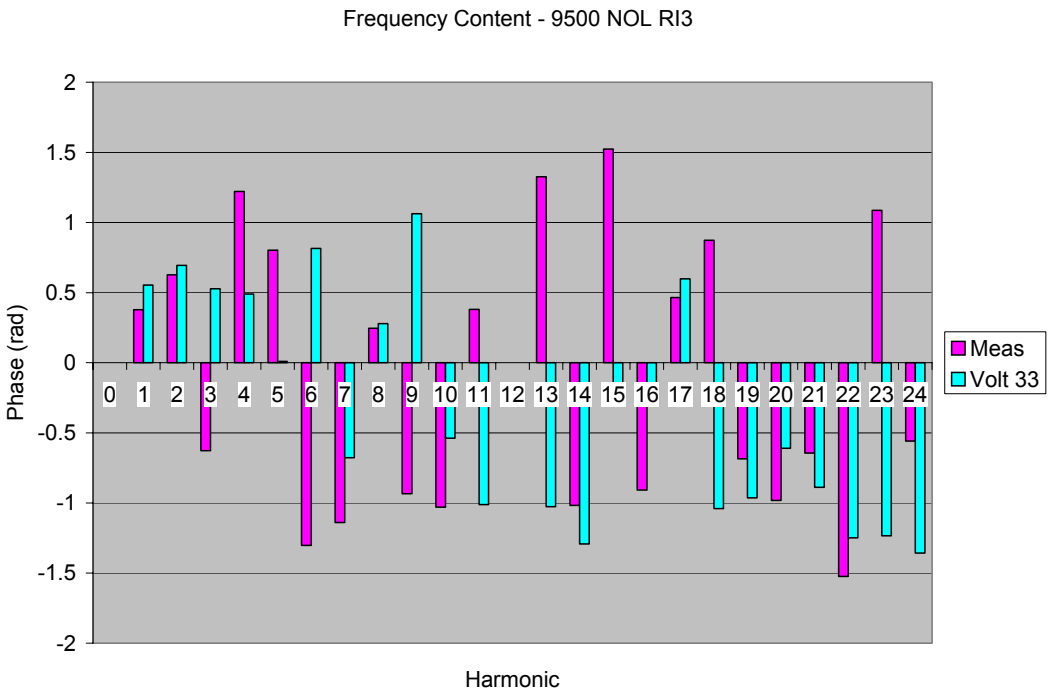

Figure 7.13. Frequency content of Volterra prediction of kernel training data – 9500 PE RI3 R1.

From these two examples, a conclusion can be drawn that the Volterra series is indeed capable of recreating distortion patterns used in the training of its kernels. Time-series and frequency magnitude reproductions have been shown to be very accurate. However, phase reproductions present a certain degree of error. This reproduction error provides a base line error in this method of system modeling, which one should expect to find as a component of prediction error as well.

A point of interest worth noting on the frequency magnitude presentations in Figure 7.9 and Figure 7.12 is the existence of a zero harmonic, or DC term, in the Volterra predictions. This is a common occurrence seen in nearly all Volterra predictions made in this study. Recall that all measured data is presented with the average total pressure (DC component) removed. Measured waveforms therefore contain no zero harmonic magnitude. However, the Volterra series predictions do contain a DC term. The existence of this term signifies a source of error in the prediction. The immediate conclusion drawn from the existence of the DC term is that the predicted dynamic time-series is offset from zero total pressure. The effect of this term on dynamic total pressure

distortion as an HCF driver, however, is negligible. Because the DC term has zero frequency, it does not have an impact as a driving frequency.

Also notice in the time-series comparisons shown in Figure 7.8 and Figure 7.11 that the beginning and ending points of the Volterra predictions are not coincident. This is not an expected result, as the 0° and 360° points are in fact the same circumferential position. These points do not coincide in the prediction as a result of the convolution integrals within the Volterra series. In convolution multiplication, the impulse response is not fully immersed in several of the first and last points of the input signal [Smith, 1997]. In other words, these first and last points of the signal are based on less information than the remaining points of the signal, and are therefore less reliable than the remaining points.

7.4 Results of Volterra Series Predictions of Novel Data

Predictions of novel data have been made with 1st, 2nd and 3rd order Volterra series. Doing so illustrates the improvement of predictions, as higher-order terms are included in the series, and imparts a better understanding of the fundamental concept of the Volterra series. Predictions of 13200 WOD at radial streamlines RI1 – RI5 R1 will be given as an example. Initially 1st order, linear predictions will be considered. Shown in Figure 7.14 are 1st order, linear Volterra predictions of 13200 WOD RI1 - RI5 R1. Note that the plots shown here are the actual output produced by the Volterra Extraction and Prediction Code, and present the dynamic downstream total pressure (Dyn Pt2) vs. circumferential degree (deg).

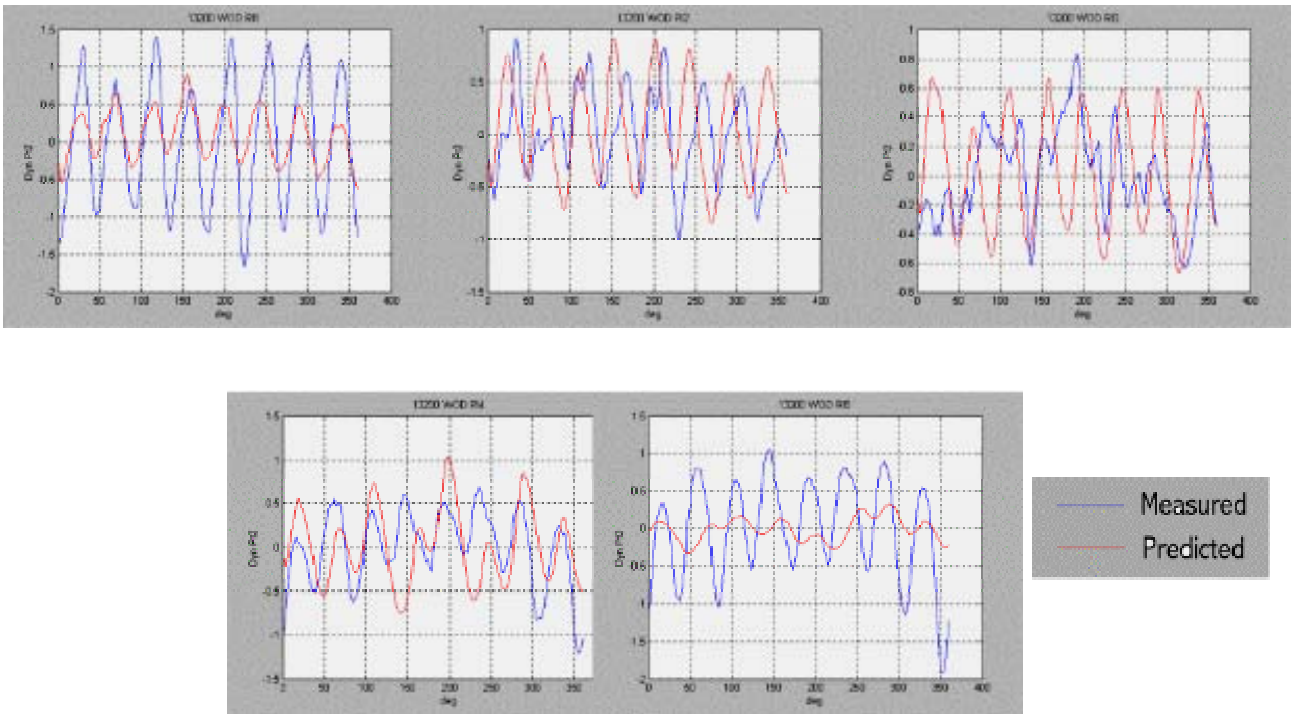

Figure 7.14. 1st order Volterra time-series prediction of 13200 WOD RI1-RI5 R1.

As noted in Section 6.2, this particular data set represents a new speed not included in the training of the Volterra kernels. From these predictions it is evident that the 1st order term of the Volterra series makes a prediction of the average waveform of the response. The linear term has recreated the 8 per rev distortion pattern and matched the circumferential placement of the peak distortions. However, the detail of the distortion peaks is not yet visible. Also note the lack of response at the near hub, RI5, prediction. This will be seen to be a typical characteristic of the Volterra series predictions and will be discussed further in Chapter 8.

Next the 2nd order Volterra predictions of 13200 WOD RI1 – RI5 are presented. Shown in Figure **7.15** are the time-series predictions made at this condition. Here, the 2nd order term has been added to the extraction and prediction process. While the 1st order term acts as the mean waveform of the response, the 2nd order term creates a higher-order, nonlinear variation around this mean. Looking at Figure **7.15**, it is apparent that portions of the detail of the downstream distortion pattern are beginning to take form in the predictions. This is particularly apparent in the prediction of RI2. Here, the dips in

peak distortions are beginning to take shape in the prediction. The variations in peak distortions at this radial immersion make this an excellent distortion pattern to use for illustration of the superposition of terms in a Volterra series.

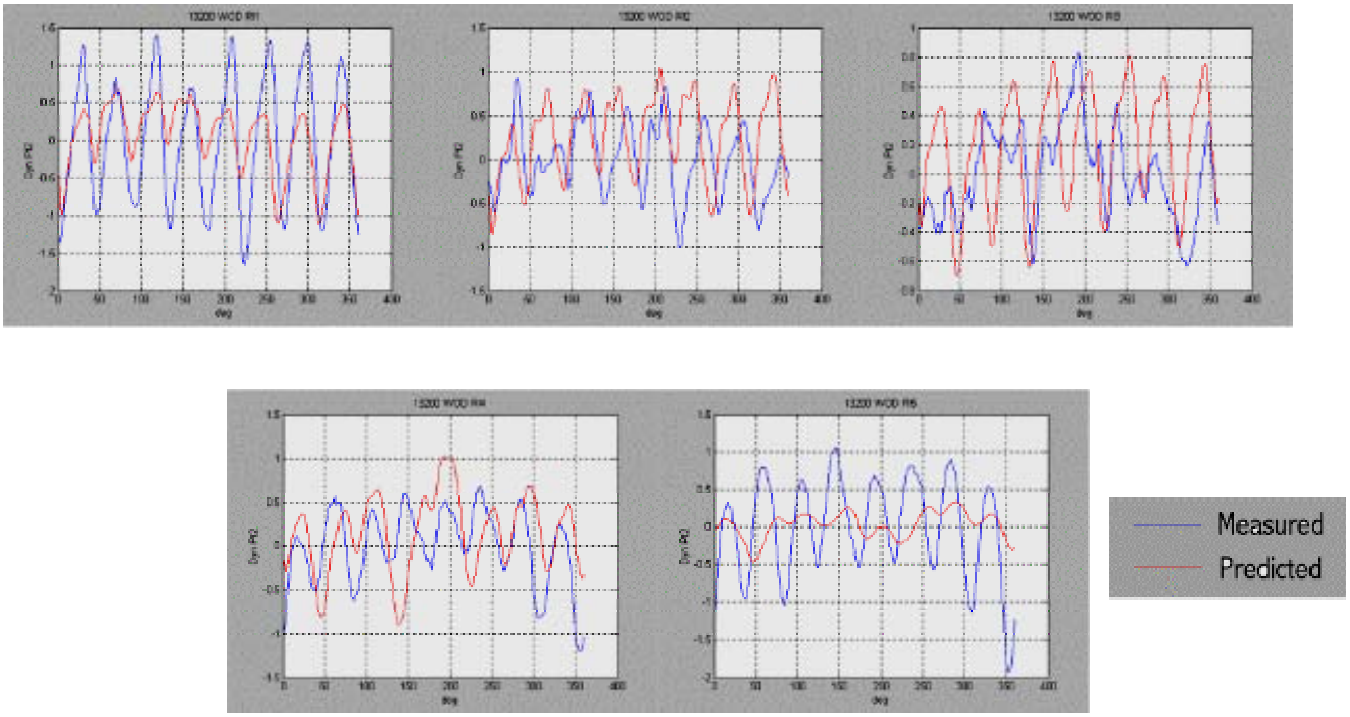

Figure 7.15. 2nd order Volterra time-series prediction of 13200 WOD RI1-RI5 R1.

The terms of a higher-order Volterra series add together by superposition to form an overall prediction. An example of this will be presented, illustrating how the addition of 1st and 2nd order terms of a 2nd order Volterra prediction of 13200 WOD RI2 R1 add together to create the downstream distortion pattern. Figure **7.16** shows the measured distortion pattern at this radial immersion, along with the 1st and 2nd order terms of a Volterra prediction plotted individually. Again, it is seen that the 1st order term creates an average waveform about the system response. Notice the third peak of the measured distortion pattern and its high frequency variation near 110°. This peak contains a dip, in essence creating two separate maximums. While the 1st order Volterra term only contains a single peak, it can be seen where the 2nd order Volterra term becomes negative and then positive in this area. Picture these two terms adding together, with the negative portion

of the 2nd order term initially lowering the value of the 1st order term, and then increasing it when the 2nd order term takes on a larger positive value. This action of superposition creates the dip in the distortion peak that is characteristic of the measured distortion pattern. Each individual Volterra term, along with the final 2nd order Volterra prediction and measured data are shown in Figure **7.17**.

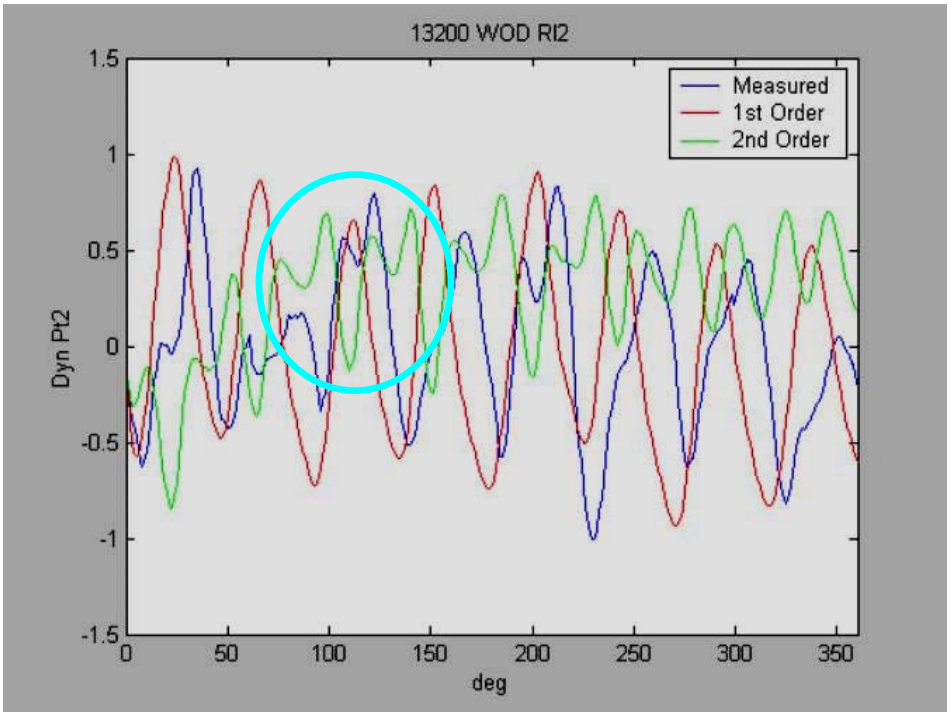

Figure 7.16. Illustration of superposition of terms in a Volterra series prediction. Measured response and terms of a 2nd order Volterra prediction of 13200 WOD RI2 R1 are shown.

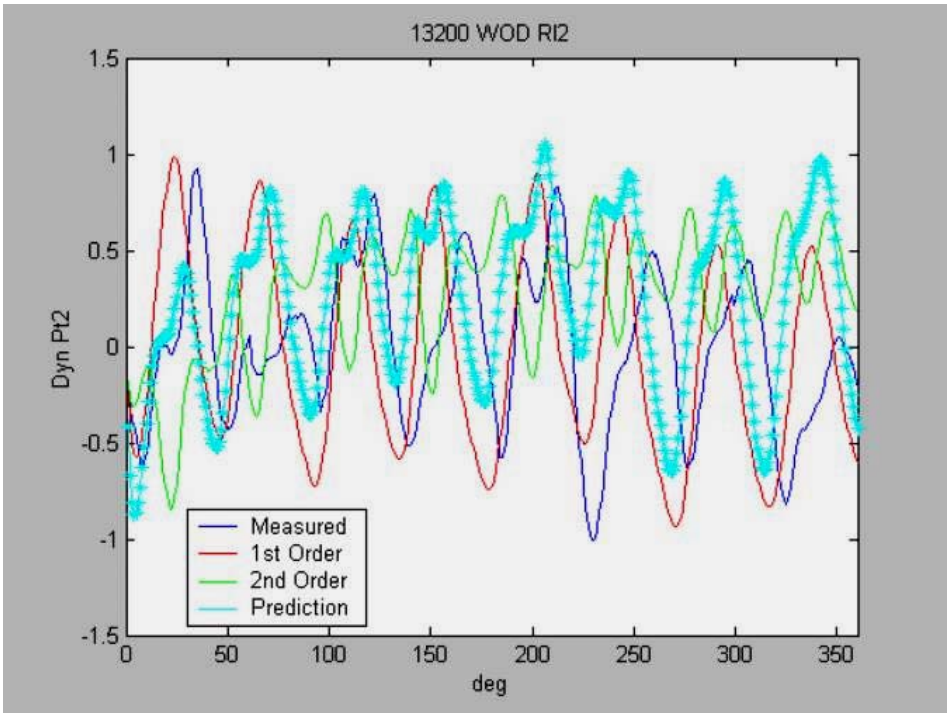

Figure 7.17. Illustration of superposition of terms in a Volterra series prediction. Measured response and prediction of 13200 WOD RI2 R1 are shown.

The third order Volterra predictions of 13200 WOD RI1 – RI5 R1 will now be presented. Shown in Figure 7.18 are time-series comparisons of third order predictions. Looking at the prediction of RI2, it is apparent that the 3rd order term has lowered the placement of the distortion peaks, bringing the prediction closer to the measured distortion pattern. The effect of the 3rd order term is also apparent in the prediction of RI4 where the distortion peaks have shifted in time closer to the measured peaks. Notice again that the higher-order terms have had little, if any impact on the near hub (RI5) prediction. Here, an 8 per rev response is apparent, however the distortion magnitudes are drastically under-predicted.

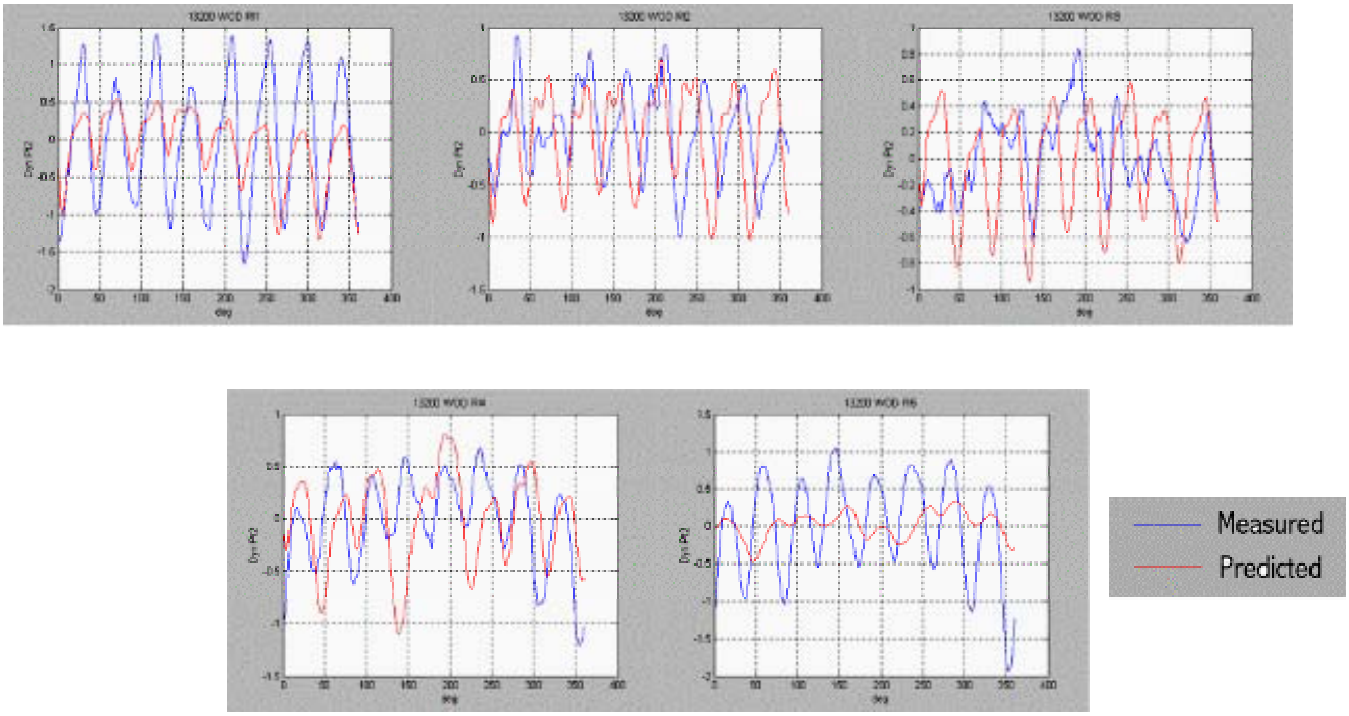

Figure 7.18. 3rd order time-series predictions of 13200 WOD RI1-RI5 R1.

7.5 Comparing Volterra Series Predictions to Tuned FRF Predictions

Results of 3rd order Volterra series predictions of 1st stage downstream total pressure distortions will now be compared to Small's tuned FRF predictions of the same conditions [Small, 2001]. First, time-series comparisons will be provided to enable a qualitative comparison of each predictor's ability to recreate distortion waveforms. This will then be followed by a quantitative comparison of frequency content over several radial immersions of each condition. Prediction accuracy will also be addressed. Note that tuned FRF predictions will be referred to as "FRF" in the presentation of results.

7.5.1 Comparison of 9100 NOL Predictions

The first predictions to be considered are of 9100 NOL RI1-RI5 R1. Recall this is a speed used in kernel training, however predictions are made at a new operating condition.

Time-series comparisons of predicted waveforms and measured data are shown in Figure 7.19. Both 2nd and 3rd order Volterra predictions have been included here to illustrate the influence, or lack there of, of the 3rd order term in these predictions. Notice at this condition that both Volterra predictions nearly overlay one another. This leads to the conclusion that at 9100 rpm, propagation of total pressure distortions through the rotor has little 3rd order influence. Figure 7.19 shows that the Volterra and tuned FRF predictions have both succeeded in capturing the characteristic 3 per rev waveform, and have closely matched the measured distortions at the near tip radial immersions. However, the tuned FRF has significantly over-predicted the response at near hub conditions. The Volterra predictions can be seen to closely match measured distortions over the entire span of the rotor.

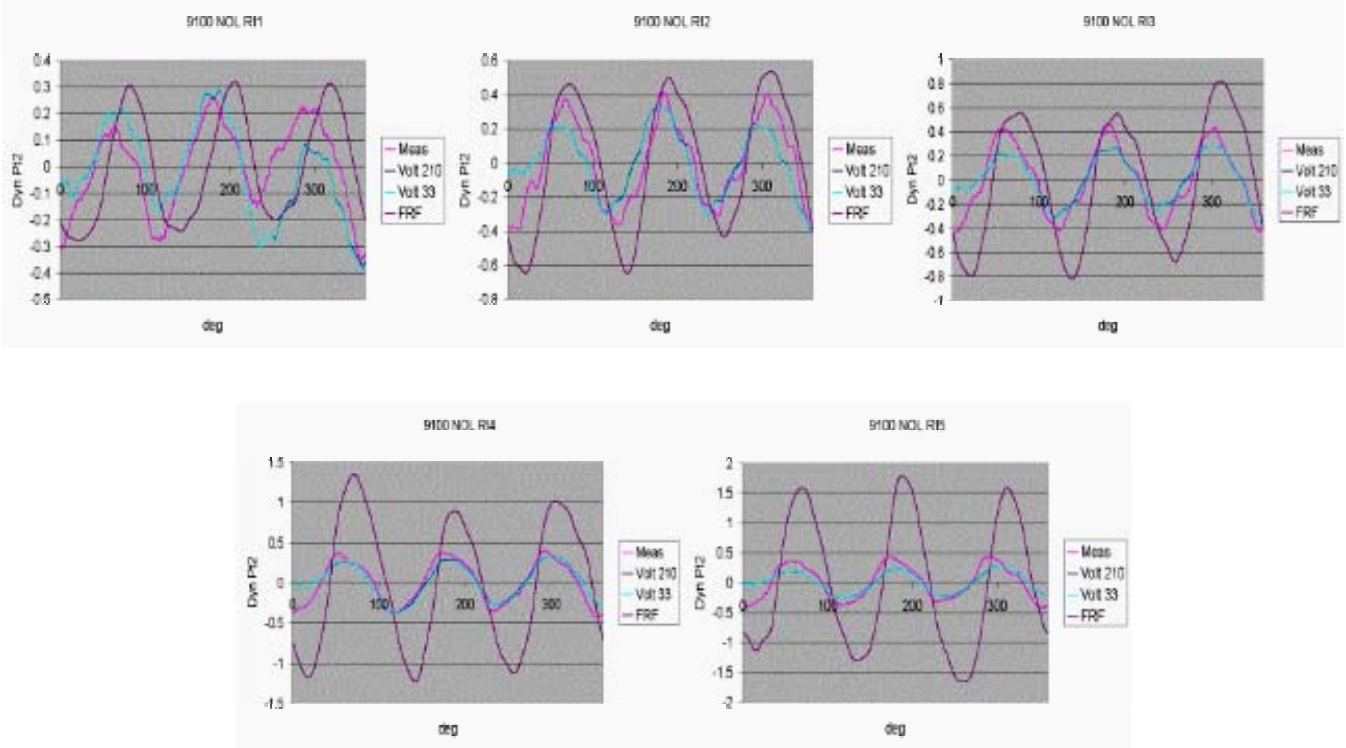

Figure 7.19. Time-series Volterra and tuned FRF predictions of 9100 NOL RI1-RI5 R1.

Figure 7.20, Figure 7.21, and Figure 7.22 present the frequency content of predictions at RI1, RI3, and RI5, respectively, with plots of frequency magnitude and phase vs. harmonic. The figures serve as reiteration of the results seen in the time-series

comparisons shown in Figure 7.19. Data at 9100 rpm represent a 3 per rev distortion, and as such the 3rd harmonic is the dominant distortion frequency. As seen in Figure 7.20, Volterra predictions have nearly matched the frequency content at the near tip (RI1) condition, and have come within 40% of dominant frequency magnitudes over the remaining radial immersions. Volterra predictions have accurate magnitudes at the higher dominant harmonics (6,9,12, etc.) as well. Phase plots show that all predictions, however, show poor agreement in phase.

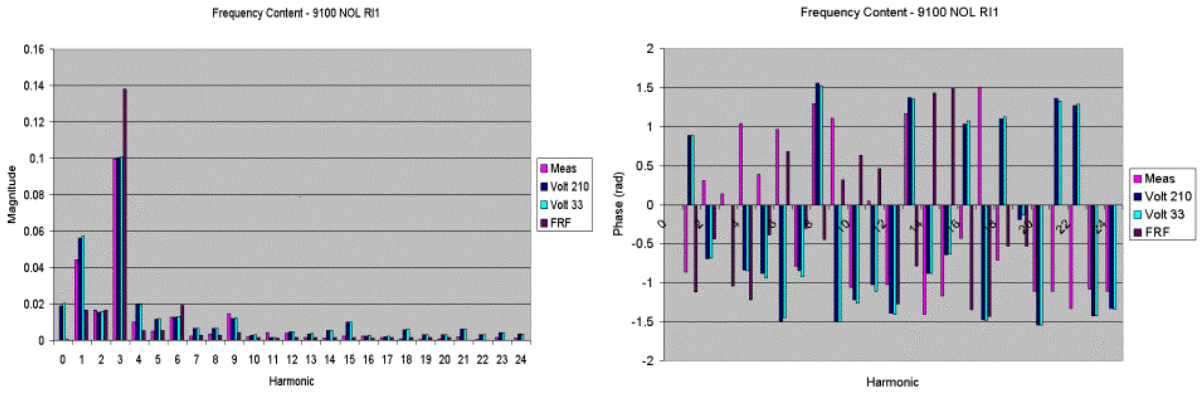

Figure 7.20. Frequency content of Volterra and tuned FRF predictions of 9100 NOL RI1 R1.

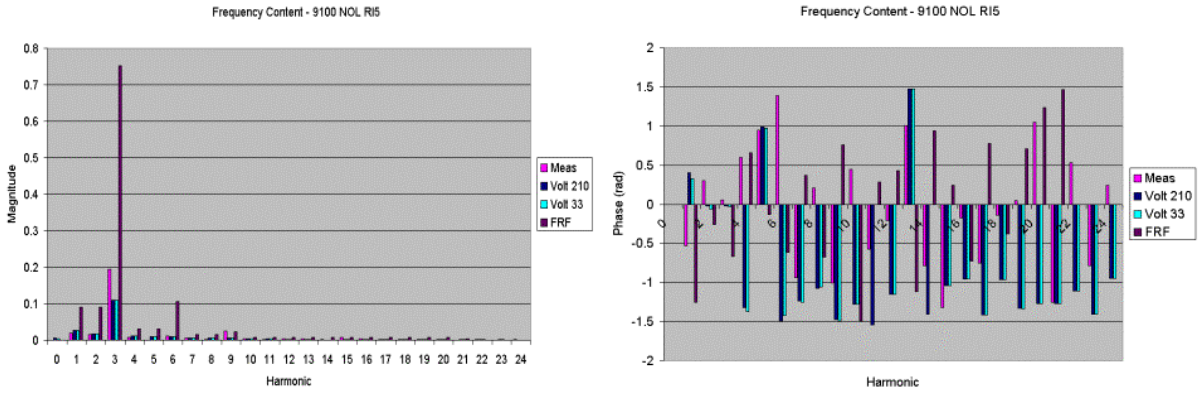

Figure 7.21. Frequency content of Volterra and tuned FRF predictions of 9100 NOL RI3 R1.

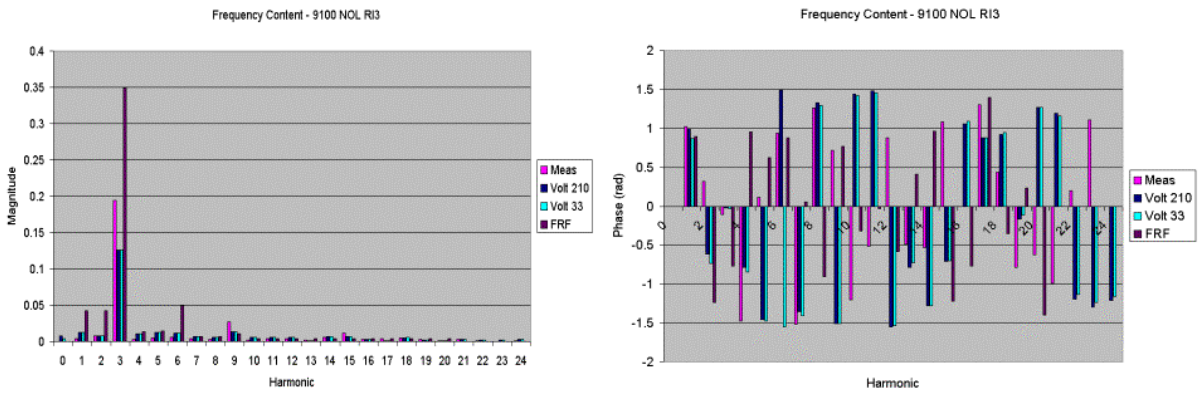

Figure 7.22. Frequency content of Volterra and tuned FRF predictions of 9100 NOL RI5 R1.

Figure 7.23 and Figure 7.24 present prediction accuracy as an average over the first 24 harmonics, and at the dominant distortion frequency, respectively. Recall that accuracy is defined as the ratio of measured and predicted frequency magnitude, where a perfect prediction yields an accuracy of 1.0.

$$Acc = \frac{MeasuredMagnitude}{\Pr edictedMagnitude}$$

Equation 7.4

Notice that the accuracies of both Volterra predictions are very similar at each radial immersion. This again emphasizes the lack of 3rd order influence at this operating condition. On an average over the first 24 harmonics, the Volterra predictions are seen to have out performed the tuned FRF predictions over the majority of the rotor span. Volterra series prediction accuracy at the dominant distortion frequency is consistently better than the tuned FRF over the entire span.

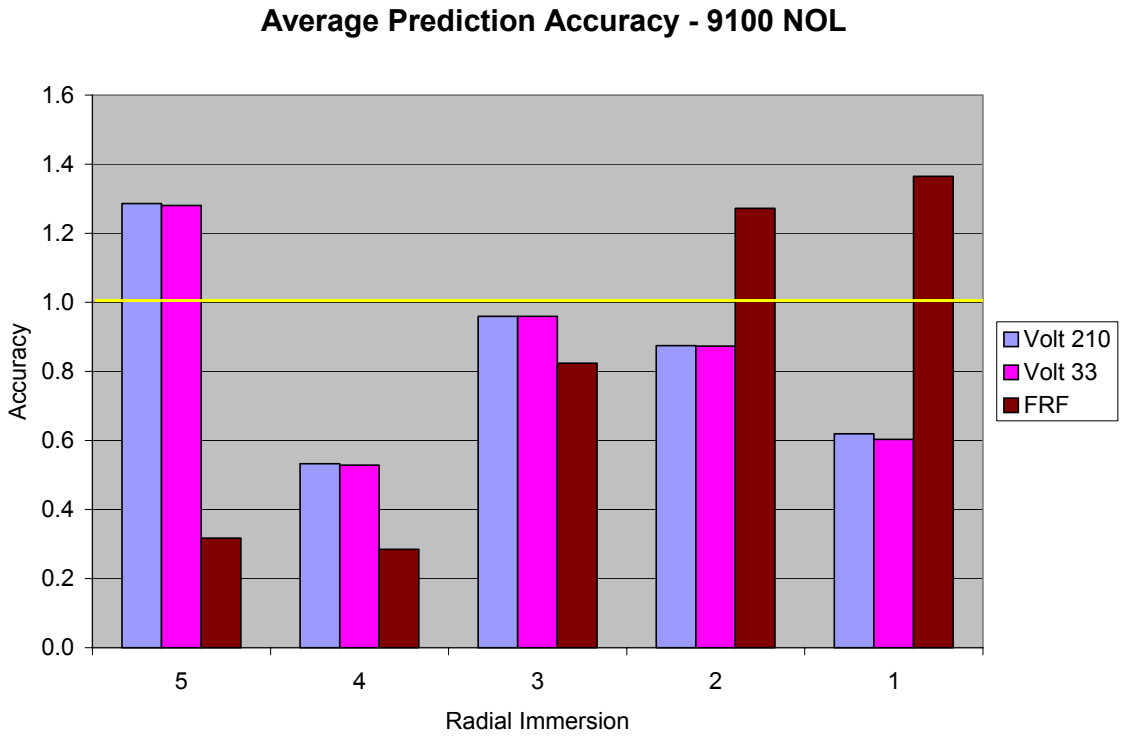

Figure 7.23. Average prediction accuracies over 24 harmonics of 9100 NOL RI1-RI5.

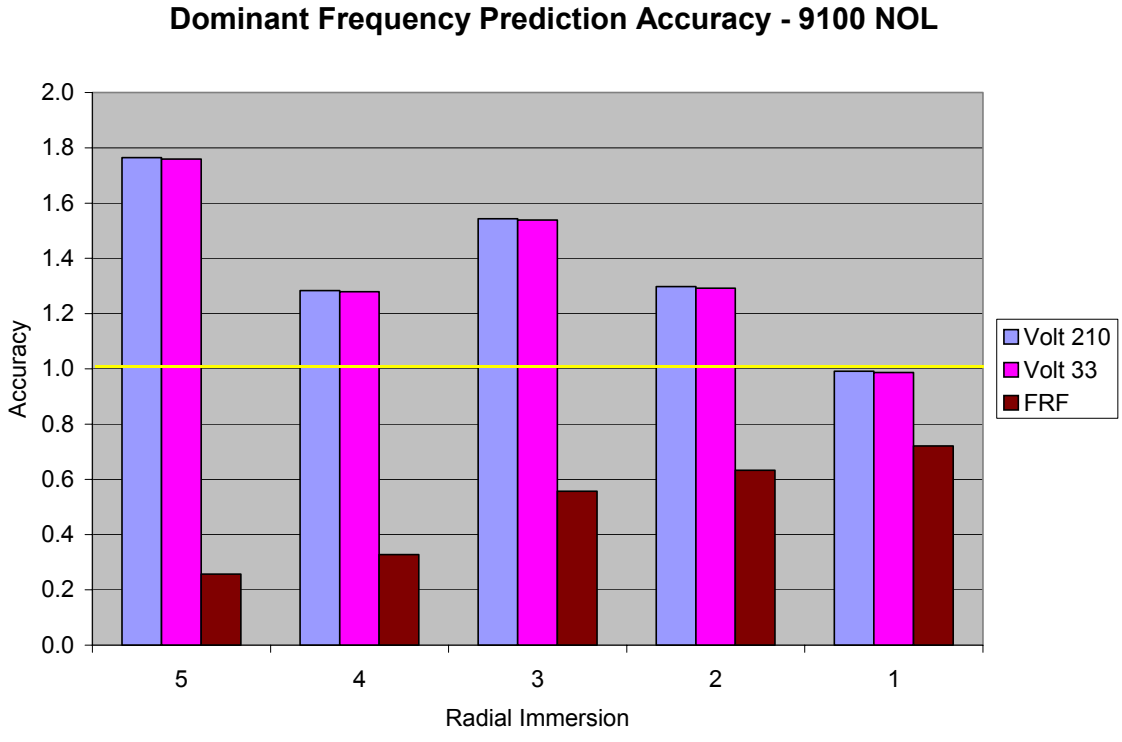

Figure 7.24. Dominant distortion frequency prediction accuracies of 9100 NOL RI1-RI5.

7.5.2 Comparison of 9500 PE Predictions

The next operating conditions to be examined are 9500 PE RI1 – RI5 R1, where again time-series and frequency comparisons will be made. Recall that 9500 rpm is also a speed used in kernel training; however, Peak Efficiency is a novel operating condition at this speed. Figure 7.25 provides time-series comparisons of 2nd and 3rd order Volterra, and tuned FRF predictions. At this condition the differences in 2nd and 3rd order Volterra predictions are more apparent than those at 9100 rpm, signifying that there is a greater 3rd order, nonlinear influence at 9500 rpm. All predictions have recreated the 8 per rev distortion waveform at near tip radial immersions, however the Volterra predictions show a minimal response at near hub predictions, particularly RI5. The tuned FRF, however, has captured a distinct 8 per rev waveform at the RI5 position, and qualitatively appears to be the preferred predictor in this case.

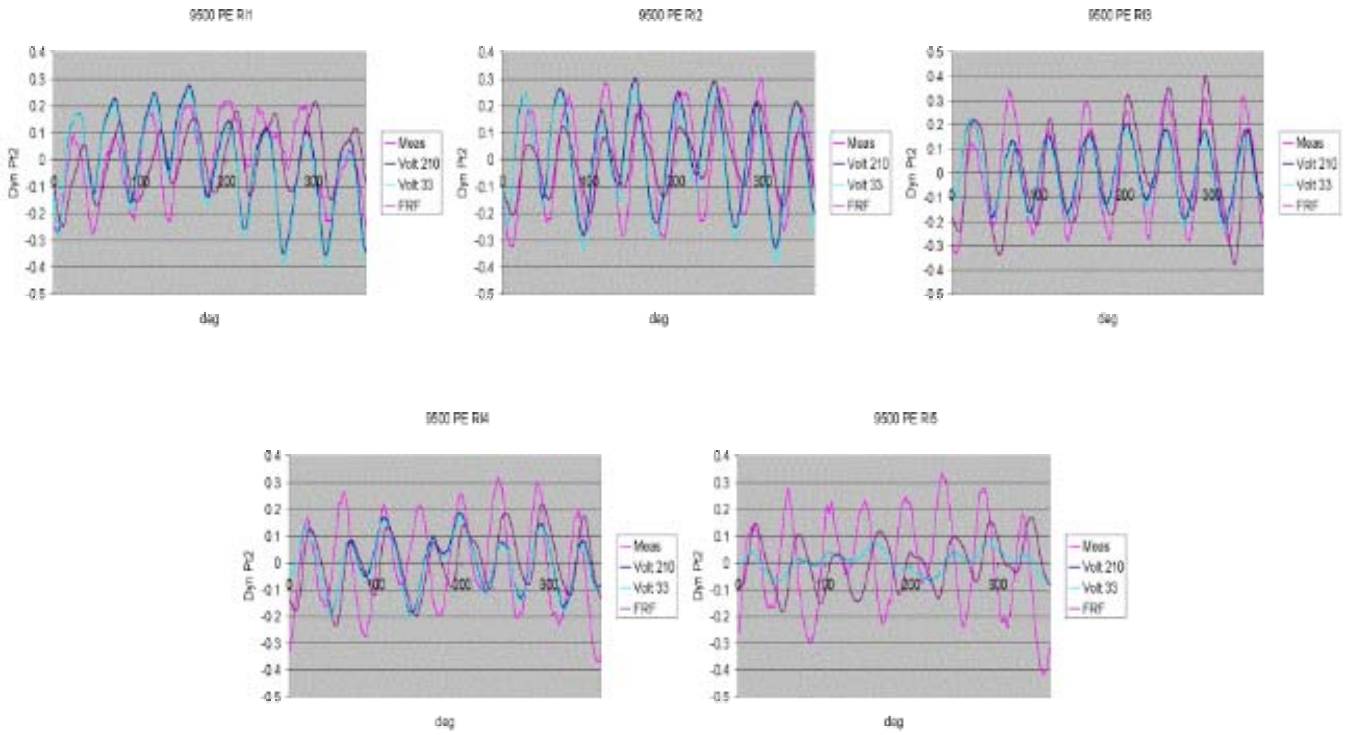

Figure 7.25. Time-series Volterra and tuned FRF predictions of 9500 PE RI1-RI5 R1.

The frequency content of 9500 PE RI1, RI3, and RI5 predictions will now be considered. Figure 7.26, Figure 7.27, and Figure 7.28 present plots of frequency content at

these positions. As seen in Figure 7.26 the Volterra predictions at RI1 are in phase with measured data, however have over predicted the dominant frequency magnitude by nearly 25%. The tuned FRF prediction at this position has a much closer to measured magnitude prediction, however it is out of phase. At midspan, both predictors have underestimated the dominant frequency magnitude, while the tuned FRF is in phase and Volterra predictions are out of phase. As expected from the time-series comparisons, Volterra predictions at the near hub (RI5) position have severely under predicted the dominant frequency magnitude. Volterra predictions appear to have actually created a 2 per rev dominant distortion waveform at this radial immersion.

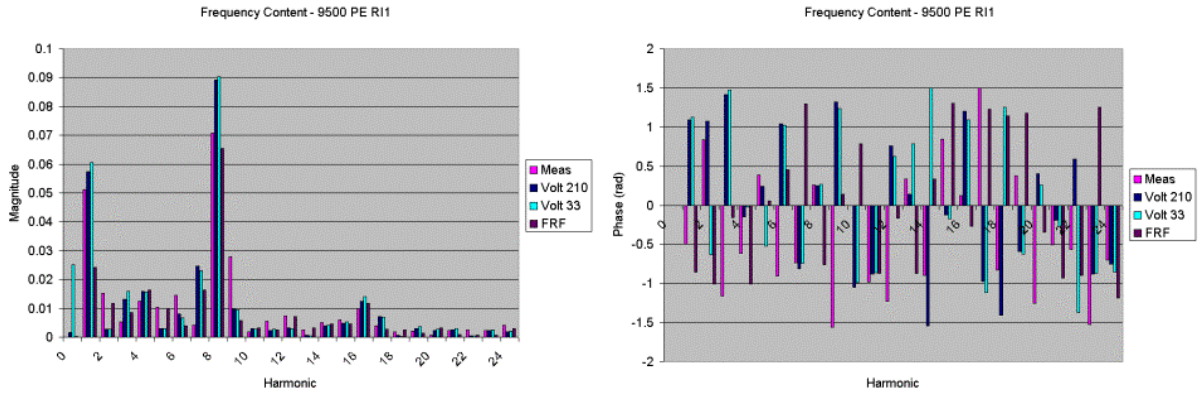

Figure 7.26. Frequency content of Volterra and tuned FRF predictions of 9500 PE RI1 R1.

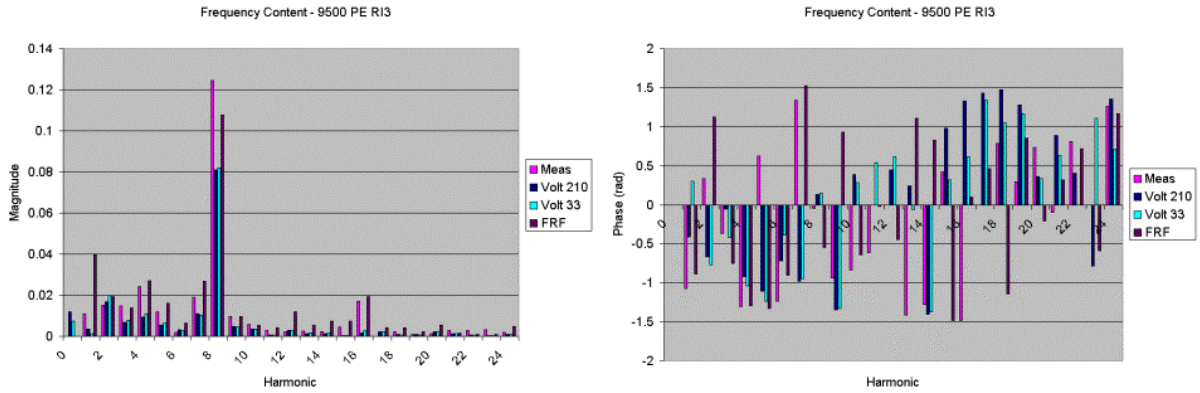

Figure 7.27. Frequency content of Volterra and tuned FRF predictions of 9500 PE RI3 R1.

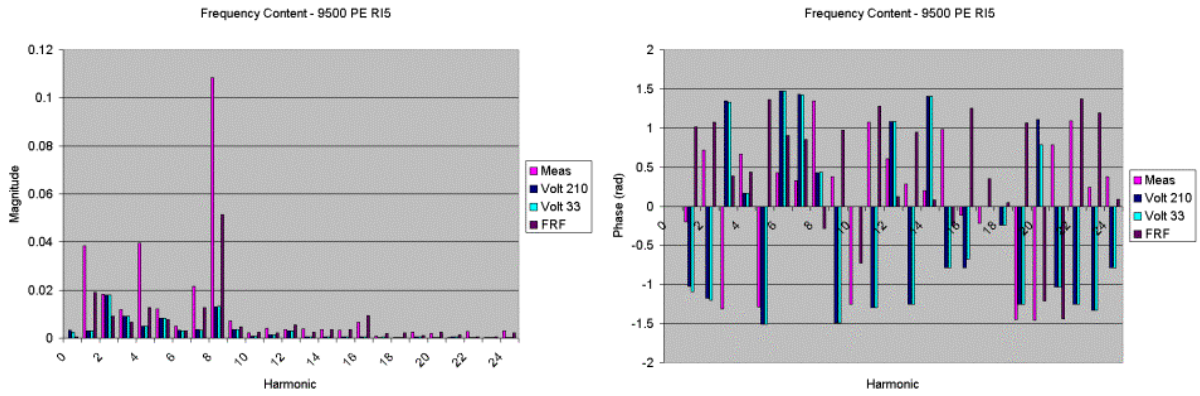

Figure 7.28. Frequency content of Volterra and tuned FRF predictions of 9500 PE RI5 R1.

Prediction accuracy results for 9500 PE are provided in Figure 7.29 and Figure 7.30. Note the particular lack of accuracy in Volterra predictions at the near hub (RI5) predictions. These points appear to be outliers from a more consistent performance over the remaining radial immersions. Based on the results presented in these tables, the tuned FRF model appears to be the more accurate predictor at this operating condition.

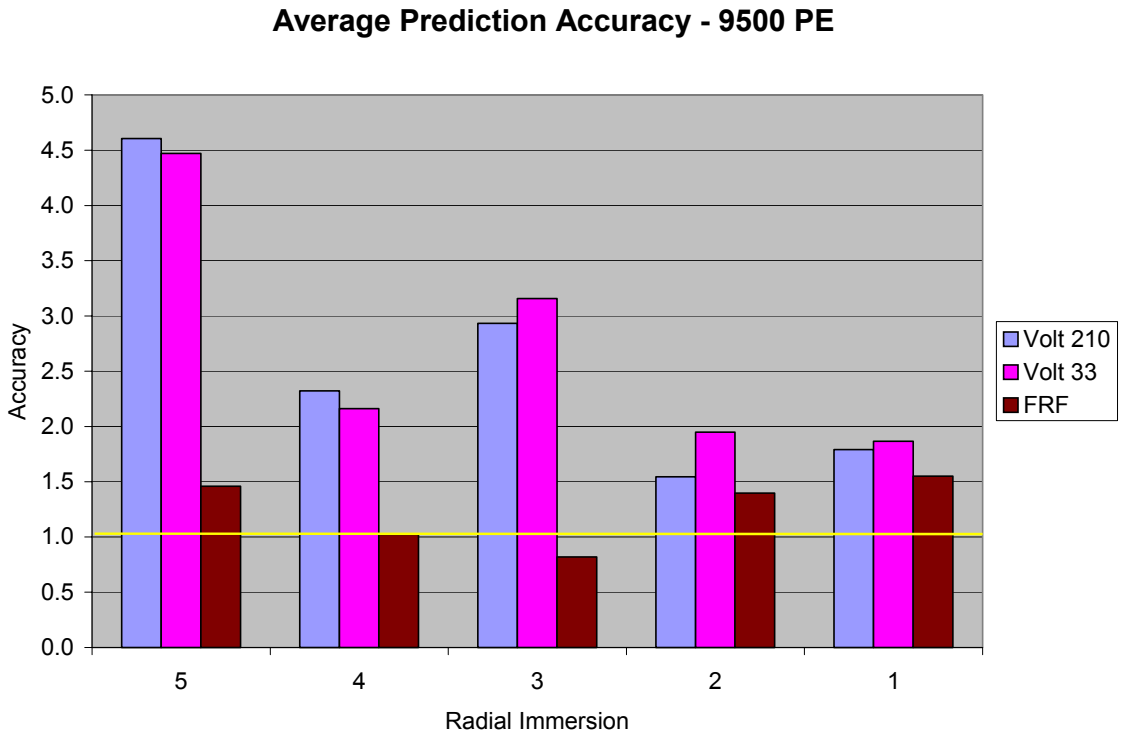

Figure 7.29. Average prediction accuracies over 24 harmonic of 9500 PE RI1-RI5.

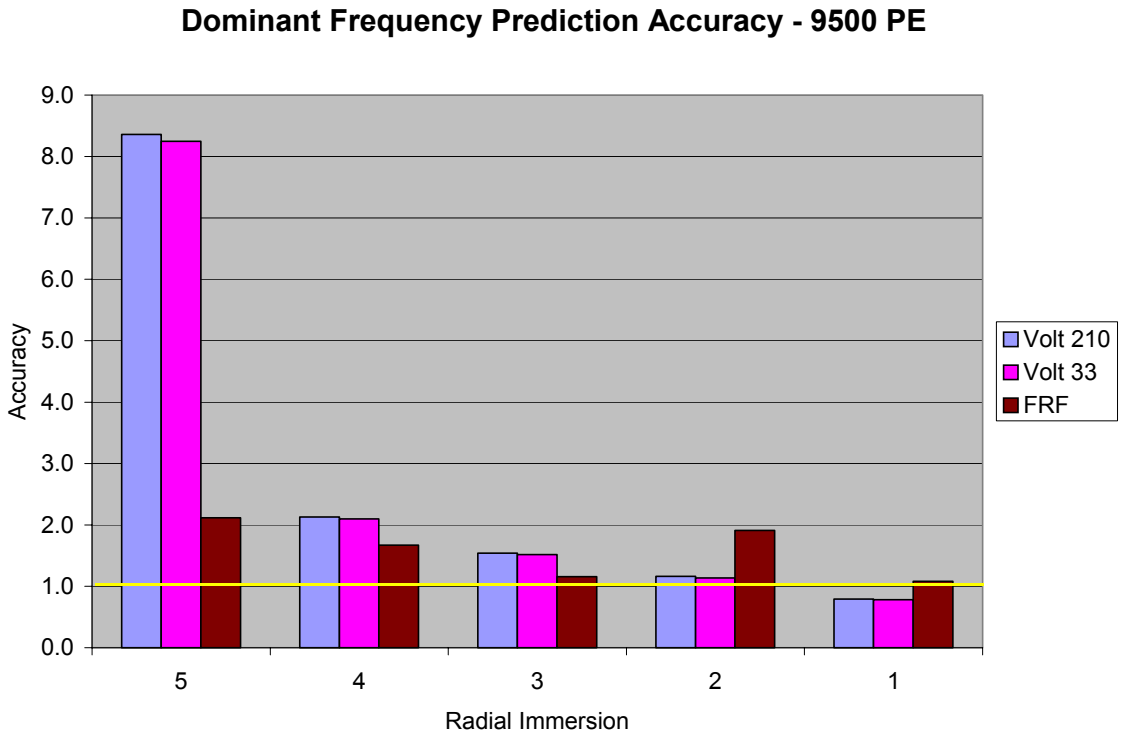

Figure 7.30. Dominant distortion frequency prediction accuracies of 9500 PE RI1-RI5.

7.5.3 Comparison of 13200 WOD Predictions

The same Volterra predictions of 13200 WOD RI1 – RI5 R1 presented in Section 7.4 will now be compared with tuned FRF predictions. Time-series comparisons are provided in Figure 7.31. Again, the difference in 2nd and 3rd order Volterra predictions is evident, even more so than at 9500 PE. This trend of increasing nonlinear dependence with increasing rotational speed is of little surprise. As compressor speed increases, rotor through-flow becomes increasingly supersonic over a greater portion of rotor span, thereby escalating flow non-linearity. Notice that the tuned FRF predictions have a periodic 8 per rev waveform. However, unlike Volterra predictions, the tuned FRF has not captured the details of the distortion patterns. As demonstrated in Section 7.4, these waveform details are a nonlinear result. Once again the tuned FRF has captured the distortion waveform at the near hub (RI5) position, while Volterra predictions show minimal response.

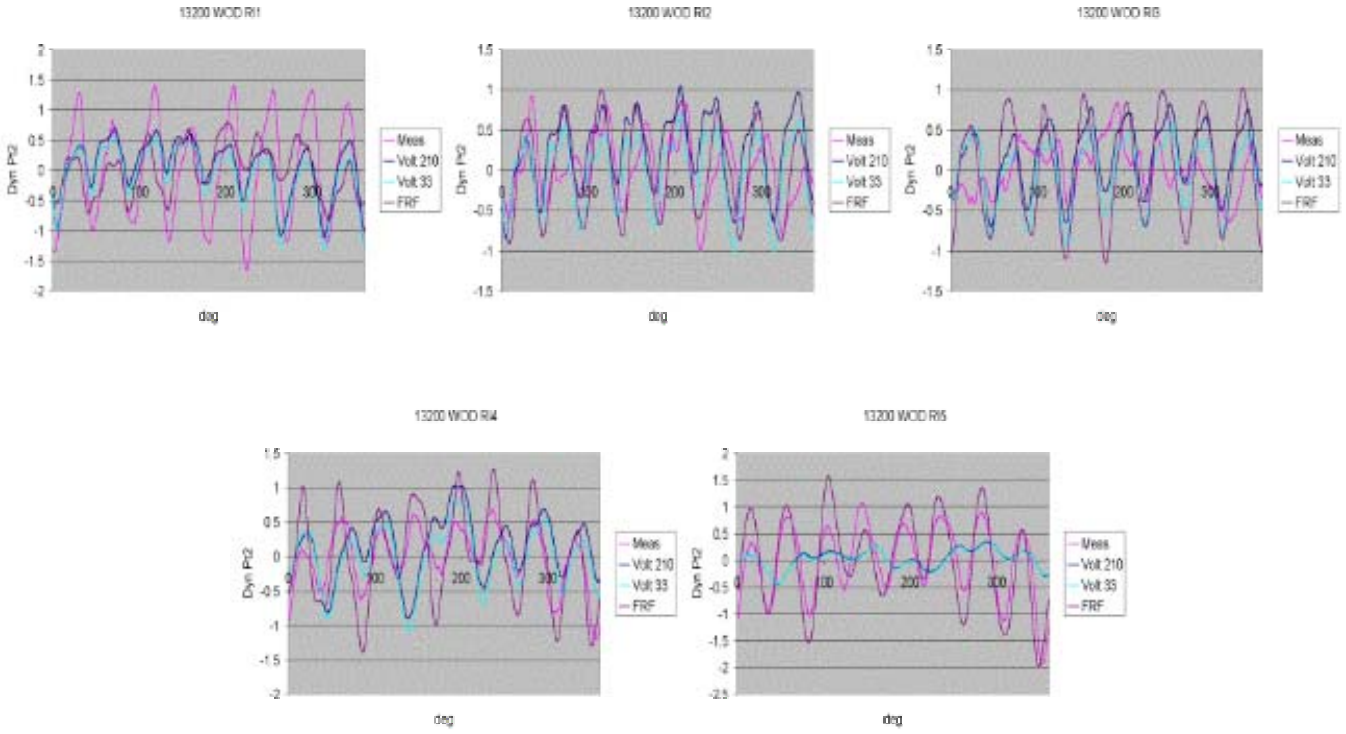

Figure 7.31. Time-series Volterra and tuned FRF predictions of 13200 WOD RI1-RI5 R1.

Frequency content of predictions at RI1, RI2, and RI5 will now be presented. The change is presentation from midspan (RI3) to RI2 results has occurred due to the emphasis placed on the RI2 distortion pattern in previous sections. Frequency content of these radial immersions is shown in Figure 7.32, Figure 7.33, and Figure 7.34. Results here are similar to those seen for 9500 PE predictions. Near hub (RI5) Volterra predictions are extremely underestimated while the tuned FRF has done well at matching the frequency content at this position.

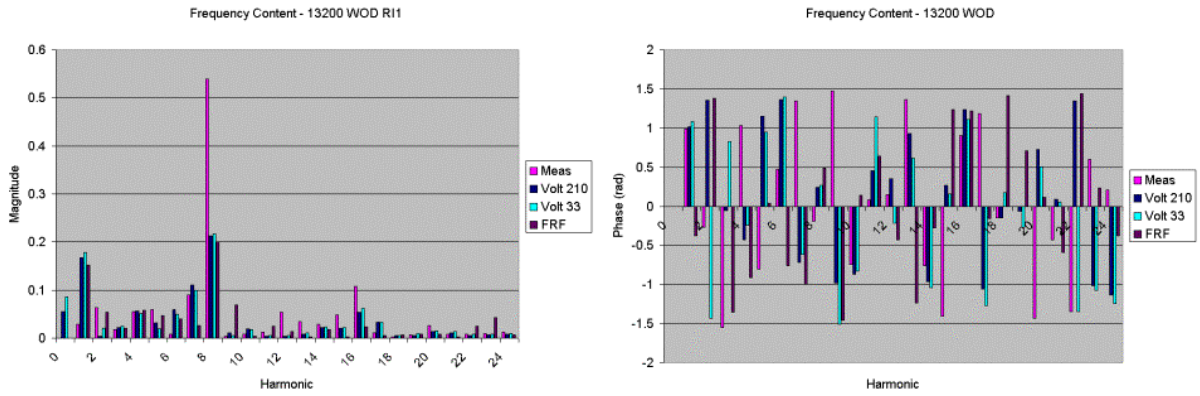

Figure 7.32. Frequency content of Volterra and tuned FRF predictions of 13200 WOD RI1 R1.

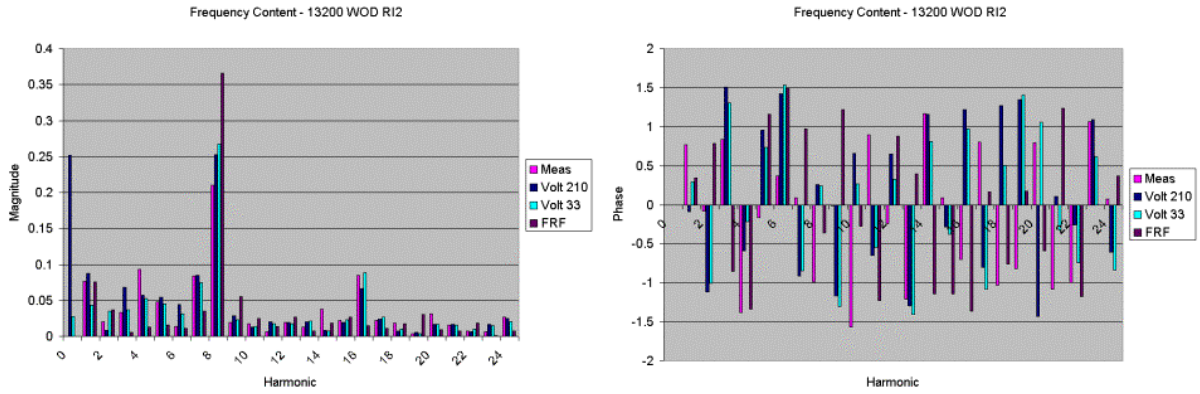

Figure 7.33. Frequency content of Volterra and tuned FRF predictions of 13200 WOD RI2 R1.

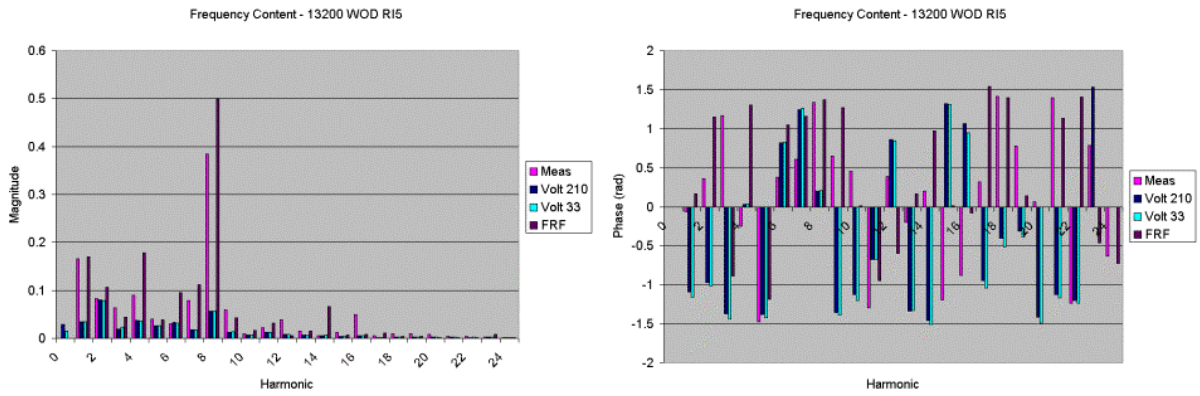

Figure 7.34. Frequency content of Volterra and tuned FRF predictions of 13200 WOD RI5 R1.

Prediction accuracy results at 13200 WOD are provided in Figure 7.35 and Figure 7.36. Again, the lack of prediction accuracy at near hub conditions, particularly RI5, is emphasized in these plots. There is an apparent decrease in accuracy of Volterra predictions at this operating condition. This is to be expected to some degree, considering that Volterra kernels are trained with data at 9100 rpm and 9500 rpm. There is a considerable gap in speed lines when making predictions of the 13200 rpm data sets. Volterra predictions are, however, more accurate at near tip radial immersions. Volterra predictions are particularly accurate at the dominant 8th harmonic.

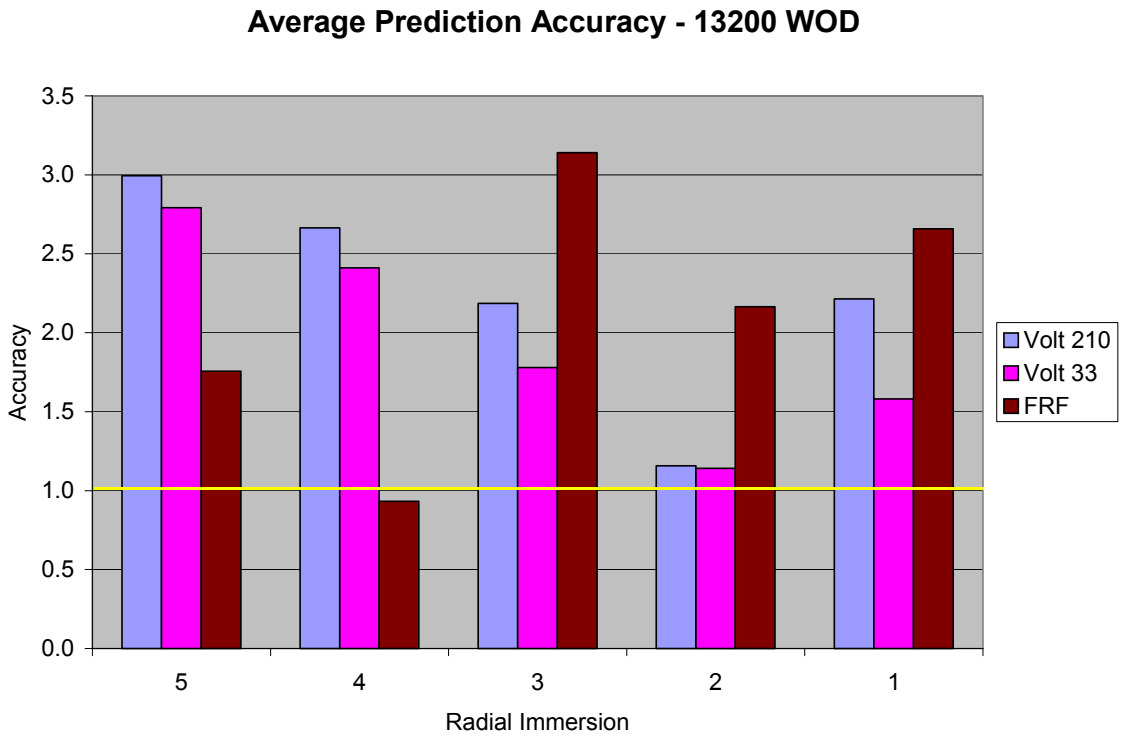

Figure 7.35. Average prediction accuracies over 24 harmonics of 13200 WOD RI1-RI5.

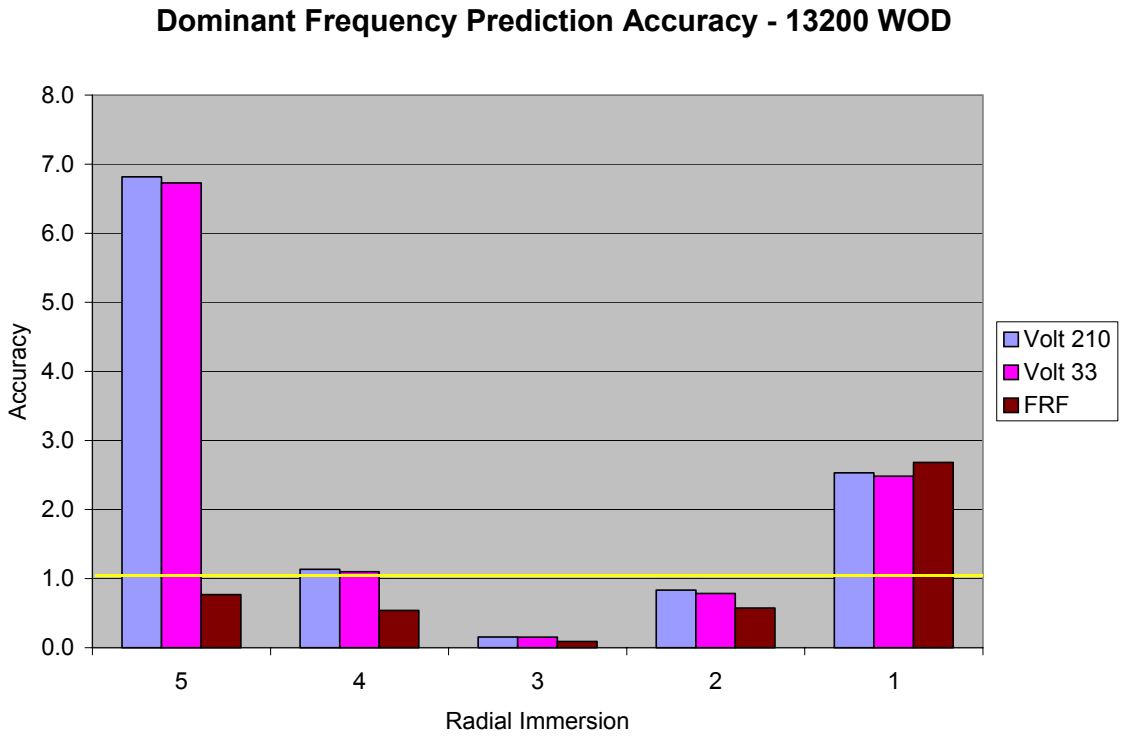

Figure 7.36. Dominant distortion frequency prediction accuracies of 13200 WOD RI1-RI5.

8 Total Pressure Distortion Dependencies

8.1 Radial Accuracy of Volterra Predictions

As pointed out in previous sections, the accuracy of Volterra series predictions at high-speeds varies greatly over the span of the rotor. While near-tip predictions have been seen to be of consistently good accuracy, near-hub predictions are very inaccurate, hardly capturing the dominant distortion waveform. Section 7.4, has shown that the lack of near hub response in Volterra predictions is a consistent result for 1st, 2nd, and 3rd order predictions, and therefore is not necessarily a function of system non-linearity. This section will examine the radial and speed dependencies of distortion predictions, offer possible causes for this dependence, and introduce new methods of accounting for these dependencies in Volterra predictions.

Figure 8.1, Figure 8.2, and Figure 8.3 illustrate Volterra prediction accuracy at each of the first 24 harmonics across the span of the rotor at each speed line, respectively. The accuracy of each radial immersion is signified by a distinct symbol, with accuracies at the dominant frequency circled in red and those of all higher harmonics of the dominant frequency circled in blue. Given a plot of this nature and the definition of accuracy in this study, one would hope to see a small grouping of accuracy points at all five radial immersions centered around 1.0. This is generally seen to be the case at 9100 rpm in Figure 8.1, with a few outliers included. There is a small cluster of points near 1.0 indicating consistent prediction accuracy across the span of the rotor. However, at 9500 rpm and 13200 rpm, the same results do not apply. A wide scatter over a large range of accuracies is seen at each of the harmonics, with the near hub (RI5) accuracy consistently being the outlier. Figure 8.2 and Figure 8.3 provide a clear picture of the decrease in prediction accuracy at near hub streamlines at high-speed conditions.

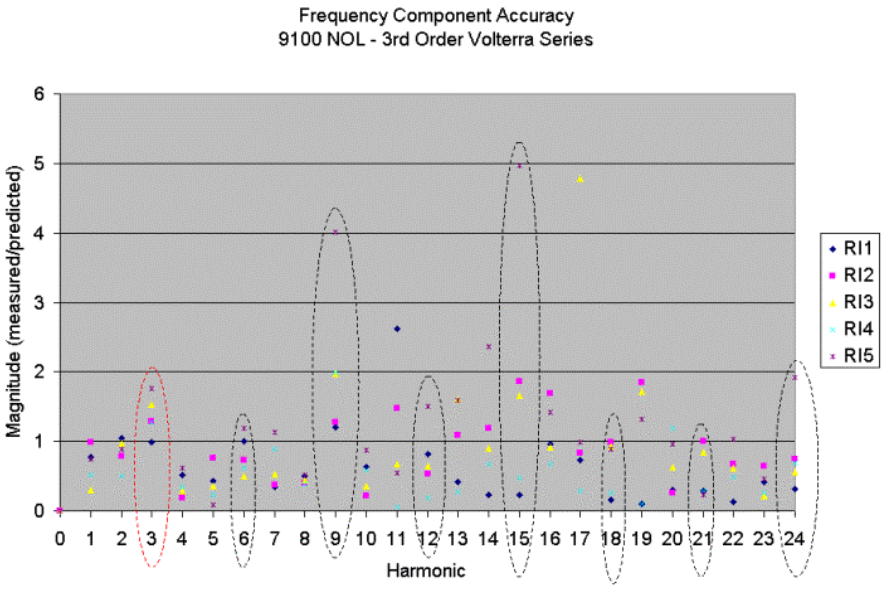

Figure 8.1. Radial frequency accuracy of 3rd order Volterra series predictions of 9100 NOL R1.

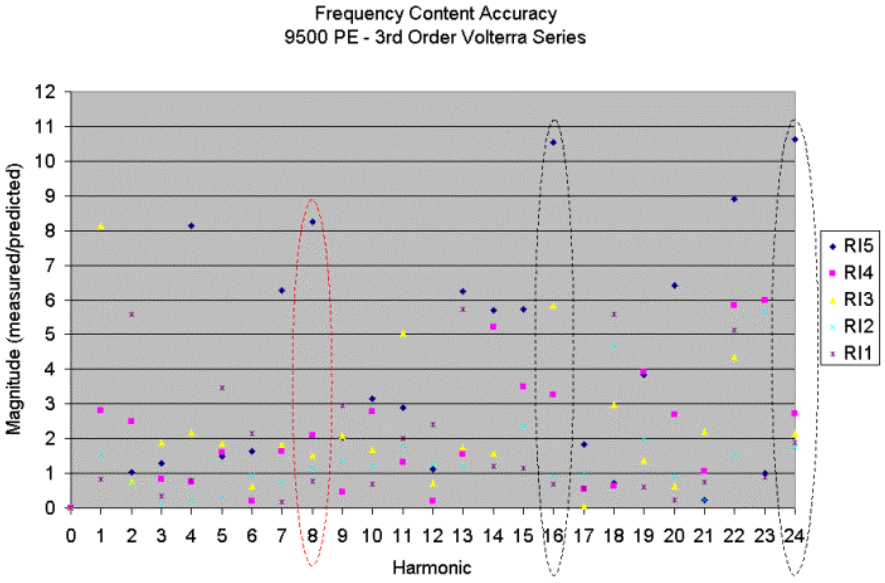

Figure 8.2. Radial frequency accuracy of 3rd order Volterra series predictions of 9500 PE R1.

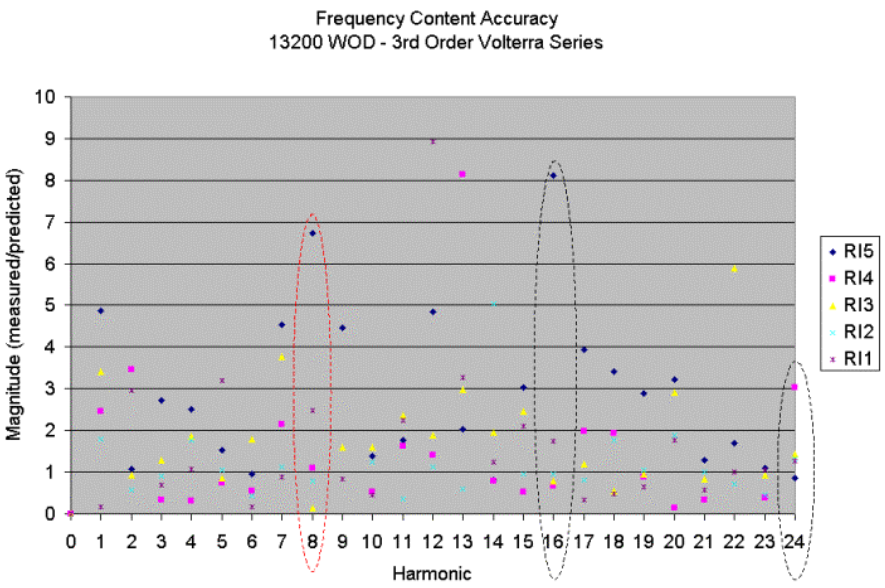

Figure 8.3. Radial frequency accuracy of 3rd order Volterra series predictions of 13200 WOD R1.

8.2 Understanding the Radial and Speed Dependencies of Total Pressure Distortion Propagation

Now that the general trend of decreasing prediction accuracy at near hub, high-speed conditions has been identified, it is important to understand the causes of this in order to develop prediction techniques to overcome it. Multiple issues will be considered in determining the source of total pressure distortion dependences. These consist of inlet total pressure distortion properties and compressor operating characteristics.

The first source of prediction dependency lies in the properties of the rotor inlet distortion patterns. Inlet distortion patterns will be examined through color contour plots of the dynamic total pressure at 9100 NOL, 9500 PE, and 13200 WOD in Figure 8.4, Figure 8.5, and Figure 8.6, respectively. In Figure 8.4 the 3 per rev distortion pattern characteristic of 9100 rpm is apparent. Notice that the extreme distortion areas, indicated by red and blue, are consistent over the span of the rotor. The fact that distortion intensity is consistent across the span at 9100 rpm agrees well with the findings of consistent prediction accuracy from hub to tip at this speed.

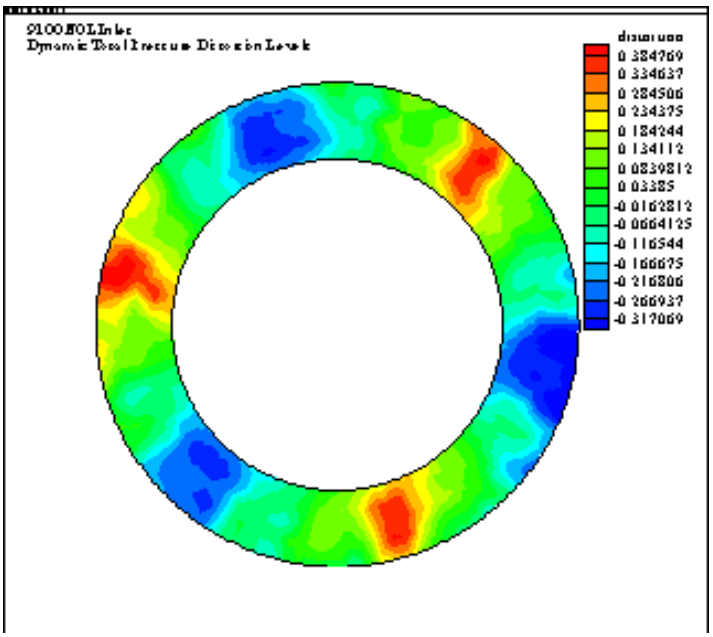

Figure 8.4. Inlet dynamic total pressure distortion pattern at 9100 NOL R1.

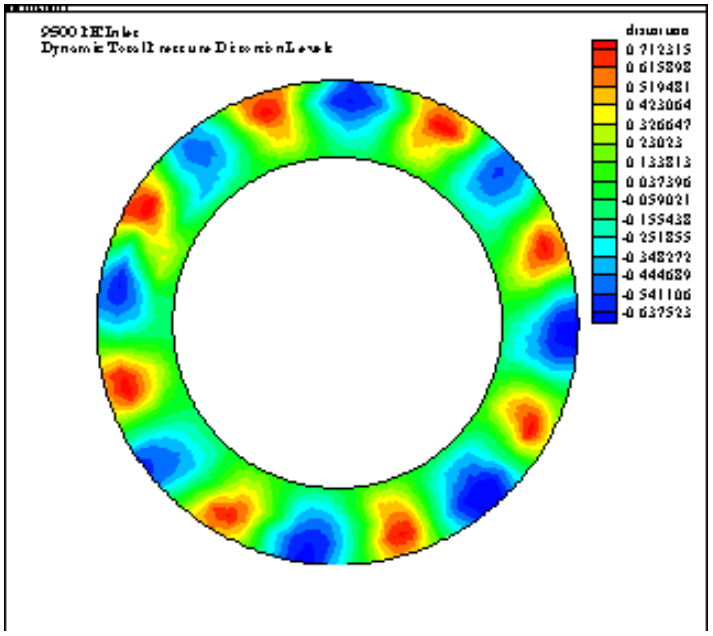

Figure 8.5. Inlet dynamic total pressure distortion pattern at 9500 PE R1.

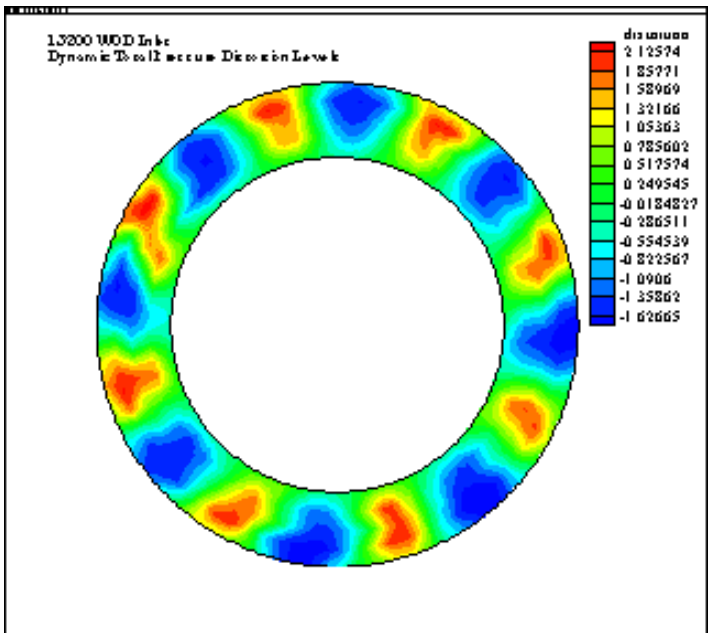

Figure 8.6. Inlet dynamic total pressure distortion pattern at 13200 WOD R1.

Now, focus is turned to the plots of 9500 rpm and 13200 rpm. Here, the 8 per rev distortion patterns are noticeable. However, at these speeds the distortion extremes are not consistent across the rotor span. Near hub distortions are noticeably dissimilar to those over the remainder of the hub, showing minimal deviations in each case. In fact, closer examination of inlet distortion patterns at 9500 rpm and 13200 rpm reveals that hub inlet distortions are generally only 10% - 15% of those at near tip radial immersions. This discrepancy in inlet distortion intensity across the rotor correlates directly with the lack of prediction accuracy near the hub. Because all five radial immersions have been included in the training of Volterra kernels, the model has knowledge of the range of distortion intensities downstream of the rotor, however it is unaware of where these differences occur. In other words, the model cannot distinguish between streamlines when trained with several radial immersions. As a result, the minimal distortions at near hub positions are not properly amplified through the rotor, which leads to severely under predicted downstream distortion pattern.

Other factors to consider in this investigation of distortion dependence are the operating characteristics of the rotor itself. This is a transonic rotor, meaning that a portion of the rotor span will experience subsonic flow while the remainder will

experience either sonic or supersonic flow. The rotor is designed to be transonic at nearly 45% span, roughly RI3, when operating at design conditions on a standard day. This means that RI1 and RI2 experience supersonic flow while RI3 experiences nearly sonic flow, and RI4 and RI5 experience subsonic flow. The existence and degree of non-linearity in subsonic and supersonic flow vary greatly. Shock systems develop in supersonic flow, which have a direct effect on the pressure rise across the rotor, and are inherently nonlinear phenomena. Therefore the characteristics of the rotor are seen to play a role in the radial and speed dependencies of total pressure distortion propagation.

9 *Methods of Accounting for Distortion Radial and Speed Dependence*

9.1 Removing Radial and Speed Dependence from Nonlinear Volterra Predictions

With a better understanding of the radial and speed dependence of distortion patterns, it appears desirable to remove such dependencies from Volterra predictions. Two methods of accomplishing this task will be discussed. The first method focuses solely on removing the radial distortion dependence from Volterra predictions by training Volterra kernels along individual streamlines with data sets representative of only the streamline to be predicted on. The second method aims at removing all dependencies from distortion patterns by normalizing data sets, both training and prediction, with physics-based parameters representative of the operating characteristics of the rotor. Each of these methods will be discussed in depth in the following sections. Results of both methods will then be presented simultaneously and be compared with traditional Volterra predictions.

9.2 Training Volterra Kernels Along Individual Streamlines

The first method for removing radial dependence from distortion pattern predictions consists of a technique termed radial kernel training. This technique treats each streamline within the rotor as a separate total pressure distortion propagation system. In other words, a Volterra series will be created for each individual streamline with kernels based on data solely representative of the streamline at hand. This process inherently removes radial dependence from Volterra predictions by basing them on one set of radial characteristics. Specific findings of Volterra kernel training along individual streamlines include:

- Significant improvement of near hub (RI5) predictions.

- Loss of time-series distortion detail in high-speed predictions (consequence of under training kernels).

Because of the limited amount of data available for kernel training, radially trained kernels must be trained with an altered schedule from that presented in Section 6.2. If the original training schedule were to be followed with the additional concept of radial training, each kernel would be based on only three or four data sets. This would lead to severely under-trained kernels. Recall that in traditional Volterra kernel training, twenty data sets were used to train each kernel. For this method of radially trained Volterra kernels, kernels will be trained with same streamline data sets from each operating condition of each speed other than that speed at which predictions will be made. Because distortion patterns at 9100 rpm have been shown to have little, if any, radial dependence, the concept of training Volterra kernels along individual streamlines will be applied to predictions at 9500 rpm and 13200 rpm only. Example kernel training schedules for RI1 to be applied in radial kernel training are outlined in Table 9.1. Note that even with these alterations in kernel training schedules, only seven or eight data sets will be used to train the kernels. The issue of under trained kernels is still very much at hand, and will be discussed further. Results of radially trained predictions as applied to a 3rd order Volterra series will be presented in Section 9.4.

Table 9.1 Example RI1 Kernel Training Schedule to be Applied in Radial Kernel Training

Prediction Data Set	Kernel Training Data Sets	
9500 PE RI1	9100 NOL RI1	13200 NOL RI1
	9100 NS RI1	13200 NS/PE RI1
	9100 PE RI1	13200 WOD RI1
	9100 WOD RI1	
13200 WOD RI1	9100 NOL RI1	9500 NOL RI1
	9100 NS RI1	9500 NS RI1
	9100 PE RI1	9500 PE RI1
	9100 WOD RI1	9500 WOD RI1

9.3 Normalization of Volterra Predictions by Physics-Based Parameters

In order to address the issue of radial and speed dependencies of inlet total pressure distortions, the concept of normalizing data sets by non-dimensional, physics-based parameters has been investigated. Initial results show improvement upon traditional Volterra series predictions and comparable results with radially trained Volterra series. Specific findings of normalized predictions include:

- Gain in frequency content accuracy over traditional Volterra predictions.
- Recreation of time-series distortion detail when predicting at high-speed conditions.
- Negligible improvement of near hub (RI5) predictions over traditional Volterra predictions.

9.3.1 Normalization Parameters

Several parameters have been examined for their influence on the prediction of total pressure distortion patterns in a Volterra series model. Included in these parameters are transport time, radial position, rotor speed, shock strength, and reduced frequency. All parameters are applied to the data both by themselves, and in a combination of several parameters. Training and prediction data sets are normalized in the process. Multiplying both the input and response data by the normalization parameters normalizes training data sets. Input prediction data are also multiplied by the parameters, while Volterra predictions are divided by the parameters.

Time non-dimensionalization has been included in all Volterra models. This has been found to be a necessary step in the expansion of kernels into basis function space. All time-series are non-dimensionalized by the parameter

$$t_{nd} = \frac{Chord}{W}$$

Equation 9.1

where Chord is the blade chord length and W is the average relative velocity across the rotor, both defined at each particular operating condition and radial immersion. The units of t_{nd} are seen to be (s^{-1}), and therefore will yield a non-dimensional term when multiplied by the initial time-series. By including relative velocity in this term, the parameter contains information concerning the fluid axial and radial velocities at the conditions for which it is defined. Blade chord length has also been included in this parameter. Convection speed, the speed at which total pressure distortions travel through the rotor, is a function of this length.

The second parameter examined is a radial correction factor. Because inlet distortion intensity has been found to have high radial dependence, this term is aimed at normalizing variations in distortion levels over the five radial immersions. The parameter is defined as,

$$r_{nd} = \left(\frac{r}{r_{tip}} \right)^2 .$$

Equation 9.2

This non-dimensional parameter presents a ratio of radial immersion radius to tip radius, where the strongest distortion intensities are found.

The next parameter examined is proportional to rotor speed ($U = r\omega$). This parameter is applied in an attempt to further remove from predictions the dependence of distortion intensity on rotational speed, thus improving predictions at novel speeds not included in kernel training. The parameter is presented as a ratio of the rotor speed at each radial immersion to tip rotor speed. As mentioned previously, tip radius distortions generally have the strongest intensity. The non-dimensional rotor speed parameter is defined as,

$$r\omega_{nd} = \frac{(r\omega)^2}{(r\omega)^2_{tip}}.$$

Equation 9.3

Another normalization parameter examined is shock strength factor. Here this factor is treated as that for a single normal shock, allowing for simplified calculation based on normal shock relations. The normal shock strength factor is defined as

$$NSF = \frac{P_2/P_1}{P_{02}/P_{01}}$$

Equation 9.4

where P_1, P_2 represent the upstream and downstream static pressure and P_{01}, P_{02} represent the upstream and downstream total pressure. The shock strength factor normalizes total pressure distortions by removing pressure changes induced by shocks. This in effect renders all operating conditions as having a subsonic blade passage through flow velocity [Small, 2001]. All data needed to compute NSF are provided by the streamline curvature code.

The final normalizing parameter examined is reduced frequency. Reduced frequency is a representation of blade response time, and is defined by Bruce as

$$k = \frac{\upsilon * Chord}{2W}$$

Equation 9.5

where k is the reduced frequency, υ is the distortion frequency ($2\pi U/\lambda$), U is the blade rotational velocity, and λ is the distortion wavelength. This parameter accounts for convection speed through the rotor, as well as rotational speed, and acts as a descriptor of the amount of time a total pressure distortion spends in the rotor passage.

9.3.2 Results of Data Normalization

Various predictions have shown that, other than the time parameter that is a necessary component of the kernel extraction process, none of the parameters presented alone has a significant influence on total pressure distortion predictions. However, various combinations of parameters have shown some degree of success. Of these, the best combination was found to consist of the product of reduced frequency and normal shock strength factor,

$$\left(\frac{k}{r}\right) * NSF \, .$$

Equation 9.6

Here the radius at which the parameter is defined normalizes reduced frequency. This normalization term includes information concerning flow velocity, radial position, local convection speed, rotational speed, and shock strength. A limitation of this normalization parameter is that it appears to apply only at high-speeds, namely 9500 rpm and 13200 rpm. Accuracy of distortion pattern predictions based on this and other normalization parameters is drastically reduced at 9100 rpm. This result is not surprising, considering that total pressure distortion levels at 9100 rpm have been shown to be consistent across the span of the rotor, thereby negating the need for a radial correction. Another point to consider is the minimal existence of shocks in the rotor at 9100 rpm. Shown in Figure 9.1 are normal shock strength factors over the span of radial immersions for all three rotational speeds at the NOL operating condition. NSF factors at NOL are representative of all operating conditions for a given speed. Figure 9.1 shows that the NSF for 9100 rpm remains consistently near 1.0 over the span of the rotor, while the NSF for 9500 rpm and 13200 rpm vary with considerably higher levels. An NSF of 1.0 indicates there is no shock induced pressure rise at that condition. The average NSF over the rotor span at 13200 rpm (2.92) is nearly three times that at 9100 rpm (1.08). Because of this, one would not expect the NSF to have much of an impact on the predictions made at 9100

rpm. Due to these results, only normalized predictions at 9500 rpm and 13200 rpm will be considered.

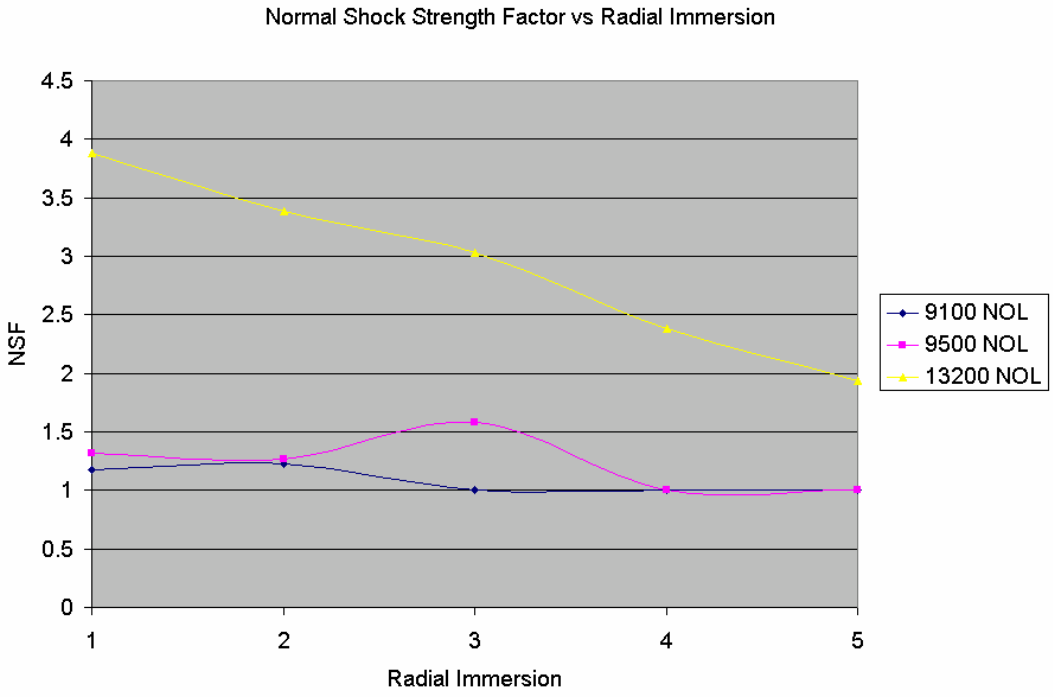

Figure 9.1. Normal shock strength factors over span of rotor for all three speed lines.

9.4 Results and Analysis of Enhanced Volterra Predictions

The first set of enhanced Volterra predictions to be considered is made at 9500 PE R1. Note that in the presentation of results radial Volterra predictions will be referred to as "Volt 33 Rad" and Volterra predictions normalized by the reduced frequency-NSF parameter will be referred to as "Volt 33 Norm". Time-series comparisons of Volt 33, Volt 33 Rad, and Volt 33 Norm predictions, and measured distortion patterns are shown in Figure 9.2. When examining these time comparisons it is apparent that the normalization parameter has had little effect at the near hub (RI5) prediction. However, at all other radial immersions Volt 33 Norm appears to have improved upon the quality of Volt 33 predictions. From the time-series plot of RI5 it is apparent that Volt 33 Rad has had a significant impact at the near hub prediction. A clear 8 per rev distortion waveform

is visible in this prediction. From an initial qualitative review of the predicted waveforms, Volt 33 Rad appears to be the best predictor, creating a distinct waveform at each radial immersion.

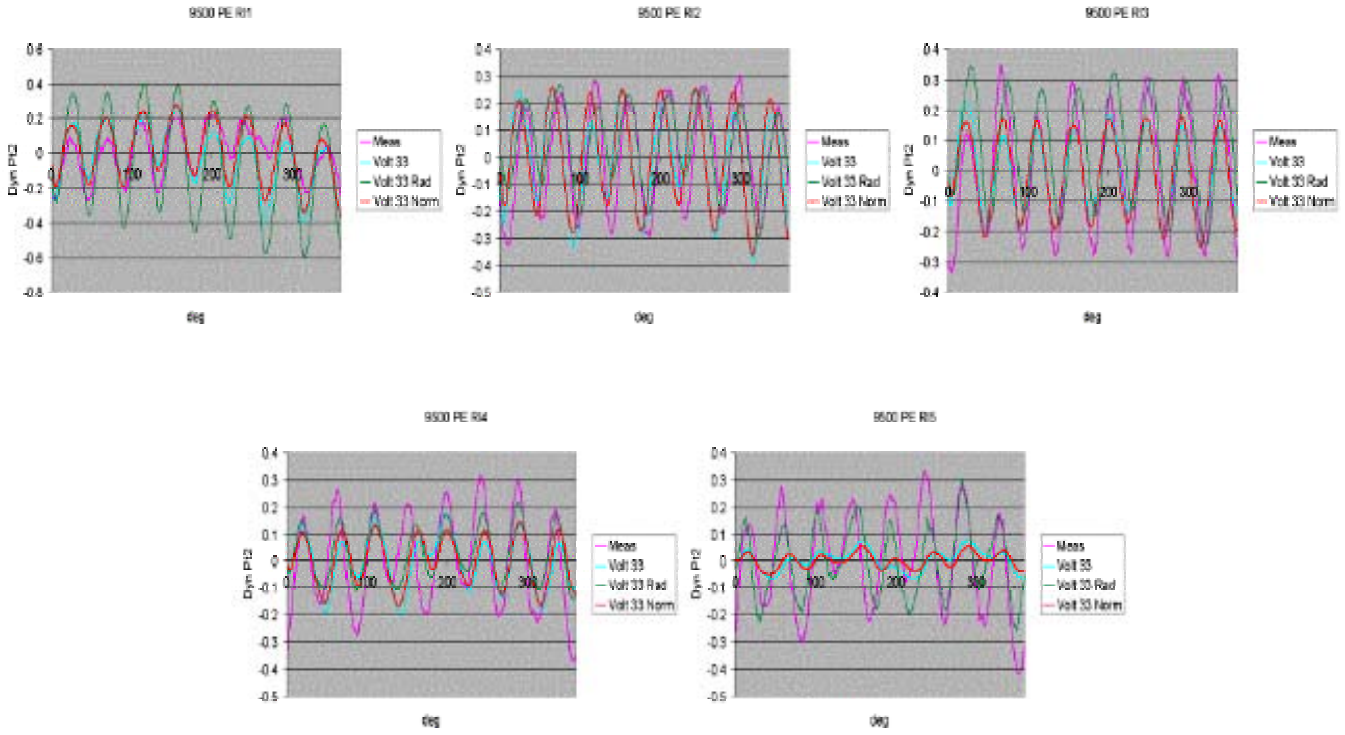

Figure 9.2. Time-series comparisons of Volterra predictions of 9500 PE RI1-RI5 R1.

To further assess the merit of enhanced Volterra predictions, the frequency content of predictions at 9500 PE will be considered. Figure 9.3, Figure 9.4, and Figure 9.5 present the frequency content at RI1, RI3, and RI5, respectively. The dominant frequency, the eighth harmonic, will be focused on in the analysis of these results. At the near tip prediction (RI1), Volt 33 and Volt 33 Norm are seen to be the best predictors, with little difference existing between the frequency content captured by each. As seen in Figure 9.3, the Volt 33 Rad prediction at this condition has well over predicted the waveform, and therefore the frequency magnitude as well. At the midspan prediction (RI3) Volt 33 Norm is seen to slightly improve upon Volt 33's frequency magnitude prediction. However, in this case Volt 33 Rad has done a better job of capturing the frequency content of the downstream distortion pattern, and has corrected the phase

discrepancies of the Volt 33 prediction. At the near hub (RI5) condition Volt 33 and Volt 33 Norm predictions both show minimal response. Each predictor is incapable of capturing the dominant distortion frequency of the waveform at this condition. Volt 33 Rad however, has captured the dominant distortion frequency to within 40% of its magnitude, and is in phase with the measured response.

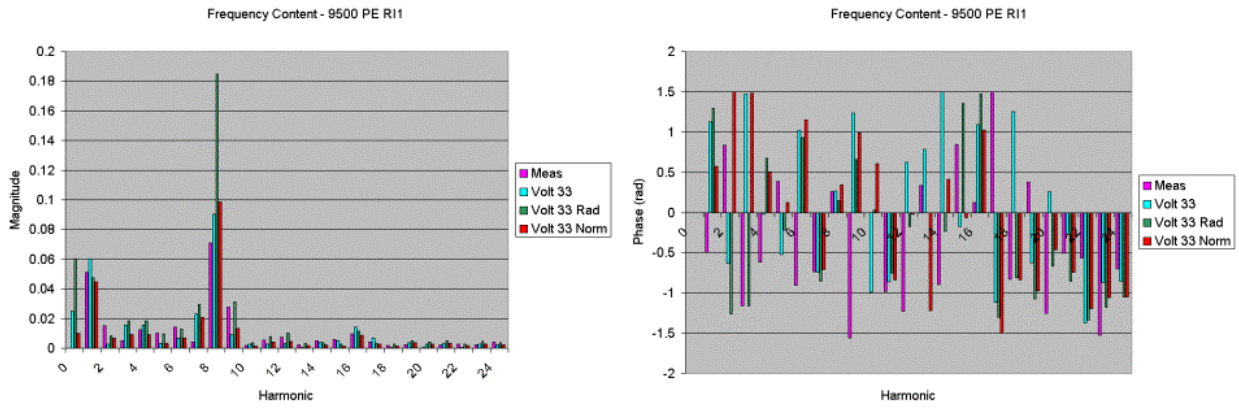

Figure 9.3. Frequency content of Volterra predictions of 9500 PE RI1 R1.

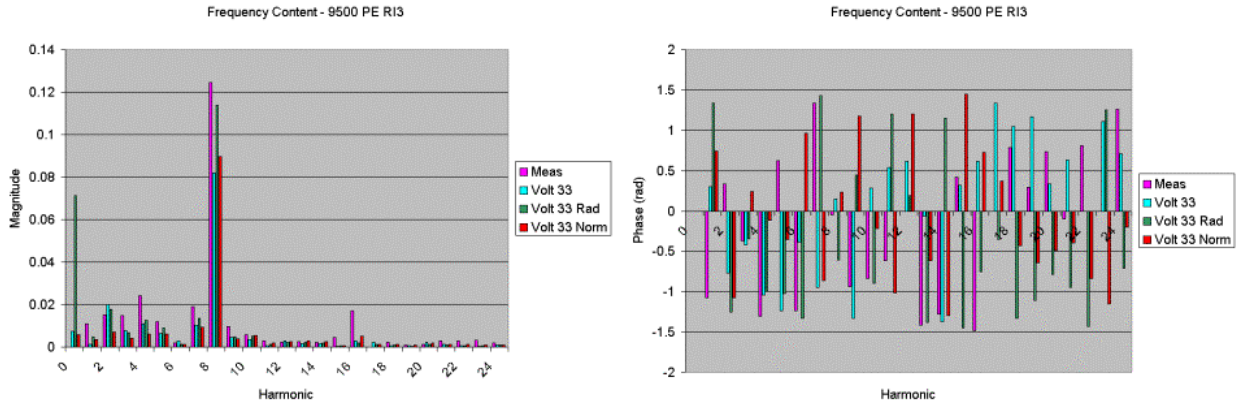

Figure 9.4. Frequency content of Volterra predictions of 9500 PE RI3 R1.

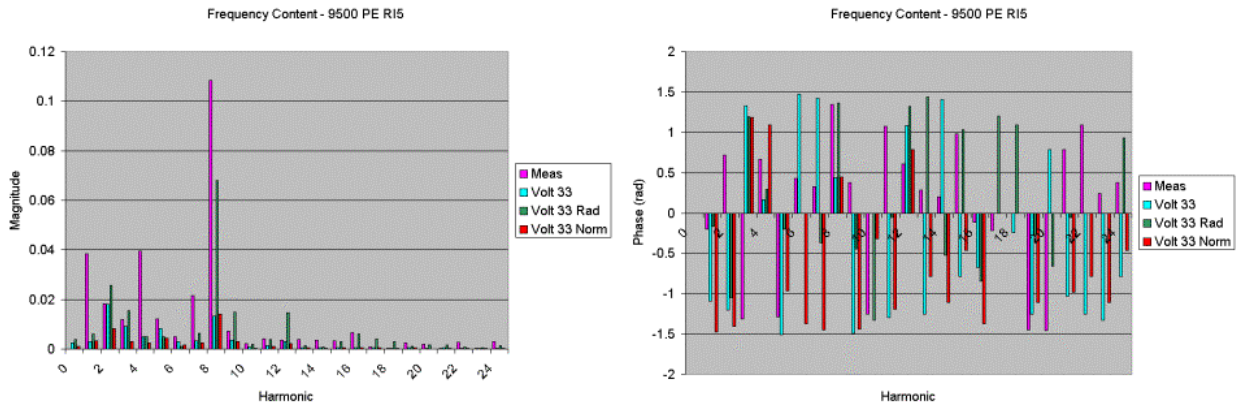

Figure 9.5. Frequency content of Volterra predictions of 9500 PE RI5 R1.

The next data set to be considered is 13200 WOD R1. Again, time-series and frequency content comparisons will be made in order to assess the radially trained and normalized Volterra series predictions. Shown in Figure 9.6 are time-series comparisons of Volt 33, Volt 33 Rad, and Volt 33 Norm predictions, and measured downstream distortion patterns at this condition. The first thing to notice in these comparisons is that the normalized Volterra predictions have captured the detail of the high-speed distortion patterns. However, as can be seen in the time-series plots, the Volt 33 Rad predictions have not captured this detail. This is believed to be a result of under training of the kernels as discussed in Section 9.2. As also seen in the predictions of 9500 PE, the normalization of the Volterra series has had little impact on near hub (RI5) predictions while radially trained predictions show significant improvement in capturing the 8 per rev distortion waveform.

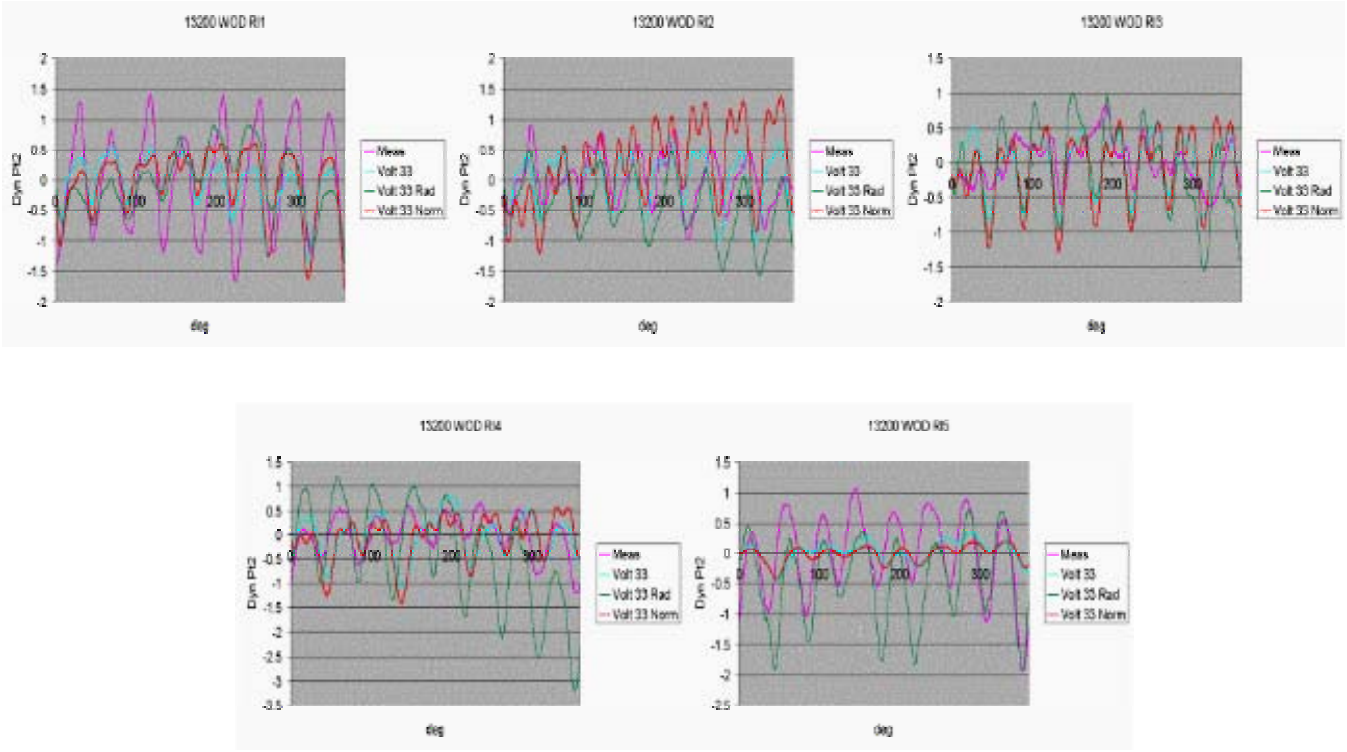

Figure 9.6. Time-series comparison of Volterra predictions of 13200 WOD RI1-RI5 R1.

Now turning focus to the frequency content of the Volterra predictions, plots of frequency magnitude and phase at RI1, RI2, and RI5 are shown in Figure 9.7, Figure 9.8, and Figure 9.9, respectively. At the near tip (RI1) prediction, Volt 33, Volt 33 Rad, and Volt 33 Norm all perform nearly equally, with Volt 33 Norm predicting a slightly more accurate magnitude, however lacking in phase. Each prediction has underestimated the magnitude at the dominant frequency by nearly 50%. Volt 33 Rad is the only prediction in phase with measured data at this radial immersion. At RI2, all Volterra predictions again perform nearly equally, coming within 20% of the dominant frequency magnitude. The Volt 33 Norm prediction again slightly outperforms the other Volterra predictions at this condition. At the near hub (RI5) prediction, Volt 33 Rad is the only prediction that captures a distinctive dominant frequency magnitude at the eighth harmonic, coming within less than 10% of the measured magnitude and is nearly in phase with measured data. All other Volterra predictions show minimal response at the dominant frequency, as is to be expected from the time-series comparisons shown in Figure 9.6.

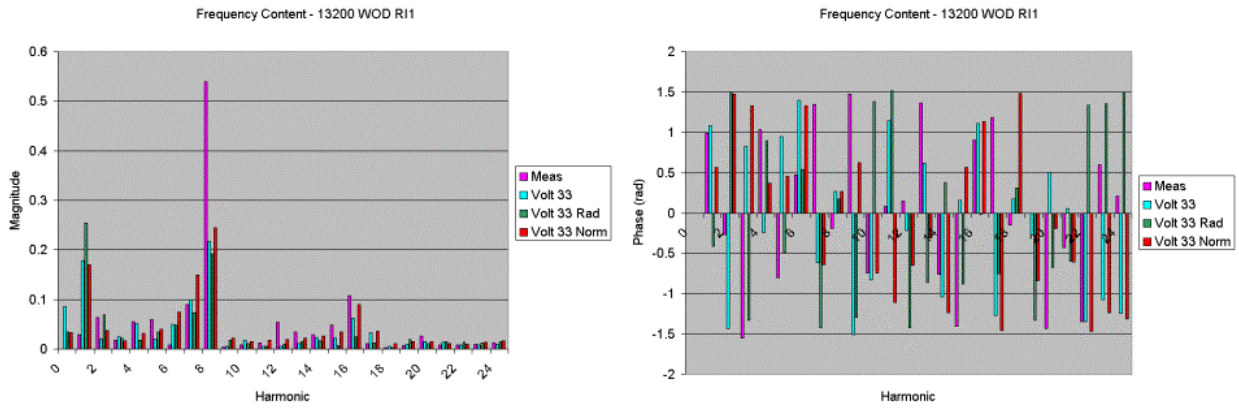

Figure 9.7. Frequency content of Volterra predictions of 13200 WOD RI1 R1.

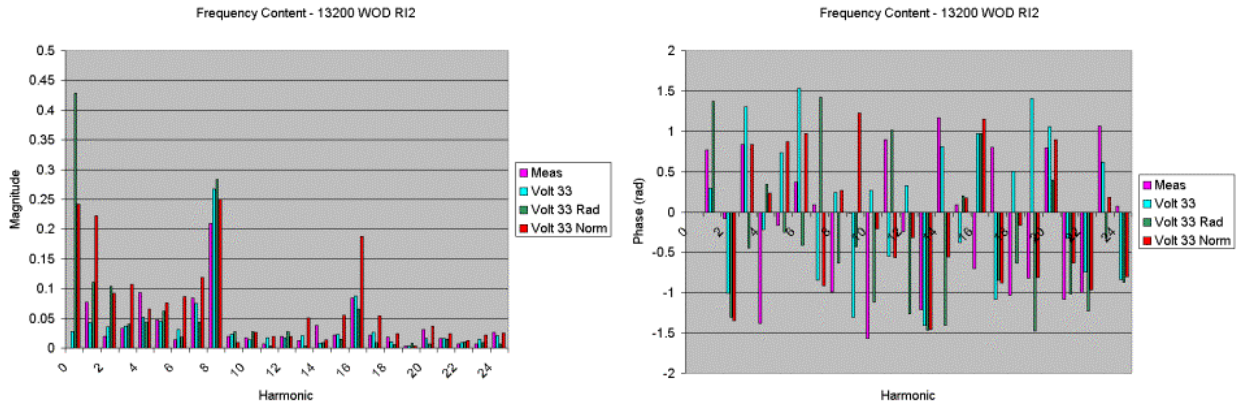

Figure 9.8. Frequency content of Volterra predictions of 13200 WOD RI2 R1.

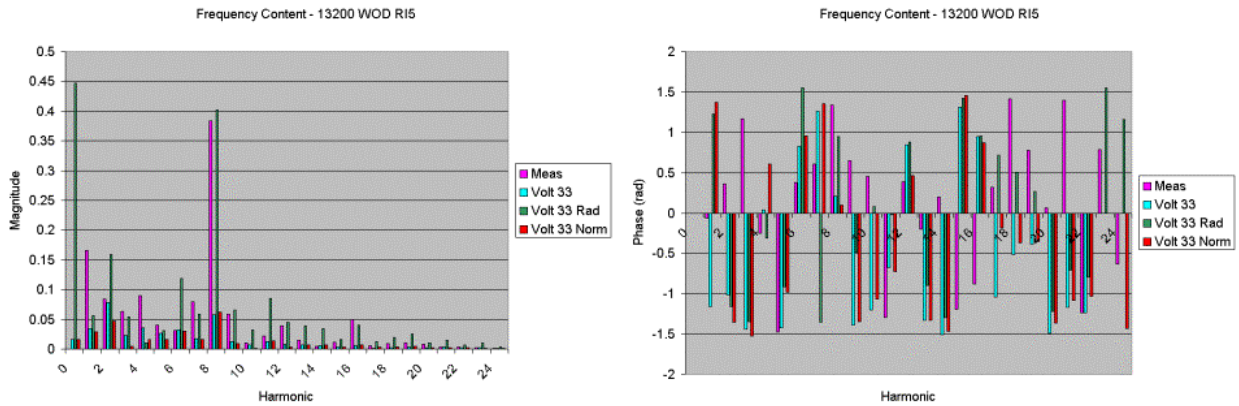

Figure 9.9. Frequency content of Volterra predictions of 13200 WOD RI5 R1.

Accuracy results for predictions made at 9500 PE and 13200 WOD are presented in Figure 9.10, Figure 9.11, Figure 9.12, and Figure 9.13. Tuned FRF prediction accuracies have been included as well for comparison. Recall that accuracy is defined as the ratio of measured to predicted frequency magnitude, with a perfect prediction having accuracy of 1.0. These results show that Volt 33 Norm has consistently made fairly accurate predictions at the near tip radial immersion, both as an average over the first 24 harmonics and at the dominant frequency. This form of normalized prediction has improved upon traditional Volt 33 predictions in nearly all cases. However, near hub normalized predictions are highly inaccurate. Radially trained Volterra predictions show the only signs of improved accuracy at the near hub radial immersion, as well as fairly accurate results at all remaining radial immersions. Radially trained predictions were seen to consistently be in phase with measured data, while the same was not always true for traditional and normalized Volterra predictions. Compared with tuned FRF predictions, the radially trained and normalized Volterra predictions show improved accuracy at the dominant frequency in nearly every case. As an average, the tuned FRF and enhanced Volterra predictions performed comparably, with enhanced Volterra predictions showing improved accuracy in most cases.

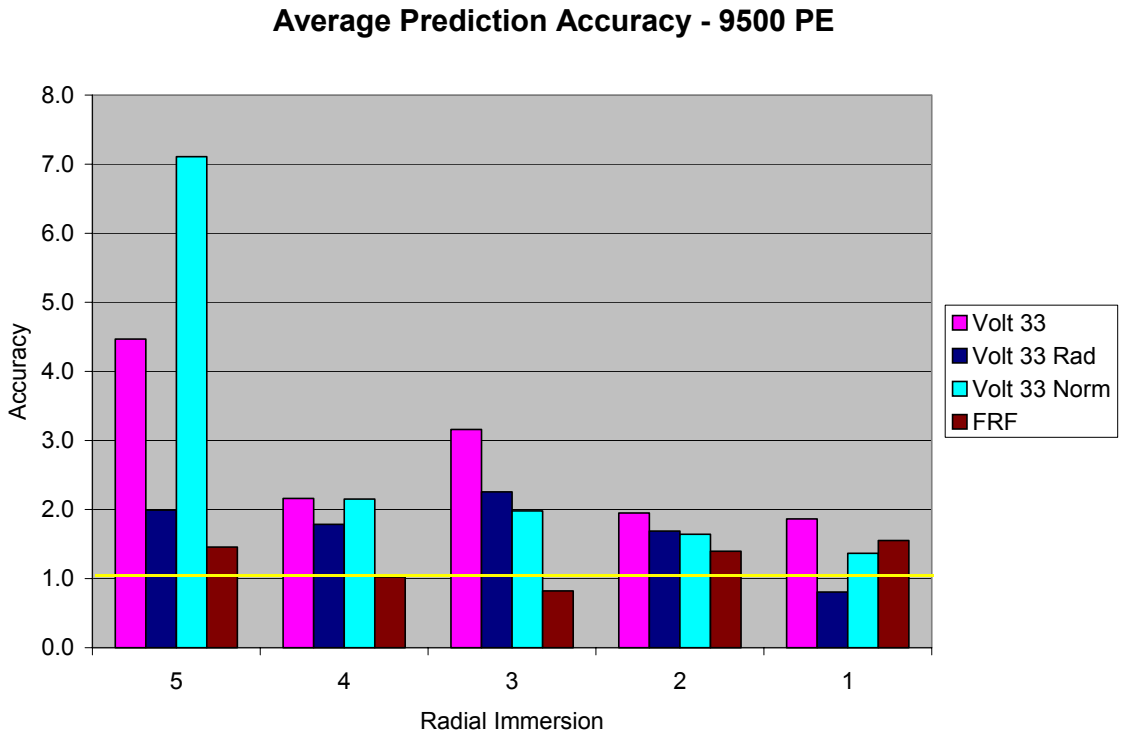

Figure 9.10. Average prediction accuracies over 24 harmonics of 9500 PE RI1-RI5.

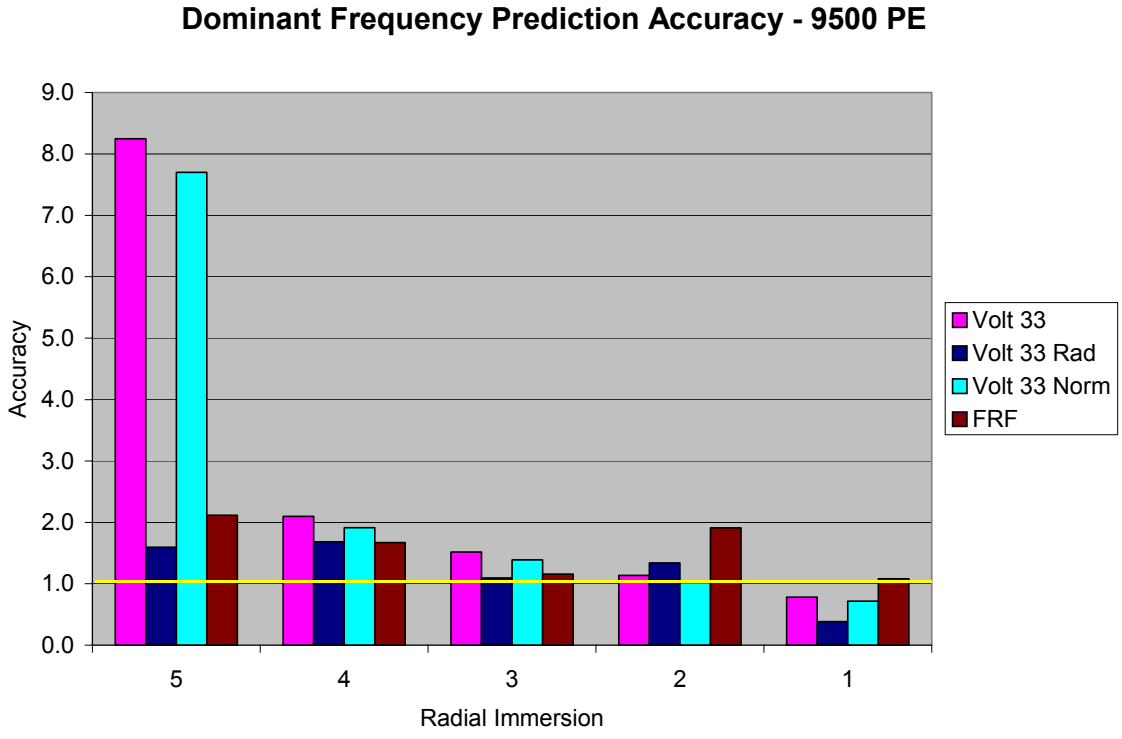

Figure 9.11. Dominant distortion frequency prediction accuracies of 9500 PE RI1-RI5.

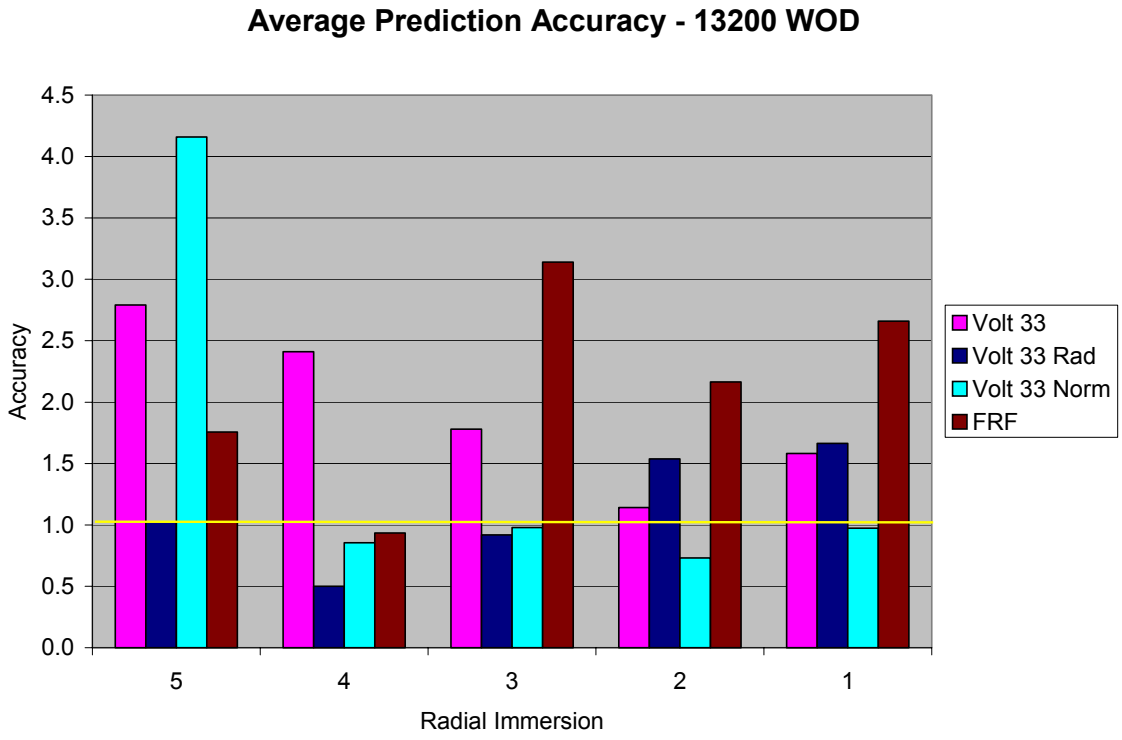

Figure 9.12. Average prediction accuracies over 24 harmonics of 13200 WOD RI1-RI5.

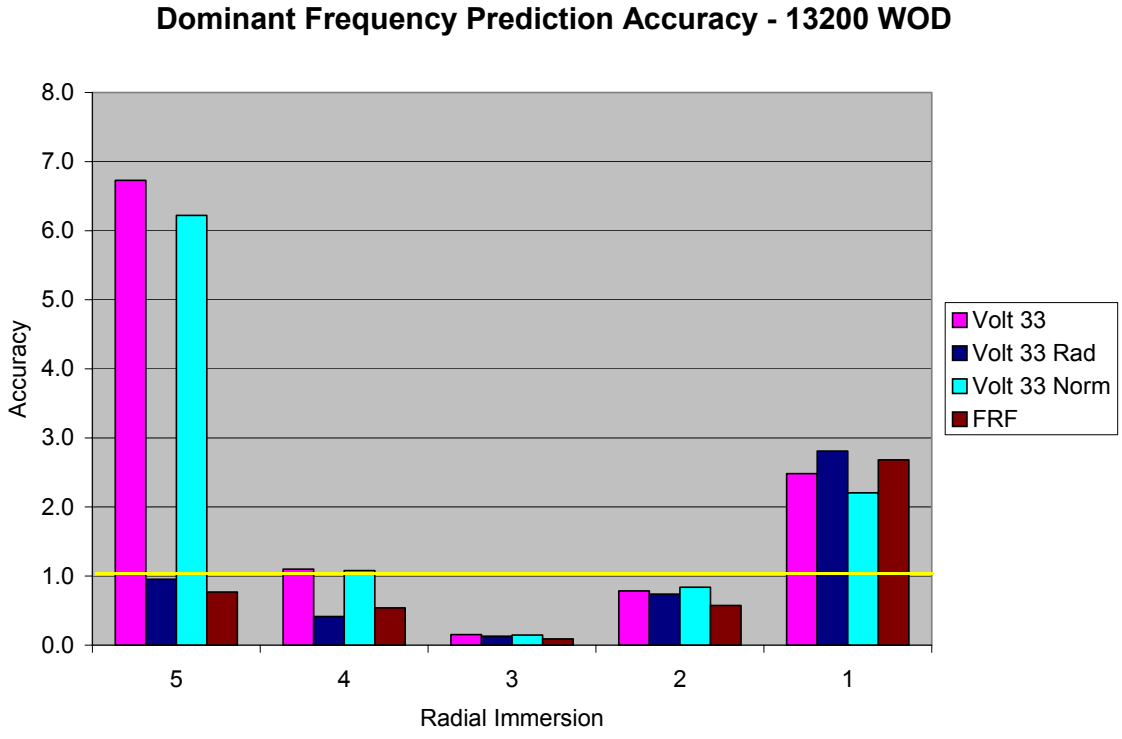

Figure 9.13. Dominant distortion frequency prediction accuracies of 13200 WOD RI1-RI5.

9.5 Conclusions Drawn from the Analysis of Radially Trained and Normalized Volterra Series Predictions

As seen in the time-series and frequency content comparisons of radially trained and normalized Volterra predictions, attempts to remove radial and speed distortion dependencies from predictions have been successful. Normalizing distortion data sets with non-dimensional, physics based parameters has shown signs of improvement over traditional Volterra series predictions. However, this improvement does not extend over the entire span of the rotor. Near hub normalized predictions show little improvement in capturing the dominant distortion frequency content in total pressure patterns. While the normalization parameter used in these comparisons does contain a radial term, the discrepancies in distortion intensity over the span of the rotor at high rotational speeds appear to be too vast for this to correct. The radially trained Volterra series has been shown to be the only Volterra predictor capable of capturing the dominant frequency component at this condition, while at the same time showing improvement over traditional Volterra series and tuned FRF predictions in many instances.

Returning to the IHPTET goal of predicting stresses anywhere along a blade to within 20% of measured stresses, it is fitting to perform a similar analysis on the total pressure predictions made along the blade. Since total pressure distortions are directly related to vibration induced blade stresses, this 20% goal presents a reasonable measure of grading each predictor's performance. Because dominant distortion frequencies signify the largest distortion magnitudes and are therefore the greatest source of possible HCF excitation, a comparison of percent error will be based on the predicted and measured dominant frequency magnitudes. Percent error is defined as

$$\%Error = \frac{\left(\Pr edicted - Measured\right)}{Measured} \times 100 .$$

Equation 9.7

Note that with error defined in this manner, a positive value indicates an over prediction while a negative value indicates an under prediction. Table 9.2 presents percent error results for all Stage 1 predictions. Tuned FRF results are included as well for means of

comparison. Recall that Volt 33 Rad and Volt 33 Norm predictions have not been applied to 9100 NOL data sets.

Table 9.2 Percent Error in Stage 1 Predictions of Dominant Frequency Magnitudes

9100 NOL		Volt 33	Volt 33 Rad	Volt 33 Norm	FRF
	RI5	-43.2%	NA	NA	288.4%
	RI4	-21.8%	NA	NA	204.9%
	RI3	-35.0%	NA	NA	79.4%
	RI2	-22.6%	NA	NA	58.0%
	RI1	1.4%	NA	NA	38.8%

9500 PE		Volt 33	Volt 33 Rad	Volt 33 Norm	FRF
	RI5	-87.9%	-37.2%	-87.0%	-52.7%
	RI4	-52.4%	-40.6%	-47.8%	-40.1%
	RI3	-34.2%	-8.7%	-28.0%	-13.6%
	RI2	-12.0%	-25.3%	-1.9%	-47.6%
	RI1	27.6%	161.0%	39.4%	-7.6%

13200 WOD		Volt 33	Volt 33 Rad	Volt 33 Norm	FRF
	RI5	-85.1%	4.8%	-83.9%	30.1%
	RI4	-9.1%	141.8%	-7.3%	85.7%
	RI3	561.6%	679.9%	587.4%	1016.7%
	RI2	27.0%	35.1%	19.0%	74.1%
	RI1	-59.7%	-64.4%	-54.7%	-62.8%

		Volt 33	Volt 33 Rad	Volt 33 Norm	FRF
(RI5 Included)	Average %error	37.1%	57.7%	41.0%	77.4%
	Std Dev	26.3%	56.2%	30.6%	77.0%
(RI5 Excluded)	Average %error	27.5%	68.1%	28.3%	64.8%
	Std Dev	17.5%	59.6%	20.1%	52.8%

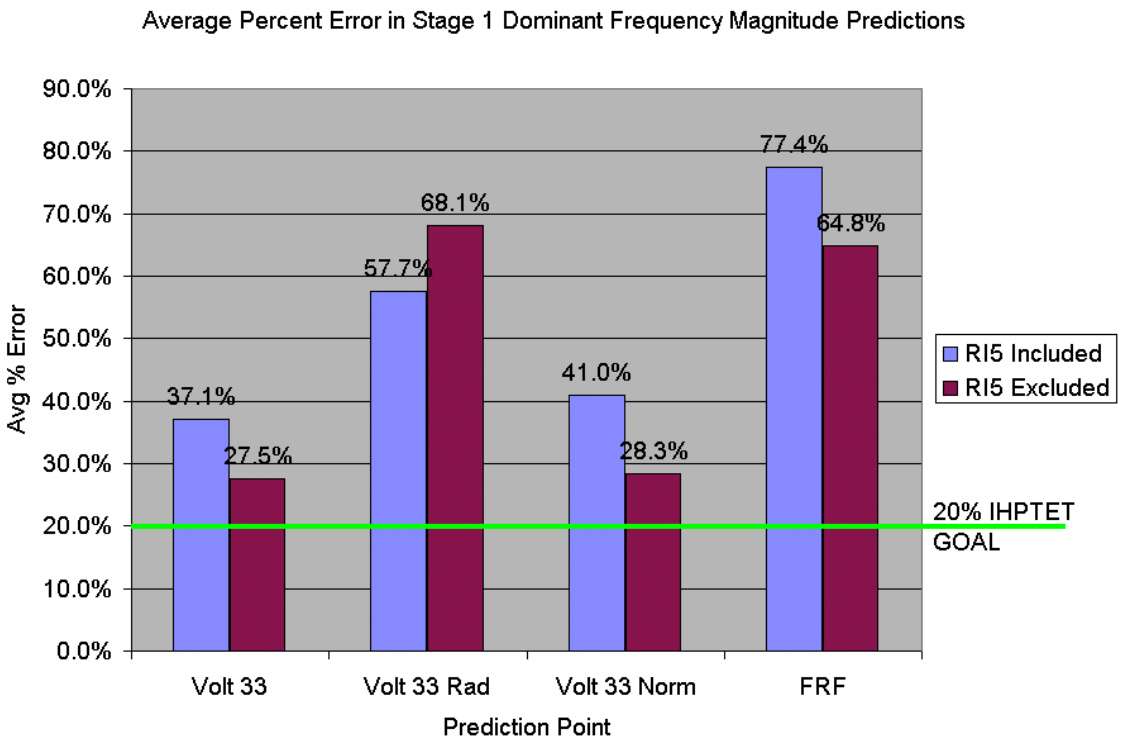

Figure 9.14. Average percent error in Stage 1 dominant distortion frequency magnitude predictions.

Table 9.2 includes a statistical analysis of the average percent error over operating points for each predictor. These statistics have been computed with near hub (RI5) predictions both included and excluded. The reason for doing so is that RI5 predictions tend to be extreme outliers for Volt 33, Volt 33 Norm and FRF predictions, skewing the average values considerably. Note that average values are calculated with prediction results at 13200 WOD RI3 excluded, as these points are not representative of typical prediction performance for any model. Average percent error values are seen to drop significantly when RI5 predictions are excluded from calculations. All Volterra series predictions are seen to outperform the tuned FRF prediction method. It is apparent from these results that Volt 33 and Volt 33 Norm predictions provide the best dominant frequency magnitude predictions, both averaging less than 30% error. While these predictions do not meet the 20% error goal as related to the IHPTET goal, they set the stage for the possibilities of successfully using nonlinear Volterra theory in the prediction of total pressure distortion propagation. As will be pointed out in Chapter 13, there is

room for improvement in the Volterra series model. Recall that in Section 7.3 a baseline error of the current modeling method was established, which may be attributed to higher-order system influence that has not been included in this study. Therefore a possibility exists of improved prediction accuracy with the inclusion of higher-order effects. Further experimental testing and system analysis is required to validate this possibility. Also, with experimental data collection tailored to training Volterra kernels, strong evidence leading to the improvement of these percent error results exists.

As seen in Stage 1 prediction results presented throughout this chapter, the normalized 3rd order Volterra series model appears to be the predominant predictor. Although the traditional Volterra series has shown slightly better percent error results in Table 9.2, the normalized predictions have been shown to improve on the overall prediction accuracy and particularly the phase content of the traditional Volterra series at high-speed conditions.

10 Quality and Potential of Distortion Magnitude Predictions

10.1 Quality and Potential Index

The research community has adopted several indices for assessing the potential effects of total pressure distortions on compressor and turbine engine performance. One such index proposed by Danforth (1975) has previously been discussed in Section 2.2. Danforth introduced the Distortion Excitation Index for Vibration (DEIV) as a means of assessing a distortion's potential for aeromechanical effects and providing an early warning design alert to potential vibratory problems. An analogous index has been implemented for the present study, which assesses both the capability of a model to predict downstream distortion profiles and the potential of these distortions for blade excitation at a particular blade location and operating condition. In essence, this index differentiates between operating conditions in which excitation potential is high and highly accurate distortion magnitude prediction is imperative, and those in which there is minimal chance of blade excitation and prediction accuracy is not as pertinent. The usefulness of this index can be realized when validating the performance of the Volterra series in predictions presented earlier in this study. While the results of this investigation have shown prediction cases where accuracy of the Volterra series has diminished (i.e. high speed, near hub conditions), this index will evaluate the importance of highly accurate predictions at these conditions, based on their potential as HCF drivers.

The present distortion index is based on a concept of "quality" and "potential" of distortion magnitude predictions. By definition of these terms, it will be shown that the first is a function of the second. The potential of a prediction represents the potential of the known distortion magnitude downstream of the rotor to excite blade vibratory modes at a particular frequency of interest. Generally this frequency will be either the dominant frequency of the distortion pattern, or a frequency at or near a known natural frequency of the blade. It is beneficial to normalize the known distortion magnitude, which is a dynamic pressure term, by a pressure coefficient in order to account for variations in operating conditions. The potential of a distortion prediction is then defined as

$$Potential = \frac{MeasuredDistortionMagnitude}{\frac{1}{2}\rho U_{tip}^2}$$

Equation 10.1

where ρ is the density entering the rotor and U_{tip} is the tip blade rotational velocity. Inspection of the denominator of this term reveals the pressure coefficient to have units of pressure, and potential therefore dimensionless.

While the potential of a distortion has been shown to be a function of the actual distortion magnitude at the operating condition of interest, the quality of a distortion prediction is in addition based on the accuracy of the prediction. Accuracy has previously been defined as the ratio of measured to predicted distortion magnitude with desired accuracies near 1.0. While this definition of accuracy is on a descending scale, it is beneficial to adjust the accuracy to an ascending scale accordingly with an ascending potential scale. To achieve this, a range of adjusted accuracy from 1.0 to 8.0 has arbitrarily been chosen, in which 8.0 represents a perfect magnitude prediction and 1.0 a very poor prediction. This is accomplished by relating adjusted accuracy to accuracy through the relations

$$AdjAcc = \left(-\frac{8}{7}\right) * Acc + \frac{64}{7}, Acc \geq 1$$
$$AdjAcc = \left(-\frac{8}{7}\right) * (2 - Acc) + \frac{64}{7}, Acc < 1$$

Equation 10.2

With adjusted accuracy defined above, the quality of a distortion magnitude prediction can then be defined as,

$$Quality = (AdjustedAccuracy) * (Potential).$$

Equation 10.3

The quality of a distortion prediction encompasses both the accuracy of the prediction and the relative importance of predicting with high accuracy. Through the definition of terms shown previously, it is seen that a high value of quality can indicate one of two things; either a distortion magnitude with moderate potential has been predicted very accurately, or a distortion magnitude with very high potential has been predicted with modest accuracy. Therefore it is necessary when presenting quality results to identify which component of the product is driving the result. In order to accomplish this, all quality results are presented simultaneously with potentials and adjusted accuracies. When analyzing a plot of prediction quality, first take notice of the potential at the radial immersion of interest. If the potential is particularly low, there is minimal concern for blade excitation at this frequency and operating condition and no further analysis is needed. However, if potential is high further examination is required. Next note the quality of this prediction. If the quality is also high, the distortion magnitude has been predicted with high accuracy and a high level of confidence is implied in this prediction. However, if the quality is low the prediction accuracy must also be low. This indicates the need for further prediction enhancement at this particular case, as there is a high potential for blade excitation, which the model has not captured.

10.2 Quality and Potential of Normalized Volterra Stage 1 Predictions

Because the normalized, 3rd order Volterra series has been chosen as the predominant modeling technique in this study, quality and potential results have been tabulated for these predictions. Both values are calculated at the dominant distortion frequency of the prediction's operating condition.

Quality and potential are now presented for Volt 33 Norm predictions along each speed line. Indices of 9100 NOL predictions at the 3rd harmonic are shown in Figure 10.1. Note that radial immersion quality and adjusted accuracy are presented on a single axis, while potential is presented on a separate axis. At this operating condition prediction quality is seen to be fairly constant across the rotor span, with a drop off at the near tip prediction. It can be seen that this drop in quality is driven by a decrease in potential. If

the proper data were available, the distortion potential at each radial immersion could be compared with distortion magnitudes known to produce high levels of vibration at this frequency for this particular rotor. However, in comparison to potentials observed along the remaining speed lines, the potentials seen at 9100 NOL are moderate. With high prediction accuracy and moderate potential, quality results at 9100 NOL provide high confidence in Volterra prediction capabilities at these conditions.

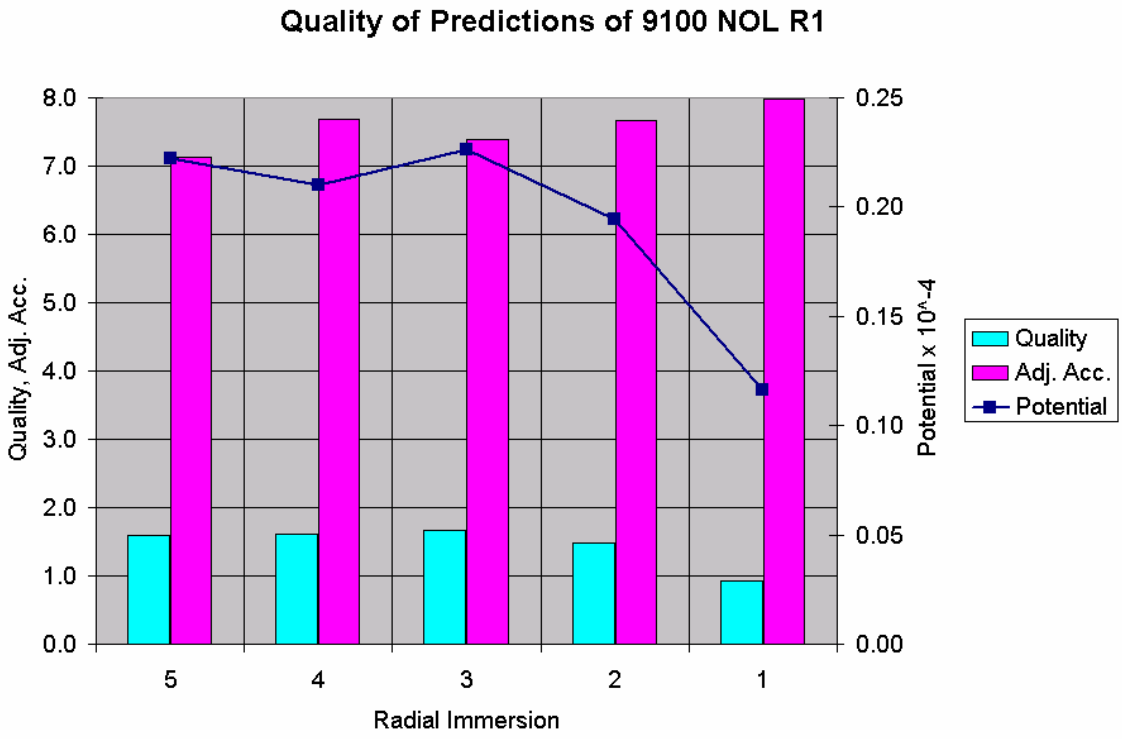

Figure 10.1. Quality and potential of Volt 33 Norm predictions at the 3rd harmonic of 9100 NOL R1.

Quality and potential of Volt 33 Norm predictions at the 8th harmonic of 9500 PE are now presented in Figure 10.2. Note that the potential of distortion magnitudes at this condition are somewhat lower than those seen at 9100 NOL. However, the potential at 9500 PE indicates distortion magnitudes at a frequency different than those at 9100 NOL, so a direct comparison is not appropriate. Note in Figure 10.2 that the quality of prediction at RI5 is very low compared to the rest of the span. This reflects the poor prediction accuracy coupled with a low potential at this position. This should sound an

alarm to the investigator that further analysis at this condition is warranted due to potentials similar to the remainder of the span at this condition. Again the near tip prediction quality is seen to drop off as compared to much of the rest of the span, and is again driven by a lower potential. The mid-span prediction qualities, RI2 through RI4, indicate high accuracy predictions of distortions with moderate potential. Therefore, a legitimate conclusion to draw from this plot would be that predictions at conditions near 9500 PE could be made with high confidence along RI1 through RI4, with a greater emphasis placed on RI2-RI4 due to higher potentials.

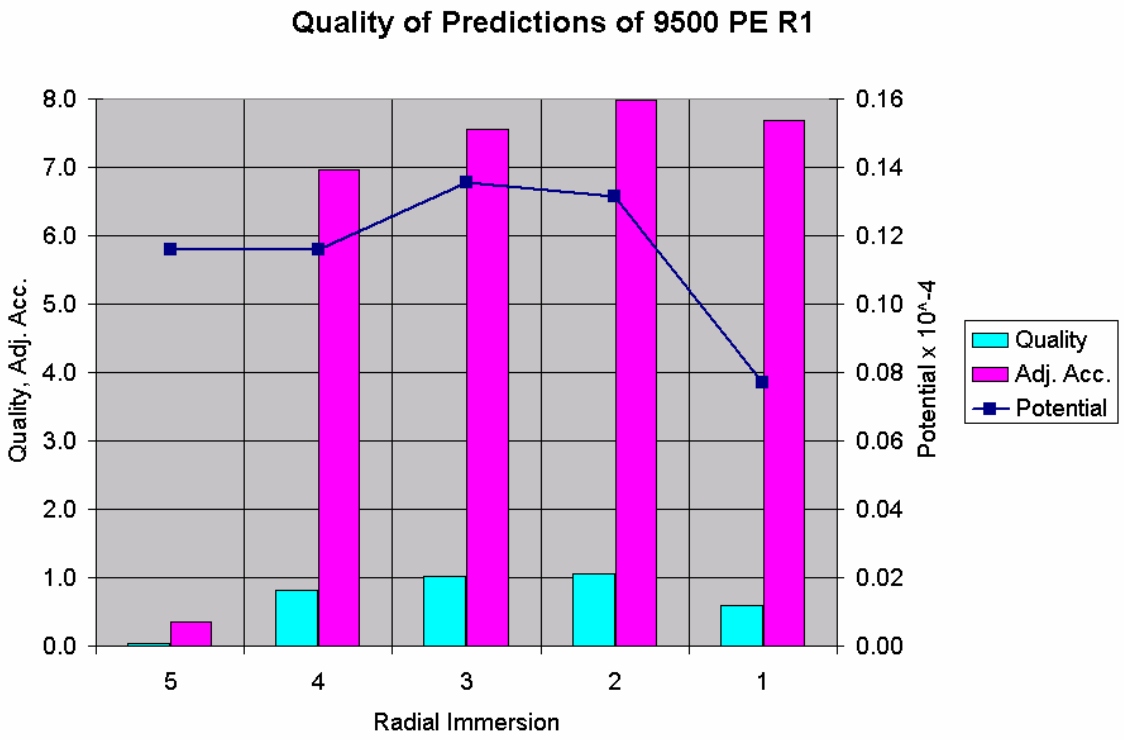

Figure 10.2. Quality and potential of Volt 33 Norm predictions at the 8th harmonic of 9500 PE R1.

Now focusing on 13200 WOD predictions, quality and potential at this condition are presented in Figure 10.3. High-level potentials exist at this condition, indicating a greater need for highly accurate predictions. RI3 has very low potential and predictions at this position are therefore not viewed with the same degree of concern as the remainder of the span. RI5 shows a moderate potential and a relatively low quality, indicating the

need for further analysis at this condition as the investigator's confidence in this prediction is not very high. Both RI4 and RI2 have moderate potentials along with high quality. These conditions then represent distortion magnitudes of relative significance that have been predicted very accurately. The investigator can feel confidant in the ability of this model at these conditions. Similarly, the potential of RI1 is very high indicating the importance of accurately predicting the distortion magnitude at this position. High prediction quality at this condition indicates that high accuracy has been achieved, and the investigator can feel confident in the predictions made at this position.

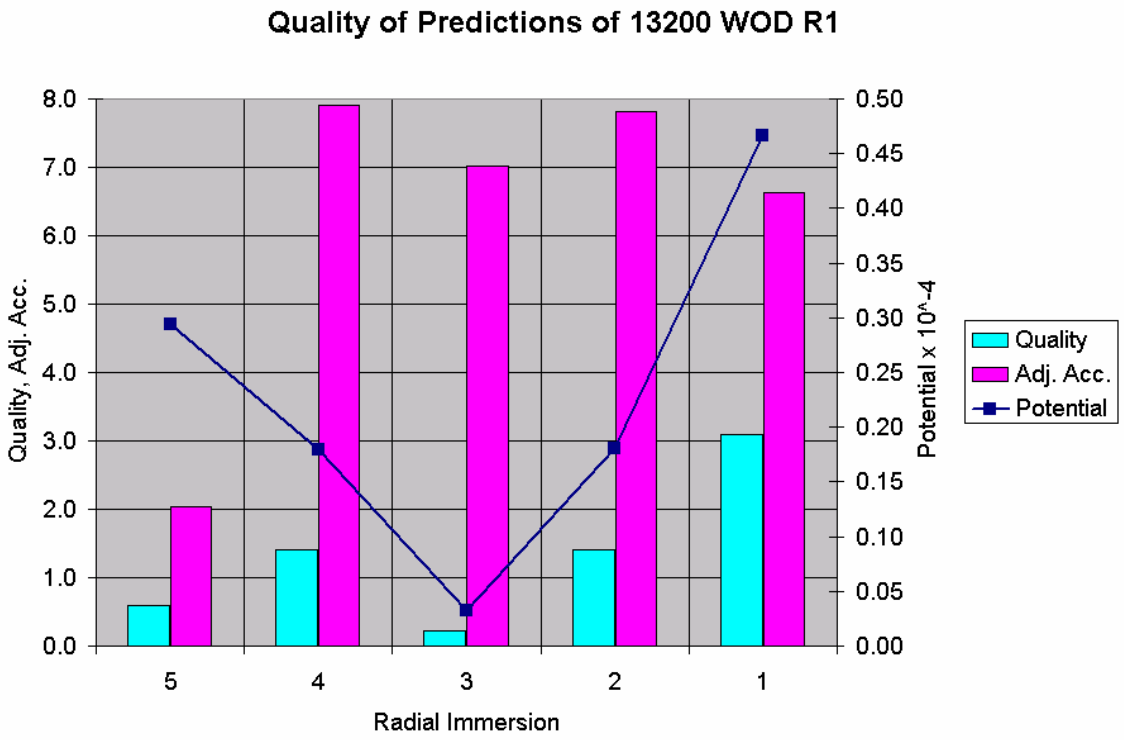

Figure 10.3. Quality and potential of Volt 33 Norm predictions at the 8th harmonic of 13200 WOD R1.

These examples have illustrated the possibility of applying the quality and distortion indices to Volterra predictions of downstream total pressure distortion magnitudes. The indices allow the investigator to put prediction results into context, determining whether the model is predicting with high accuracy when it is most needed. High levels of quality and potential give the investigator confidence in the fact that the

model is providing highly accurate predictions under conditions where the potential of HCF excitation is high and there is little room for error.

11 Volterra Predictions of 2nd Stage and Alternate Rotor Distortion Patterns

11.1 2nd Stage Volterra Predictions

As a further test of the Volterra series, prediction techniques developed in previous chapters will now be applied to 2nd stage distortion data. As seen in Figure 11.1, Stator 1 leading edge total pressure data will be considered as 2nd stage input data with Stator 2 leading edge data treated as Rotor 2 exit data. Stator 1 leading edge data is assumed to be consistent with flow properties at Rotor 2 leading edge as no work is done on the fluid as it flows through the stationary stator blade row. Each of the Volterra prediction forms, traditional, radially trained, and normalized will be applied to these data sets.

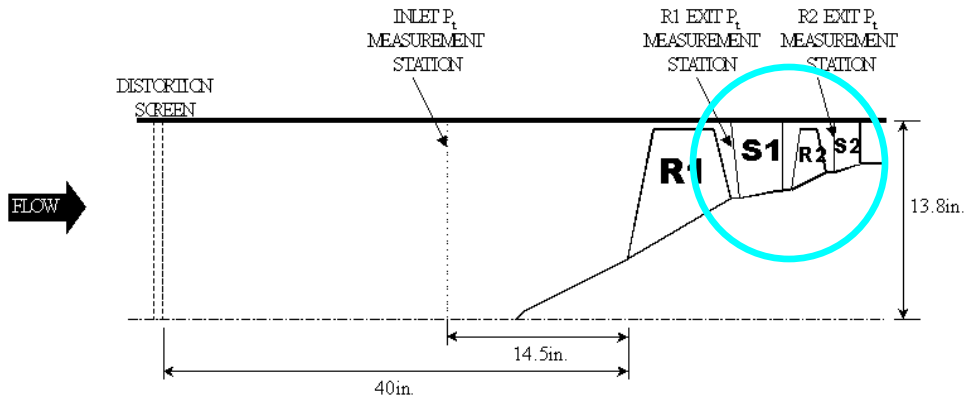

Figure 11.1. 2nd stage input/output measurement locations [Small, 2001].

Stage two 3rd order Volterra series prediction results are provided for the 9100 NOL RI1-RI5 R2 data set. Prediction results in the 2nd stage rotor at this condition are similar to those found in the 1st stage, and as such radially trained and normalized Volterra predictions will not be investigated for this data set. As seen in the time-series comparisons of 3rd order Volterra predictions and measured data shown in Figure 11.2, Volt 33 has closely matched the measured distortion waveform at each radial immersion. With the exception of the near tip (RI1) prediction, Volt 33 has nearly overlaid the

distortion peaks in each case. Accuracy results for these predictions are provided in Figure 11.3 and Figure 11.4. Here it is seen that prediction accuracies are extremely good at this condition, with slight deviation only at the near tip (RI1) prediction. The 3rd order Volterra series appears to have continued success as a predictor of low speed, total pressure distortion propagation in the 2nd stage of this compressor.

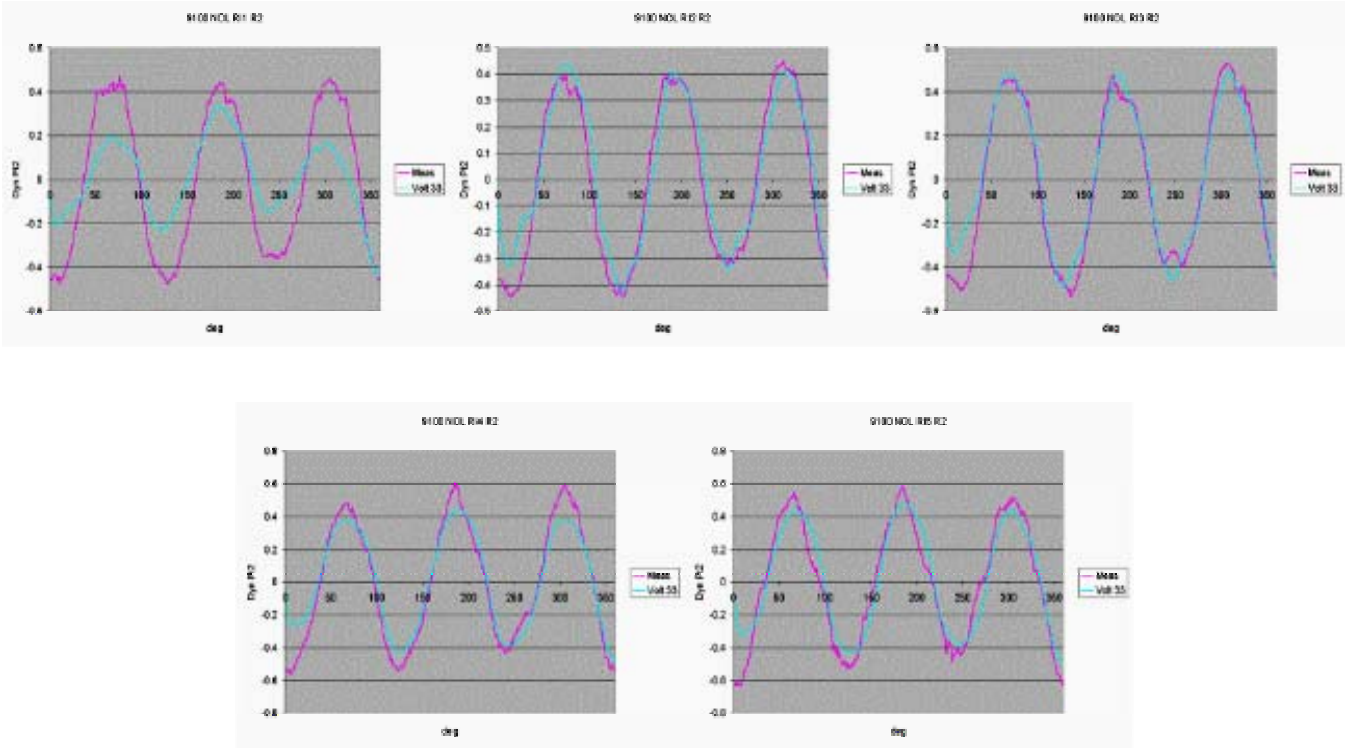

Figure 11.2. Time-series comparison of 3rd order Volterra predictions of 9100 NOL RI1-RI5 R2.

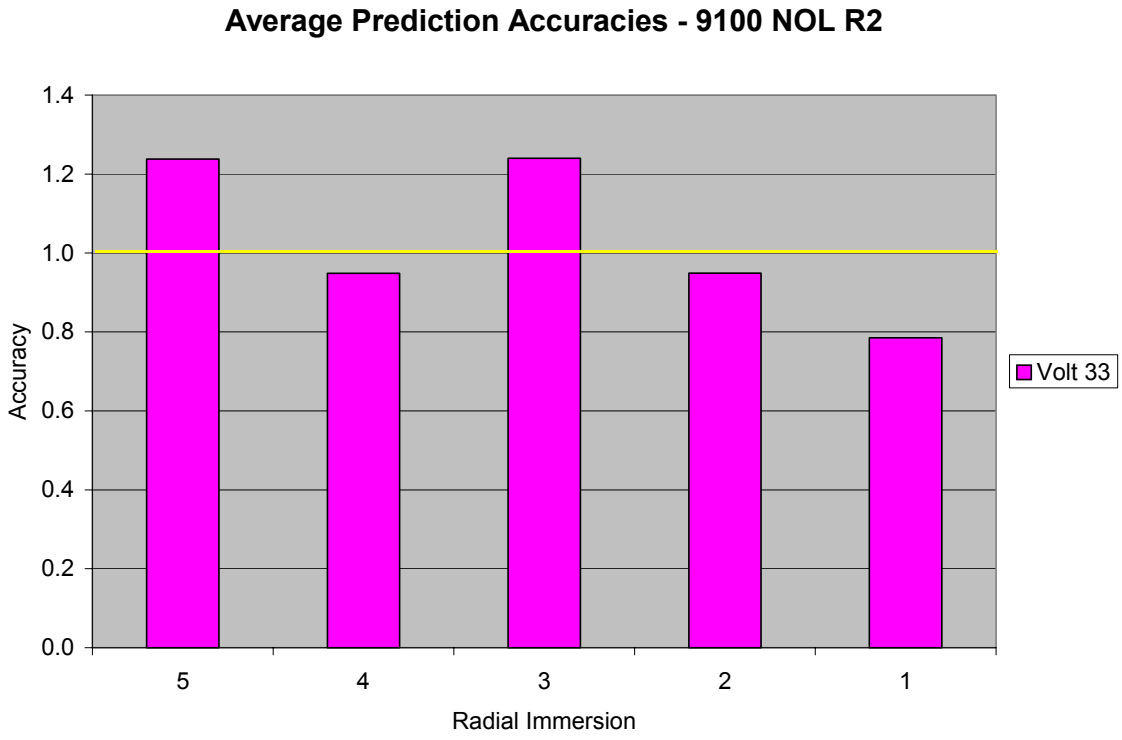

Figure 11.3. Average prediction accuracies over 24 harmonics of 9100 NOL RI1-RI5 R2.

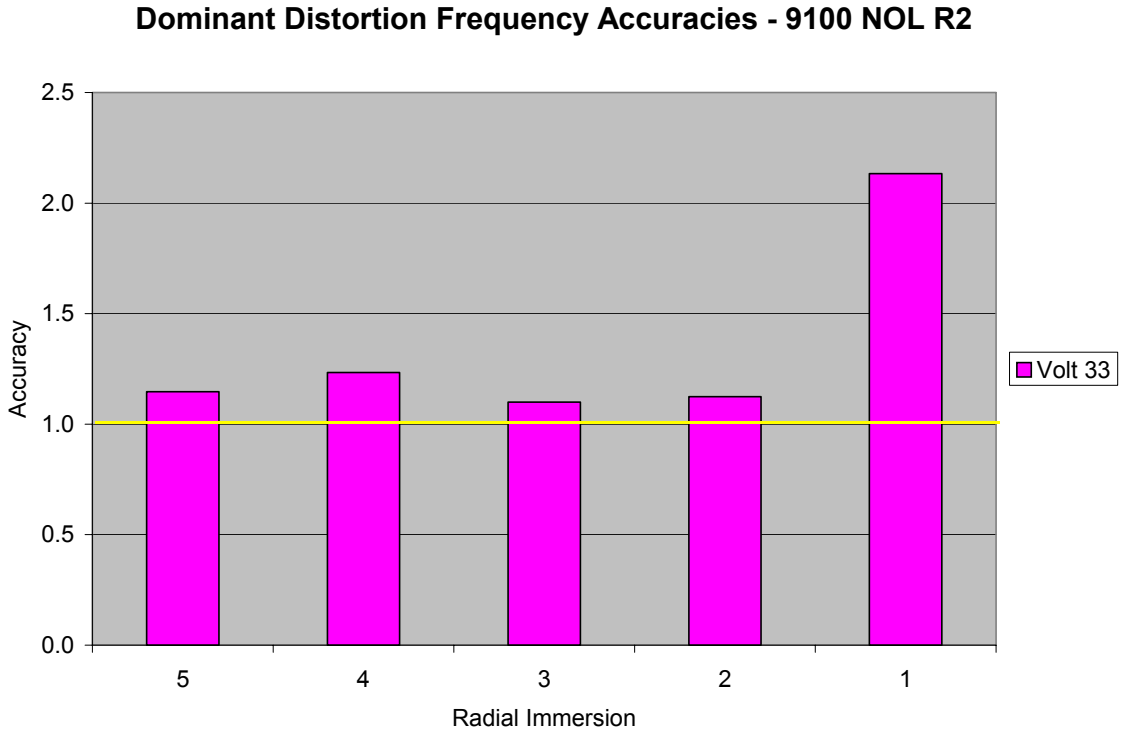

Figure 11.4. Dominant distortion frequency accuracies of 9100 NOL RI1-RI5 R2.

Stage 2 prediction results are also provided for traditional, radially trained, and normalized Volterra predictions of 9500 PE RI1-RI5 R2. Results at this condition are similar to those found at 13200 WOD RI1-RI5 R2 and can be taken as representative of their prediction accuracy. Time-series comparisons of Volterra predictions are shown in Figure 11.5. Predictions at this condition do not appear to have captured distortion patterns as well as those at 9100 NOL R2. Volt 33 shows reasonable predictions over the span of the rotor, including near hub (RI5) predictions. This result is interesting, considering the inability of this predictor to recreate the near hub distortion waveforms downstream of Rotor 1. This implies that 2nd stage total pressure distortion patterns do not share the radial dependence typical of high-speed, 1st stage distortions. This is not surprising considering the radially uniform distortion patterns exiting Rotor 1.

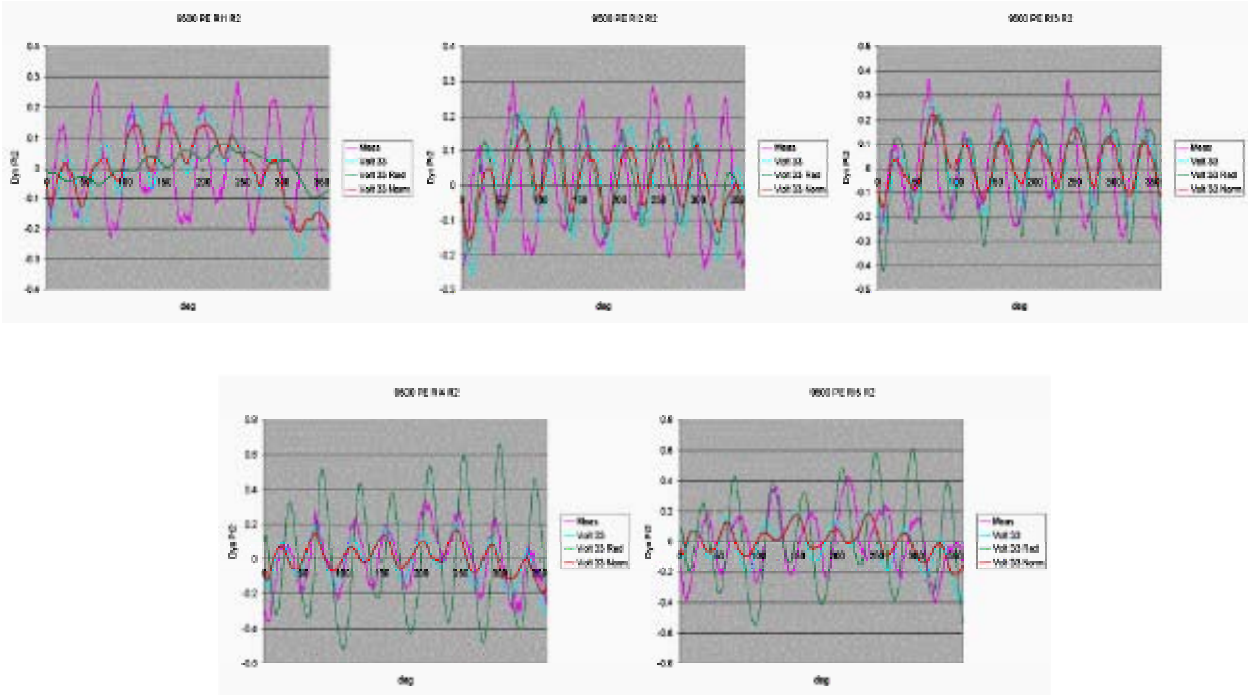

Figure 11.5. Time-series comparison of Volterra predictions of 9500 PE RI1-RI5 R2.

Accuracy results of Volterra predictions are provided in Figure 11.6 and Figure 11.7. Volt 33 is seen to provide the most consistent accuracy over the span of the rotor, both as an average over the first 24 harmonics and at the dominant distortion frequency. The performances of radially trained and normalized Volterra predictions, however, are not as

consistent over the rotor span. The radially trained Volterra series is seen to predict with high-quality accuracy over much of the rotor span, however predicts with poor accuracies at near tip conditions. Meanwhile, the normalized Volterra series appears to provide little improvement upon the traditional Volterra series predictions. Because of this result, the alternative normalized Volterra prediction methods developed in the previous chapter and shown to be successful in improving 1st stage distortion predictions, does not appear to apply to 2nd stage distortion propagation. This result is not surprising, as rotor characteristics and flow behavior vary greatly between stages. As a result, a separate set of normalizing characteristics would need to be investigated for 2nd stage predictions.

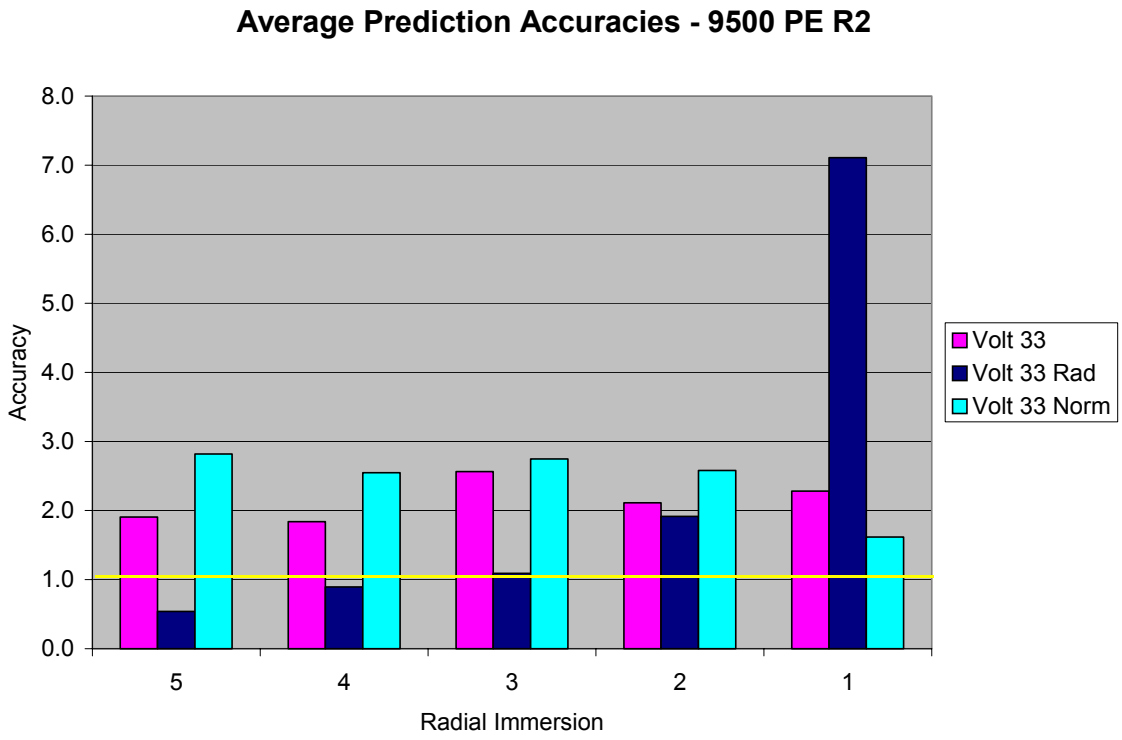

Figure 11.6. Average prediction accuracies over 24 harmonics of 9500 PE RI1-RI5 R2.

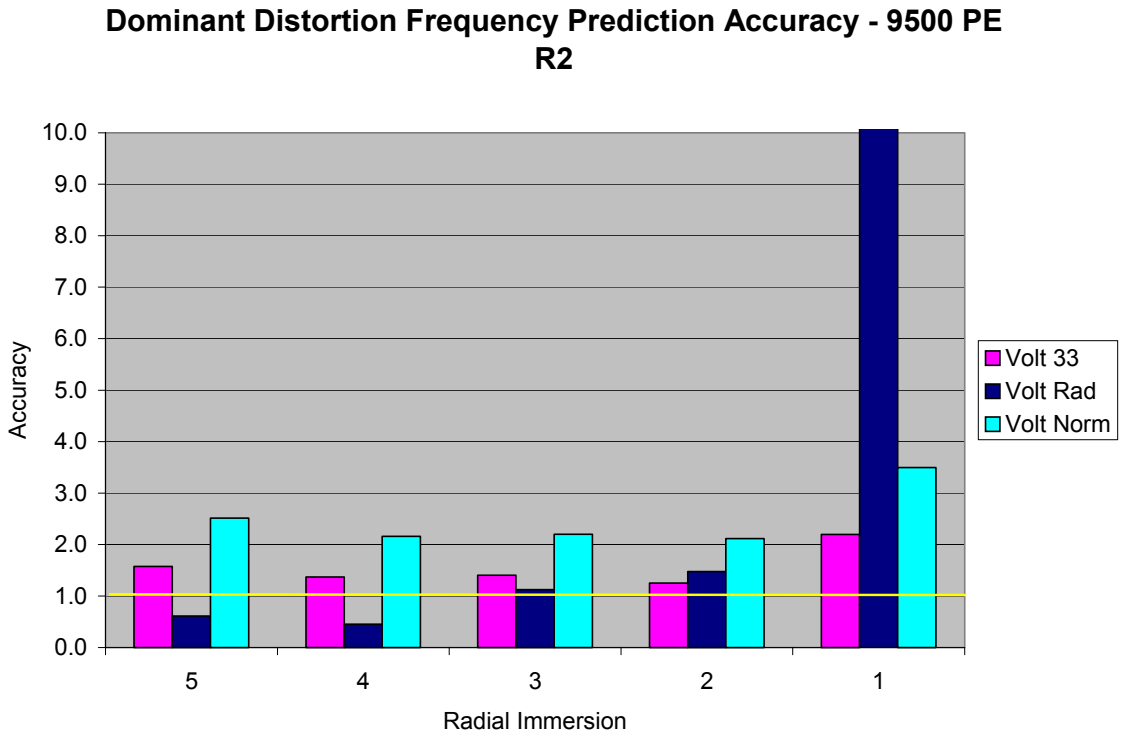

Figure 11.7. Dominant distortion frequency prediction accuracies of 9500 PE RI1-RI5 R2.

11.2 Volterra Predictions of an Alternate Rotor

The Volterra model of total pressure distortion propagation derived from Stage 1 data has been tested on a new rotor of different design. This is a low aspect ratio rotor of similar blisk wide-chord design, but incorporates different blade geometry [Small, 2001]. Testing of the rotor took place in the same test cell as the previously examined rotor, providing some degree of consistency. Additional information characteristic of this rotor is proprietary and therefore will not be included in this study.

Although it has already been established that the expectations of a Volterra model based on one rotor to accurately predict distortion propagation through another are not high, this test nonetheless serves two distinct purposes. The first purpose is to test the ability of the Volterra series to capture the basic fundamental behavior of a compressor rotor. Successfully applying the model to a rotor of different design will prove the model's ability to act in general as a compressor stage. The second purpose of this test is

to subject the Volterra series to a novel inlet distortion type. A typical inlet distortion profile generated for testing of the alternate rotor is shown in Figure 11.8. Notice that this is a 1 per rev square wave. With 3 per rev and 8 per rev sinusoidal distortion waveforms used to train the Volterra kernels, this is a distortion type unknown to the model, and therefore provides a test of the model's ability to recognize and reproduce a novel waveform. Predictions of downstream total pressure distortion patterns of the alternate rotor are restricted to the traditional, 3rd order Volterra series trained with 1st stage distortion data. Additional flow data necessary to apply radial and normalized predictions is not available.

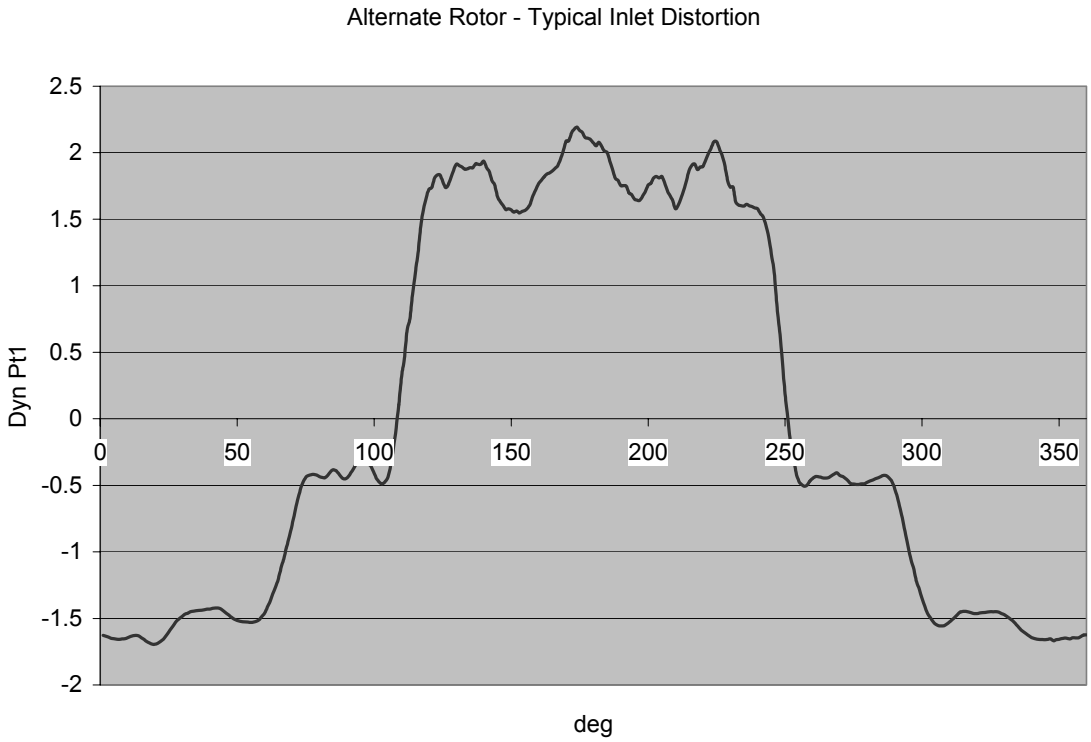

Figure 11.8. Typical inlet dynamic distortion profile used in testing of alternate rotor.

A qualitative analysis of Volterra predictions of alternate rotor distortion patterns will now be provided. Time-series comparisons of Volterra predictions and measured data are shown in Figure 11.9. It is seen here that the Volterra series has successfully recognized and recreated the novel 1 per rev distortion pattern characteristic of this data

set. Although this rotor is different from that on which the model has been created, the Volterra series has done well at predicting the downstream distortion waveform.

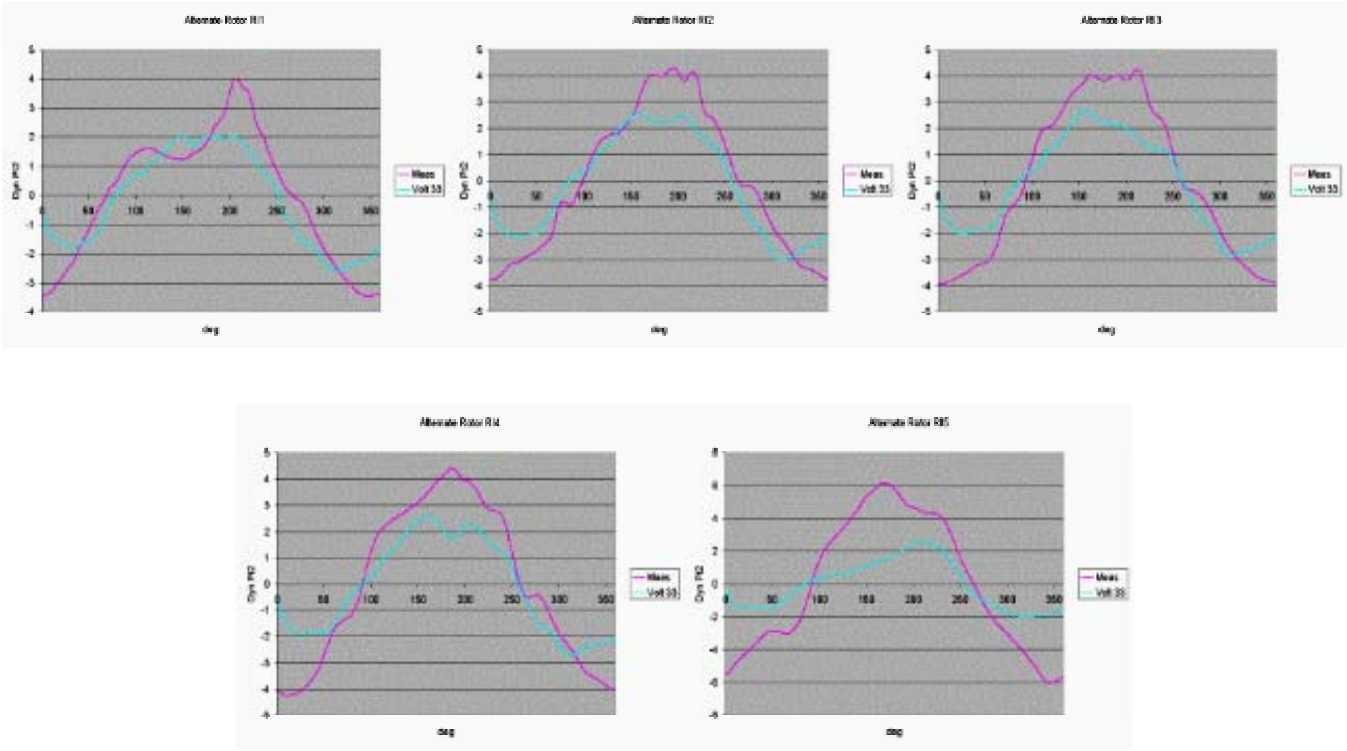

Figure 11.9. Time-series comparison of 3rd order Volterra predictions of alternate rotor.

12 Summary and Conclusions

The propagation of circumferentially non-uniform total pressure patterns through a transonic, axial flow compressor has been investigated in this study. Nonlinear Volterra theory has been successfully demonstrated as an empirical predictor of downstream total pressure distortion patterns.

Volterra kernels are the basis of a Volterra series, allowing prediction of system response given any arbitrary input. As such an empirical method of extracting Volterra kernels from existing input/response total pressure data sets has been presented and applied to a transonic rotor. A progression of results through 1st order, 2nd order, and 3rd order Volterra predictions has shown enhanced prediction accuracy with the addition of nonlinear terms, and has therefore illustrated the significant influence of non-linearity in distortion transport through the rotor. Further attempts to improve Volterra predictions have been illustrated, including training Volterra kernels along individual streamlines in order to remove the radial dependence of distortion intensity, and normalizing total pressure data sets by physics based parameters representative of compressor characteristics, again removing distortion dependencies. Low speed (9100 rpm) distortion patterns have shown minimal susceptibility to these dependencies and are adequately predicted by a traditional 3rd order Volterra series.

Higher-order, nonlinear terms were seen to have a significant influence on high-speed Volterra predictions. Low speed conditions, however, have shown little response to 2nd and 3rd order terms, while being predicted with high accuracy based solely on the 1st order term.

Nonlinear Volterra models have been successfully applied to data sets characteristic of operating conditions other than those at which the models were derived. This is an important result pointing to the possibilities of successfully predicting downstream distortion patterns of inlet conditions either not included in test schedules or unable to be replicated by modern distortion generating practices.

A common result of Volterra predictions at high-speed conditions was seen to be an inability to produce any significant response at near hub conditions, particularly at RI5. The cause of this was shown to be a strong distortion dependence on radial position and

rotational speed. These dependencies led to the development of the enhanced prediction methods discussed earlier. Training Volterra kernels along individual streamlines was found to greatly improve upon near hub predictions. Normalized predictions, while improving upon near tip and midspan prediction accuracy, were seen to have little influence on near hub predictions.

Volterra series prediction results were shown to have improved upon Small's tuned FRF model. Significant improvement in frequency content prediction was found at low speed (9100 rpm) conditions. Traditional Volterra predictions at high-speed conditions were seen to lack in frequency content accuracy when compared with the tuned FRF model. However, significant improvements in frequency magnitude and phase matching were found when predictions were corrected with either radially trained kernels or normalized data sets. One capability of the Volterra series not realized by the tuned FRF model is the ability to recreate higher-order time-series distortion content at high-speed conditions. This distortion content is most evident in the downstream total pressure profile of 13200 WOD RI2 R1. The distortion detail was shown to be a result of the 2nd and 3rd order terms of the Volterra series, and therefore is considered as a nonlinear result of distortion transport. The fact that the Volterra series was able to produce the distortion detail of an operating condition not included in the training of its kernels speaks highly of the strong capabilities and possible applications of this theory.

When the Volterra series was applied to the 2nd stage rotor, distortion propagation was seen to exhibit different properties than those found in the 1st stage rotor. The most notable property was an apparent lack of the high-speed radial dependence dominant in the 1st stage rotor. Near hub prediction accuracy in the 2nd stage was superior to that in the 1st stage. As a result of these findings, the prediction technique of radially trained kernels did not have the positive effect in the 2nd stage that it did in the 1st stage. Likewise, normalized predictions in the 2nd stage were not as effective as those in the 1st stage. This leads to the conclusion that the dominant flow properties in distortion propagation vary from stage to stage.

Finally, a Volterra series trained with 1st stage data was successfully applied to an alternate rotor of different design operating with a new distortion pattern. Here, a 1 per rev distortion pattern was used in testing of the rotor. This pattern, while new to the

Volterra series, was successfully recognized and reproduced in predictions downstream of the rotor. Qualitatively, time-series Volterra predictions compared very well with measured distortion patterns at these conditions.

13 Recommendations

The nonlinear Volterra series has been demonstrated as a promising means of modeling non-uniform total pressure propagation through a rotor. While the results of the analysis of this model are encouraging, further improvements to the modeling technique are in order. Suggestions of continued work based on this study are as follows.

- Develop and implement a test plan tailored to the training of Volterra kernels for the modeling of a specific rotor. Include in testing a greater variety of speeds, operating conditions, and distortion types to allow for the inclusion of more information in kernel training, as well as more novel data sets for the evaluation of the model. This is particularly necessary for a better assessment of the technique of training kernels along individual streamlines. Due to the amount of available data in this study, kernels were well under-trained when applying this technique.
- Extend the Volterra series to higher-order terms (i.e. 4^{th} and 5^{th} order) to test the limits of non-uniform total pressure propagation non-linearity. Doing so will require higher resolution data sets (i.e. data every 0.5°).
- Optimize the number of basis functions used in extracting Volterra kernels. In the same fashion, optimize the number of terms used to represent higher-order Volterra kernels.
- Optimize the choice of data sets included in the training of Volterra kernels. This includes the choice of speeds and operating conditions, as well as the number of data sets used.
- Investigate the influence of additional physics based parameters in the normalization of data sets.
- Implement a better method of demonstrating prediction accuracy in the time-domain.
- Develop a method of incorporating average total pressure into Volterra series predictions.

14 Works Cited

Aerospace Resource Document 50015 (SAE ARD50015), January, 1991.

Barker, G. P. and Schneider, H., *Matrices and Linear Algebra*, Holt Rinehart and Winston, Inc., New York, 1968.

Beckwith, T., Marangoni, R., and Lienhard, J., *Mechanical Measurements 5th Edition*, Addison-Wesley Publishing Company, Massachusetts, 1993.

Bendat, J. S., *Nonlinear Systems Techniques and Applications*, John Wiley & Sons, Inc., New York, 1998.

Biesiadny, T., Braithwaite, W., Soeder, R., and Abdelwahab, M., "Summary of Investigations of Engine Response to Distorted Inlet Conditions," NASA Technical Memo No. 87317, Lewis Research Center, Cleveland, OH, 1986.

Boyd, S., Tang, Y. S., and Chua, L. O., "Measuring Volterra Kernels," *IEEE Transactions on Circuits and Systems*, Vol. 30, No. 8, Aug. 1983, pp. 571-577.

Breard, C., Vahdati, M., Sayma, A., and Imregun, M., "An Integrated Time-Domain Aeroelasticity Model for the Prediction of Fan Forced Response Due to Inlet Distortion," Proceedings of ASME Turbo Expo 2000, May 2000, Munich, Germany.

Chow, P. N., Elias, S. R., Hutchinson, B. R., and Koch, J. M., "Experimental and Computational Study of a Radial Compressor Inlet," Dresser-Rand Technical Paper TP103, 2000.

Danforth, C.E., "Distortion Induced Vibration in Fan and Compressor Blading," Journal of Aircraft, Vol. 12, No. 4, April 1975.

Datko, J. and O'Hara, J., "The Aeromechanical Response of an Advanced Transonic Compressor to Inlet Distortion," ASME 87-GT-189, 1987.

Delahaye, B. and Sagnes, P., "Inlet Distortion and Compressor Behavior," ICAS Paper No. 84-1.9.1, 1984.

Fabian, M., Falk, E., Haven, B., and Jumper, E., "A Characterization of the Unsteady Velocity Field Aft of the F109 Turbofan Rotor," Proceedings of the High Cycle Fatigue Conference, 1999.

Gossel, M., *Nonlinear Time Discrete Systems*, Springer-Verlag, Berlin, 1982.

Govardhan, M. and Viswanath, K., "Effect of Circumferential Inlet Flow Distortion and Swirl on the Flow Field of an Axial Flow Fan Stage," ASME 96-GT-263, 1996.

Greitzer, E.M., Tan, C.S., Wisler, D.C., Adamczyk, J.J., and Stazisar, A.J., "Unsteady Flows in Turbomachines: Where's the Beef?," ASME Unsteady Flows in Aeropropulsion, 1994.

Greitzer, E. M. and Longley, J. P., "Inlet Distortion Effects in Aircraft Propulsion System Integration," AGARD-LS-183, May 1992.

Hansen, P. C., *Rank-Deficient and Discrete Ill-Posed Problems*, Society for Industrial and Applied Mathematics, Philadelphia, 1998.

Jenkins, J and Tromp, J., "A Volterra Kernel Identification Scheme Applied to Aerodynamic Reactions," AIAA 90-2803, August 1990.

Lee, Y. W. and Schetzen, M., "Measurement of the Wiener Kernels of a Nonlinear System by Cross-Correlation," *International Journal of Control*, Vol. 2, No. 3, Sep. 1965, pp. 237-254.

Manwaring, S. and Fleeter, S., "Inlet Distortion Generated Periodic Aerodynamic Rotor Response," ASME 89-GT-299, 1989.

Manwaring, S. and Fleeter, S., "Forcing Function Effects of Rotor Periodic Aerodynamic Response," Transactions of ASME, Vol. 113, April 1991.

Manwaring, S., Rabe, D., Lorence, C., and Wadia, A., "Inlet Distortion Generated Forced Response of a Low Aspect-Ratio Transonic Fan," ASME Journal of Turbomachinery, Vol. 119, October 1997.

Miller, R. K., *Nonlinear Volterra Integral Equations*, W. A. Benjamin, Inc., Philippines, 1971.

Morrow, P., "Detailed Test Plan for the Augmented Damping of Low Aspect Ratio Fans (ADLARF)," USAF Technology Branch Turbine Engine Division, WPAFB, March 1993.

Rabe, D., Bolcs, A., and Russler, P., "Influence of Inlet Distortion on Transonic Compressor Blade Loading," AIAA 95-2461, Presented at the 31st Joint Propulsion Conference and Exhibit, July 1995, San Diego, CA.

Rabe, D., Williams, C., and Hah, C., "Inlet Flow Distortion and Unsteady Blade Response in a Transonic Axial-Compressor Rotor," ISABE 99-7297, 1999.

Reid, C., "The Response of Axial Flow Compressors to Intake Flow Distortion," ASME Paper No. 69-GT-29, 1969.

Reisenthel, P. H., "Application of Nonlinear Indicial Modeling to the Prediction of a Dynamically Stalling Wing," AIAA 96-2493, June 1996.

Reisenthel, P. H., "Development of a Nonlinear Indicial Model for Maneuvering Fighter Aircraft," AIAA 96-0896, 1996.

Reisenthel, P. H., "Prediction of Unsteady Aerodynamic Forces Via Nonlinear Kernel Identification," Langley International Forum on Aeroelasticity and Structural Dynamics, Williamsburg, VA, June 1999.

Reisenthel, P. H. and Bettencourt, M. T., "Extraction of Nonlinear Indicial and Critical State Responses from Experimental Data," AIAA 99-0764, Jan. 1999.

Reisenthel, P. H. and Bettencourt, M. T., "Data-Based Aerodynamic Modeling Using Nonlinear Indicial Theory," AIAA 99-0763, Jan. 1999.

Roberts, F., Plourde, G., and Smakula, F., "Insights into Axial Compressor Response to Distortion," AIAA Paper No. 68-565, 1968.

Rugh, W. J., *Nonlinear System Theory – The Volterra / Wiener Approach*, The Johns Hopkins University Press, Baltimore, 1981.

Schetzen, M., *The Volterra and Wiener Theories of Nonlinear Systems*, John Wiley & Sons, New York, 1980.

Schwartz, J., "An Experimental and Analytical Investigation of Dynamic Flow Response of a Fan Rotor with Distorted Inlet Flow," M.S. Thesis, Virginia Polytechnic Institute and State University, Blacksburg, VA, 1999.

Silva, W. A., "Identification of Linear and Nonlinear Aerodynamic Impulse Responses Using Digital Filter Techniques," AIAA 97-3712, Aug. 1997.

Silva, W. A., "Application of Nonlinear Systems Theory to Transonic Unsteady Aerodynamic Responses," *Journal of Aircraft*, Vol. 30, No. 5, 1993, pp. 660-668.

Small, M., "Improved Methods for Predicting the Effects of Inlet Flow Distortion on the Performance of Axial Flow Compressors," M.S. Thesis, Virginia Polytechnic Institute and State University, Blacksburg, VA, May 2001.

Smith, S. W., *The Scientist and Engineer's Guide To Digital Signal Processing, 2nd Edition*, California Technical Publishing, San Diego, 1997.

Steenken, W. G., Williams, J. G., Yuhas, A. J., and Walsh, K. R., "An Inlet Distortion Assessment During Aircraft Departures at High Angle of Attack for an F/A-18A Aircraft," NASA Technical Memorandum 104328, Mar. 1997.

Vidyasagar, M., *Nonlinear Systems Analysis*, Prentice-Hall, Inc., New Jersey, 1978.

Volterra, V., *Theory of Functionals and of Integral and Integro-Differential Equations*, Blackie & Sons Ltd., London, 1930.

VITA

Jonathan G. Luedke

The author, son of Glenn and Judy Luedke, was born in March 1977 in Woodbridge, VA. After spending the entirety of his childhood in this same town he followed in his sister's footsteps and enrolled as an undergraduate at Virginia Tech in southwestern Virginia. Completing a Bachelor's degree in Mechanical Engineering four years later, Jonathan moved into the working world, accepting his first full time position as an engineer at a natural gas transmission company. After spending a year in the natural gas utility business he returned to his alma mater, Virginia Tech, to work full time towards a Master's degree in Mechanical Engineering. Upon graduation he will begin employment in the Propulsion Laboratory at GE Corporate Research and Development in Schenectady, NY. Currently Jonathan is engaged to his girlfriend of two years, and friend of nearly eight, Jenny. The happy couple plans to be married in the fall of the next year.